# Initiation of cortical spreading depolarization and pre-epileptic hyperactivity in a multiscale mathematical model of NaV1.1 mutations

Louisiane Lemaire

UNIVERSITÉ CÔTE D'AZUR

ÉCOLE DOCTORALE
SCIENCES FONDAMENTALES ET APPLIQUÉES


# THÈSE DE DOCTORAT

# Initiation de la dépression corticale envahissante et hyperactivité pre-épileptique dans un modèle mathématique multi-échelles des mutations de $Na_V1.1$

**Louisiane LEMAIRE**

Inria Sophia Antipolis-Méditerranée Research Center

**Présentée en vue de l'obtention du grade de docteur en** Mathématiques
**d'**Université Côte d'Azur
**Dirigée par** : Mathieu Desroches
**Co-encadrée par** : Martin Krupa
**Soutenue le** : 13/12/2021

**Devant le jury, composé de** :
Mathieu Desroches, CR Inria, Inria
Boris Gutkin, DR CNRS, École Normale Supérieure
Gemma Huguet, Associate Prof., UPC
Martin Krupa, Prof., UCA-Inria
Massimo Mantegazza, DR Inserm, IPMC-CNRS-UCA-Inserm
Patricia Reynaud-Bouret, DR CNRS, UCA-CNRS
John Rinzel, Prof., NYU

Inria

# Initiation de la dépression corticale envahissante et hyperactivité pre-épileptique dans un modèle mathématique multi-échelles des mutations de $Na_V1.1$

**Présidente du jury**
Patricia Reynaud-Bouret, DR CNRS, UCA-CNRS

**Rapportrice et rapporteur**
Gemma Huguet, Associate Prof., Universitat Politècnica de Catalunya
John Rinzel, Prof., NYU

**Examinateurs**
Mathieu Desroches, CR Inria, Inria Sophia Antipolis-Méditerranée Research Centre
Boris Gutkin, DR CNRS, École Normale Supérieure
Martin Krupa, Prof., UCA-Inria

**Invité**
Massimo Mantegazza, DR Inserm, IPMC-CNRS-UCA-Inserm

**Initiation de la dépression corticale envahissante et hyperactivité pre-épileptique dans un modèle mathématique multi-échelles des mutations de $Na_V1.1$**

---

**Résumé**

Les mutations "perte de fonction" de *SCN1A*, le gène codant pour le canal sodique voltage-dépendant $Na_V1.1$, provoquent différents types d'épilepsie, tandis que ses mutations "gain de fonction" provoquent la migraine hémiplégique familiale de type 3 (MFH3). La manière dont ces effets opposés induisent les activités pathologiques paroxystiques spécifiques de l'épilepsie (crises épileptiques) ou de la migraine (dépolarisation corticale envahissante, DCE) n'est pas encore claire. Dans cette thèse, nous étudions les mécanismes différentiels conduisant à l'initiation de ces activités pathologiques. Nous utilisons une approche de modélisation mathématique, en étroite collaboration avec des biologistes expérimentaux.

Nous avons développé et analysé un modèle à conductance de deux neurones (pyramidal et GABAergique) interconnectés, avec des concentrations ioniques dynamiques. Nous avons étudié les mutations MFH3 et épileptogènes dans ce même cadre, en modifiant seulement deux paramètres pertinents. Les simulations de ce modèle et les expériences sur des souris (activation pharmacologique de $Na_V1.1$ ou induction de l'hyperactivité des neurones GABAergiques par optogénétique) suggèrent que le facteur clé de l'initiation de la DCE dans le cas de MFH3 est une accumulation du potassium extracellulaire due à l'activité des neurones. Il est intéressant de noter que dans notre modèle, l'accumulation progressive initiale de potassium extracellulaire qui déclenche la DCE ne nécessite pas une augmentation de la fréquence des potentiels d'action du neurone GABAergique. En ce qui concerne les mutations épileptogènes de $Na_V1.1$, dans notre modèle, la perte de fonction de ce canal entraîne une vulnérabilité accrue du neurone GABAergique à la transition vers un bloc de dépolarisation. Cette prédiction est confirmée expérimentalement par des enregistrements sur des souris $Scn1a^{+/-}$ réalisés par nos collaborateurs. Sur cette base, nous proposons le phénomène de bloc de dépolarisation des neurones GABAergiques comme un mécanisme pro-épileptique impliqué dans le déclenchement des crises, car il provoque le dysfonctionnement de l'inhibition des réseaux, ce qui constitue un contexte idéal pour la genèse des crises épileptiques. Globalement, concernant les mécanismes pathologiques des mutations de $Na_V1.1$, nos résultats suggèrent l'implication de mécanismes d'hyperexcitabilité des réseaux autres que la modification de la fréquence des potentiels d'actions des neurones GABAergiques. Ceci est intéressant, car la modification de fréquence est l'une des principales caractéristiques étudiées en ce qui concerne les pathologies de l'excitabilité neuronale.

Pour étudier les scénarios de bifurcations dynamiques associés à la transition du régime de potentiels d'action répétés vers la DCE ou l'hyperactivité épileptiforme, nous avons construit un modèle plus simple, avec une séparation explicite des échelles de temps. Cette version idéalisée conserve les principales caractéristiques du modèle biophysique détaillé, tout en se prêtant mieux à une analyse théorique. Dans ce cadre, nous avons reproduit les deux transitions pathologiques avec une variation minimale des paramètres. Nous modélisons le potassium extracellulaire avec un système bistable lent-rapide, pour capturer sa dynamique caractéristique telle qu'elle est enregistrée au site d'initiation de la DCE. Dans le cas des mutations épileptogènes de $Na_V1.1$, le principal ingrédient est un déplacement de la position de la bifurcation responsable de la transition du régime de potentiels d'actions répétés vers le bloc de dépolarisation.

**Mots clés**

Modèle à conductance, dynamique des concentrations ioniques, dynamiques lentes-rapides, bloc de dépolarisation, dépression corticale envahissante, migraine hémiplégique familiale, épilepsie, $Na_V1.1$/*SCN1A*.

**Initiation of cortical spreading depolarization and pre-epileptic hyperactivity in a multiscale mathematical model of $Na_V1.1$ mutations**

---

**Abstract**

Loss of function mutations of *SCN1A*, the gene coding for the voltage-gated sodium channel $Na_V1.1$, cause different types of epilepsy, whereas gain of function mutations cause familial hemiplegic migraine type 3 (FHM3). It is not clear yet how these opposite effects can induce the paroxysmal pathological activities that are specific of epilepsy (seizures) or migraine (cortical spreading depolarization, CSD). In this thesis, we investigate the differential mechanisms leading to the initiation of these pathological activities. We use a mathematical modeling approach, working in close collaboration with experimentalists.

We developed and analyzed a two-neuron conductance-based model of interconnected GABAergic and pyramidal neurons, with dynamic ion concentrations. We studied both FHM3 and epileptogenic mutations within the same framework, modifying only two relevant parameters. Both simulations of this model and experiments on mice (acute pharmacological activation of $Na_V1.1$ or optogenetic-induced hyperactivity of GABAergic neurons) suggest that the key factor for CSD initiation in the case of FHM3 is a spiking-generated build-up of extracellular potassium. Interestingly, in our model the initial progressive accumulation of extracellular potassium which triggers CSD does not require an increased firing frequency of the GABAergic neuron. Concerning $Na_V1.1$ epileptogenic mutations, in our model loss of function of this channel results in an enhanced susceptibility of the GABAergic neuron to depolarization block. This prediction is confirmed experimentally by recordings on *Scn1a*$^{+/-}$ mice performed by our collaborators. Based on this, we propose depolarization block of GABAergic neurons as a pro-epileptic mechanism involved in the triggering of seizures, because it causes the dysfunction of network inhibition, which is an ideal background for the genesis of seizures. Overall, concerning the pathological mechanisms of $Na_V1.1$ mutations, our results suggest the involvement of mechanisms of network hyperexcitability other than the modification of the firing frequency of GABAergic neurons. This is noteworthy, because modifications of firing frequency is one of the principal features investigated in pathologies of neuronal excitability.

To study the dynamic bifurcation scenarios associated with the transition from tonic firing to CSD or epileptiform hyperactivity, we built a simpler model, with explicit timescale separation. This idealized version retains the salient features of the detailed biophysical model, while being more amenable to theoretical analysis. In this setting, we reproduced both pathological transitions upon minimal parameter variation. We model extracellar potassium with a bistable slow-fast system, to capture its characteristic dynamics as it is recorded at the site of CSD initiation. In the case of $Na_V1.1$ epileptogenic mutations, the main ingredient is a shift in the position of the bifurcation responsible for the transition from tonic firing to depolarization block.

**Keywords**

Conductance-based model, ion concentration dynamics, slow-fast dynamics, depolarization block, cortical spreading depression, familial hemiplegic migraine, epilepsy, $Na_V1.1$/*SCN1A*.

# Contents

# Acronyms

**ACSF** artificial cerebrospinal fluid. 20, 21, 25, 40

**AIS** axon initial segment. 82

**CSD** cortical spreading depolarization. vii, viii, 1–8, 10–27, 30, 39, 41–50, 52, 53, 55, 57–60, 64, 72, 74–76, 81–84

**DB** depolarization block. 75–77, 82, 84

**DC** direct current. 6, 11, 12, 21, 25

**DIC** differential interference contrast. 40

**FHM** familial hemiplegic migraine. 1, 2, 6, 41

**FHM1** FHM type 1. 2, 6, 22, 23, 81

**FHM2** FHM type 2. 2, 6, 22, 23, 81

**FHM3** FHM type 3. viii, 1–3, 6, 8, 13, 15, 20, 22, 23, 27–30, 38, 39, 41–44, 46–49, 54–56, 58, 81, 83

**FHN** FitzHugh–Nagumo. 64, 75

**GEFS+** genetic epilepsy with febrile seizures plus. 2

**HR** Hindmarsh-Rose. 75

**IOS** intrinsic optical signal. vii, 6–8, 11, 19, 24, 25

**LFP** local field potential. 6–8, 10–12, 18–20

**MUA** multi-unit activity. 18, 19

**PD** period-doubling. 70

**PV+** parvalbumin-positive. 82

**SD** spreading depolarization. 1, 2, 6, 21, 22, 64, 81

**SNIC** saddle-node on invariant circle. 63, 83, 84

**SUDEP** sudden unexpected death in epilepsy. 21

**TTX** tetrodotoxin. 16, 17, 22

**VGAT** vesicular GABA transporter. 7, 10–13, 15–18, 20–22, 24, 39, 40

**WT** wild type. 7, 12, 21

# Chapter 1

# Introduction

## 1.1 Motivation

$Na_V1.1$ is a voltage-gated sodium channel, coded by the gene *SCN1A*, which is mainly expressed in GABAergic neurons. It is a major target of human mutations implicated in pathologies of neuronal excitability [1, 2]. Loss of function mutations of $Na_V1.1$ have been found in patients with epileptic disorders. On the other hand, gain of function mutations have been linked to types of migraine in which cortical spreading depolarizations (CSDs) are involved. It is not clear yet how these opposite effects lead to one or the other of two different manifestations of neuronal hyperactivity: epileptic seizures and CSD.

### 1.1.1 How can $Na_V1.1$ gain of function cause migraine with aura?

Familial hemiplegic migraine (FHM) is a rare but severe Mendelian type of migraine with aura, which typically includes hemiparesis, i.e. weakness of one side of the body. Three genes responsible for FHM are currently known. *SCN1A* was the last of them to be identified [3], causing FHM type 3 (FHM3). Although one study initially reported loss of function for two FHM3 $Na_V1.1$ mutations studied in heterologous expression systems [4], more recent works have instead established gain of function of the channel as the common functional effect of FHM3 mutations [1, 2, 5–8].

#### CSD is a pathological mechanism of migraine with aura

CSD is a wave of transient intense neuronal firing followed by a sustained depolarization block, which slowly propagates in the cortex [9]. It was first observed by Leão in 1944 [10]. This phenomenon is accompanied by a breakdown of transmembrane ion concentration gradients, water influx and cell swelling [11–13].

Spreading depolarizations (SDs) generated in anoxic conditions are implicated in stroke, traumatic brain injury, and subarachnoid hemorrhage [9, 13, 14]. On the contrary, CSD generated in normoxic conditions is thought to be a pathological mechanism of migraine with aura, based on numerous studies performed with experimental animals [9, 14]. Even though clinical evidence linking CSD and migraine symptoms is limited, a recent report has unequivocally demonstrated with electrophysiological recordings that SD-induced depression of spontaneous cortical activity was linked to symptomatic migraine aura in a patient [15]. In addition to the generation of the patient's percept of migraine aura, it has been proposed that in migraineurs SDs can stimulate trigeminal nociceptors innervating the meninges, activating pain pathways and provoking the headache [9, 13, 16].

#### The link between FHM3 mutations and CSD initiation remains unclear

*In vivo* experiments on the knock-in $Scn1a^{L263V/+}$ mouse model have shown increased propensity to CSD in this model and suggest that FHM3 mutations predominantly affect

CSD initiation, rather than its propagation. Indeed, no increase in CSD propagation speed was observed in this model [17], unlike what was reported for the two other types of FHM (FHM1 and FHM2) [18, 19]. However, even though SDs have been observed and extensively studied for decades, the specific pathological mechanisms that lead to their initiation are not well understood. In particular, it is not clear yet how gain of function mutations in voltage-gated sodium channels of GABAergic neurons, which classically have an inhibitory role, can lead to the network hyperexcitability characterizing CSD. Studying this link can give a better understanding not only of FHM3 pathophysiology, but also of CSD and migraine with aura in general, as well as other pathologies in which SDs are involved.

### 1.1.2 How does $Na_V1.1$ loss of function lead to epileptic seizures?

Numerous epileptogenic mutations of $Na_V1.1$ have been identified. This is the case for Dravet syndrome [20], a severe and pharmacoresistant developmental and epileptic encephalopathy, and for genetic epilepsy with febrile seizures plus (GEFS+) [21], characterized in general by milder phenotypes. Studies performed both in vitro and in mouse models have shown that these mutations cause a loss of function of the channel [1, 2, 22–24]. Since $Na_V1.1$ is particularly important for GABAergic neurons' excitability [22], the causal link between its loss of function and epileptiform activity is certainly more intuitive than the one between its gain of function and CSD. Indeed, it is expected that a failure of excitability in inhibitory neurons can promote hyperexcitability of neuronal networks and seizures. However, here also there is no consensus when it comes to the precise mechanisms of seizure generation involved.

## 1.2 Outline

In this thesis, we investigate the differential mechanisms by which gain or loss of function of $Na_V1.1$ sodium channels can induce the pathological neuronal hyperactivities which are characteristic of either hemiplegic migraine (CSD) or epilepsy (seizure). We do not aim to model a full blown CSD or a seizure. Instead, we are interested in the conditions which can lead to their initiation. We use a mathematical modeling approach, working in close collaboration with the neurophysiologist Massimo Mantegazza from the Institute of Molecular and Cellular Pharmacology (IPMC) in Sophia Antipolis (France).

### Chapter 2. Initiation of migraine-related cortical spreading depolarization by hyperactivity of GABAergic neurons and $Na_V1.1$ channels

In Chapter 2, we present experimental results based on *electrophysiological recordings* performed *in vivo*, in brain slices and in cell lines. They were carried out by the group of Massimo Mantegazza at IPMC and by Paolo Scalmani at the Foundation IRCCS Neurological Institute Carlo Besta in Milan (Italy). Increased glutamatergic activity is thought to be a key factor for generating CSD [9, 13]. However, we show here that *acute pharmacological activation of $Na_V1.1$* or *optogenetic-induced hyperactivity of GABAergic neurons* is sufficient to ignite CSD in the neocortex. Neither GABAergic nor glutamatergic synaptic transmission was required for CSD initiation. CSD was not generated in other brain areas, suggesting that this is a neocortex-specific mechanism of CSD initiation.

We also build a *two-neuron conductance-based model* of interconnected GABAergic and pyramidal neurons, in which we incorporated *ionic concentration dynamics* for both neurons. In agreement with the experimental data, in this model $Na_V1.1$ gain of function

facilitates CSD initiation. Numerical simulations suggest that accumulation of extracellular potassium induced by neuronal firing is the key factor. This prediction is confirmed by an experiment where *chelation of extracellular potassium* blocks CSD initiation.

Overall, our results provide a mechanism linking $Na_V1.1$ gain-of-function to CSD generation in FHM3: spiking-generated extracellular $K^+$ build-up. This collaborative work resulted in a publication in *The Journal of Clinical Investigations*, an important biomedicine journal [25].

## Chapter 3. Modeling $Na_V1.1$ epilepsy and migraine mutations in a microcircuit with dynamic ion concentrations

In Chapter 3, we extend the model of Chapter 2 to also study $Na_V1.1$ epileptogenic mutations. We model FHM3 mutations by increasing the persistent sodium current in the GABAergic neuron and epileptogenic mutations by decreasing the sodium conductance in the GABAergic neuron. Therefore, we study both mutations within the same framework, modifying only two parameters.

In our simulations, the key effect of FHM3 mutations is ion fluxes modification at each action potential (in particular the larger activation of voltage-gated potassium channels), and the resulting CSD-triggering extracellular potassium accumulation, which is not caused only by modifications of firing frequency. Epileptogenic mutations, on the other hand, increase GABAergic neurons' susceptibility to depolarization block, without major modifications of firing frequency before it. Our modeling results connect qualitatively to experimental data: potassium accumulation in the case of FHM3 mutations and facilitated depolarization block of the GABAergic neuron in the case of epileptogenic mutations. Both these effects can lead to hyperexcitability of the pyramidal neuron, inducing in the migraine condition depolarization block of both the GABAergic and the pyramidal neuron.

Overall, our findings suggest different mechanisms of network hyperexcitability for migraine and epileptogenic $Na_V1.1$ mutations, and imply that modifications of firing frequency may not be the only relevant pathological mechanism. This collaborative work is published in *PLOS Computational Biology* [26].

## Chapter 4. Idealized multiple-timescale model of CSD initiation and pre-epileptic hyperactivity

The dynamics of the detailed biophysical model studied in Chapter 3 indicates the presence of multiple implicit timescales, but its large dimension complicates their exploitation. In Chapter 4, we develop a simpler version of the model, which is more amenable to theoretical analysis while keeping its key elements.

The idealized model has three timescales: the dynamics of the two neurons is fast (four variables), extracellular potassium is slow (one variable) and we introduced a super slow variable which participates in generating the potassium dynamics. The explicit timescale separation between those variables allows us to use the theory of *slow-fast dynamical systems*, where slow variables can be treated as parameters in the fast singular limit. We perform *numerical continuation* to retrieve the bifurcation structure with respect to those parameters. We then study the transition between physiological and pathological firing regimes as *dynamic bifurcations* of the full system.

To model $Na_V1.1$ migraine mutations, based on the conclusions from the previous chapters, we increase the spiking-induced release of potassium by the GABAergic neuron. This facilitates the jump of the bistable potassium from a low state to a high state, which causes the transition from tonic firing to depolarization block for both neurons.

The use of an additional super slow timescale to model potassium dynamics allows us to reproduce the characteristic rise which is recorded at the site of CSD initiation by our collaborators (see Fig. 4.1). Concerning $Na_V1.1$ epileptogenic mutations, we model the increased susceptibility of GABAergic neurons to depolarization block by shifting the (dynamic) bifurcation responsible for the transition from tonic firing to depolarization block to a lower input. The resulting drop of inhibition leads to a high firing frequency of the pyramidal neuron, which we interpret as pre-epileptic hyperactivity.

# Chapter 2

# Initiation of migraine-related cortical spreading depolarization by hyperactivity of GABAergic neurons and $Na_V1.1$ channels

The content of this chapter is published in [25]: O. Chever et al. "Initiation of Migraine-Related Cortical Spreading Depolarization by Hyperactivity of GABAergic Neurons and $Na_V1.1$ Channels". *The Journal of Clinical Investigation* (Sept. 7, 2021). My contribution to this work was to design and implement the computation model, and to interpret the simulations.

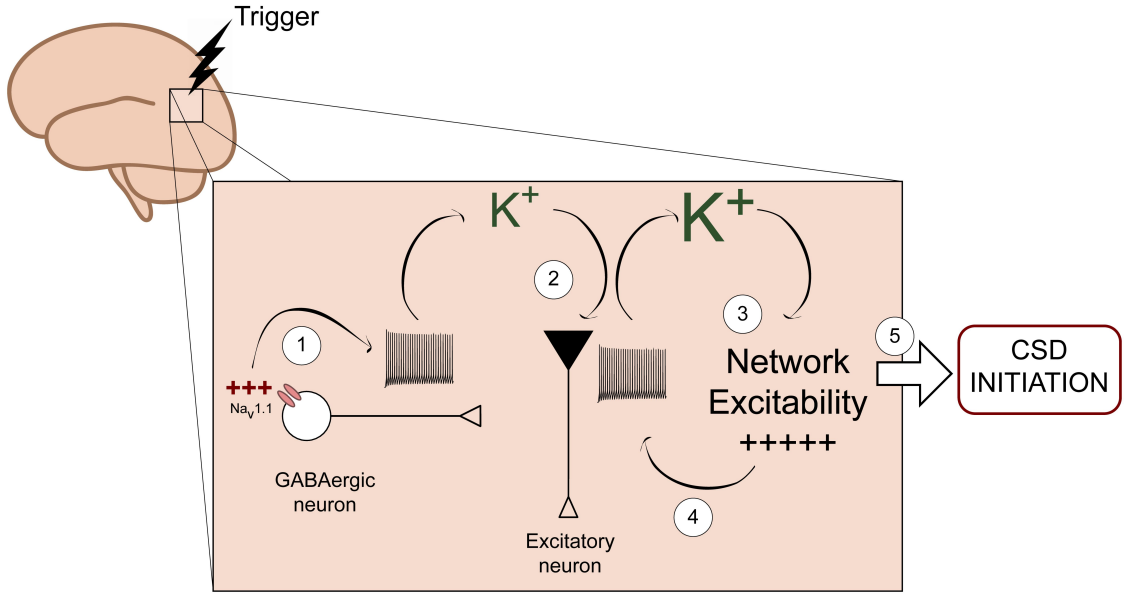


**Graphical abstract.**

## 2.1 Introduction

Familial hemiplegic migraine (FHM), has become a model disease for more common forms of migraine with aura and has allowed the identification of some molecular/cellular pathological mechanisms of human migraine and CSD [9, 16], which may be at least in part shared by SDs involved in other diseases. FHM type 1 (FHM1) is caused by gain-of-function mutations of the α1 subunit of the $Ca_V2.1$ P/Q type $Ca^{2+}$ channel (the *CACNA1A*

gene) [27], FHM type 2 (FHM2) by loss-of-function mutations of the α2 subunit of the glial $Na^+/K^+$ pump (the *ATP1A2* gene) [28]. The experimental induction of CSD is facilitated in both FHM1 and FHM2 genetic mouse models [18, 19], primarily because of increased network excitability induced by excessive release or insufficient reuptake of glutamate [29–31], consistent with a similar overall mechanism affecting the glutamatergic system. These results have contributed to establish the current hypothesis that increased glutamatergic activity is the most important factor for triggering CSD.

FHM type 3 (FHM3) is caused by mutations of the $Na_V1.1$ (*SCN1A*) $Na^+$ channel [3], which is particularly important for GABAergic neurons' excitability [22]. We and others have provided evidence that, in contrast to epileptogenic mutations, FHM3 mutations cause instead gain-of-function of the channel, often increasing persistent current, inducing hyperexcitability of transfected GABAergic neurons in primary culture [1, 2, 5–8, 12, 32–34], which could be responsible for CSD initiation, as we have recently proposed in a computational model [35]. Interestingly, a recent work showed that knock-in mice carrying the FHM3 L263V $Na_V1.1$ mutation experience spontaneous CSD events but not seizures, although detailed mechanisms of CSD generation have not been studied [17]. These results point to a counterintuitive mechanism in CSD caused by $Na_V1.1$ gain-of-function, different than in the case of FHM1 or FHM2. However, it is not clear yet whether and how CSD (and possibly other SDs) could be generated by $Na_V1.1$ gain-of-function/GABAergic neurons' hyperactivity.

Here, we addressed this issue inducing acute $Na_V1.1$ gain-of-function that mimics the functional effect of FHM3 mutations and performing selective optogenetic stimulation of GABAergic neurons, carrying out experiments *in vivo*, in brain slices and in cell lines.

## 2.2 Results

### 2.2.1 Acute gain-of-function of $Na_V1.1$ channels induces CSD selectively in the neocortex

To disclose the role of $Na_V1.1$ channels' gain-of-function in the generation of CSD, we used the spider toxin Hm1a that has been reported as a specific $Na_V1.1$ enhancer [36]. We confirmed, by performing whole-cell patch-clamp recordings of $Na^+$ currents in cell lines, that also in our conditions Hm1a selectively targets $Na_V1.1$ over the two other $Na_V$ isoforms expressed in the adult cortex, $Na_V1.2$ and $Na_V1.6$, although only at low concentration (10 nM) (Fig. $S_1$). Importantly, Hm1a induced a 12-fold increase of persistent current, an effect that is comparable to that previously observed with FHM3 mutations [5–8, 34], making it a good pharmacological tool for modeling the effect of these mutations.

We tested the effect of the toxin in whole brain slices that included different structures, performing extracellular local field potential (LFP) recordings and intrinsic optical signal (IOS) imaging in an extended area (Fig. 2.1; Fig. $S_2$). Bath application of 10 nM Hm1a lead to spontaneous CSD ignition, which was observed both as DC shift in LFP recordings (Fig. 2.1 B) and as propagating wave in IOS images (Fig. 2.1 D, E and Video 1). CSD was elicited in 22.5 % of the slices within 10 min of Hm1a application (our time limit for determining successful induction), whereas we have never observed CSD in control conditions (Fig. 2.1 C). Interestingly, CSD was elicited only in the neocortex and never in the other structures monitored (hippocampus, dorsal striatum, globus pallidus and thalamus) (Fig. 2.1 D, E and Video 1). To confirm that this was a neocortex-specific effect of Hm1a, we evaluated whether in our conditions other brain areas were able to generate spreading depolarizations by applying short puffs of 130 mM KCl, a classical method of CSD induction [9, 37]. The success rate for CSD induction was 100 % in all the structures tested: the neocortex (Fig. $S_3$ A - C and Video 2), the striatum (Fig. $S_3$ $D_1$ and Video 3)

and the hippocampus (Fig. $S_3$ $D_2$ and Video 4). Neither Hm1a-induced nor KCl-induced CSD propagated outside the structure in which they were induced.

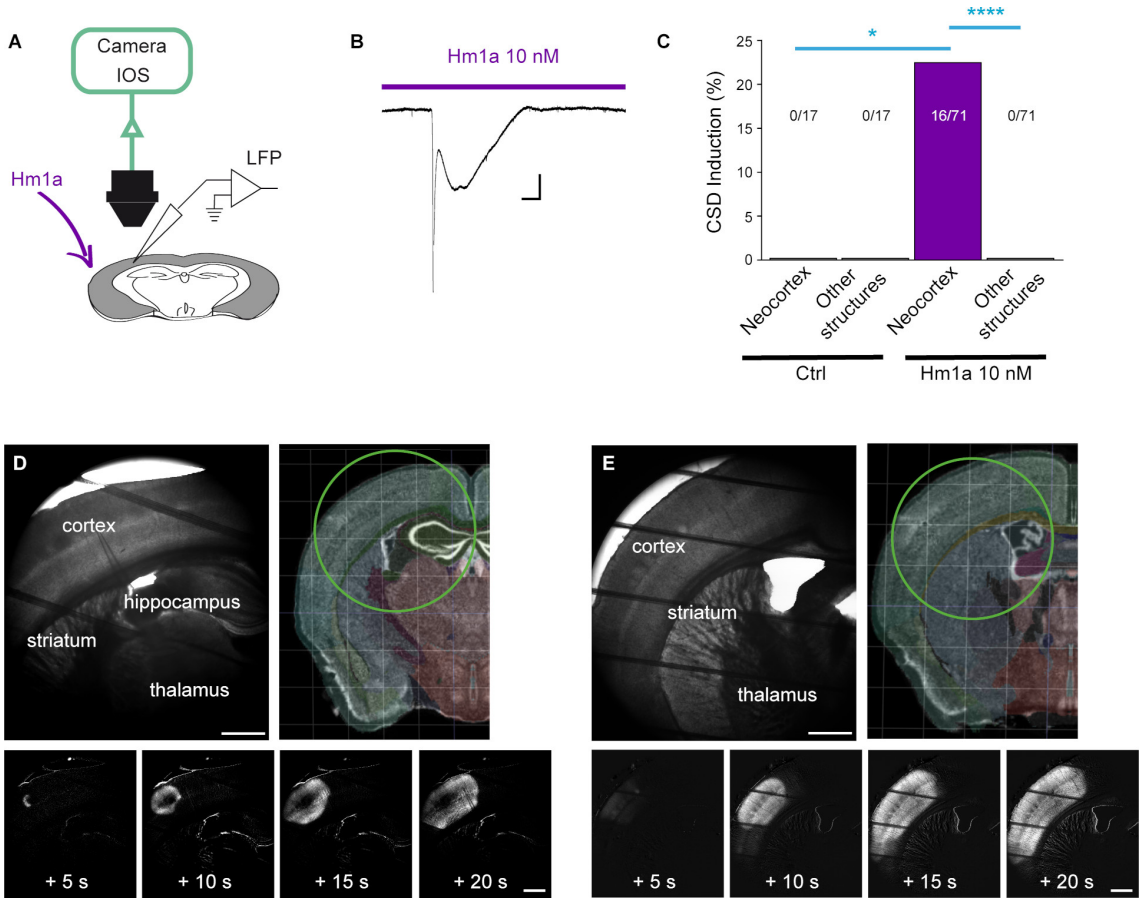


**Figure 2.1: The selective $Na_V1.1$ enhancer Hm1a specifically triggers CSD in the neocortex. A.** Experimental setting: brain slices were perfused with 10 nM Hm1a, a concentration at which Hm1a is selective for $Na_V1.1$ (see Fig. $S_1$), and CSD induction was monitored with extracellular local field potential (LFP) recordings and intrinsic optical signal (IOS) imaging obtained in extended brain regions (4X objective, 0.35X camera adapter). **B.** Representative LFP recording of a CSD observed in the neocortex during the perfusion with Hm1a. Scale bars 1 mV, 20 s. **C.** Overall results showing the lack of spontaneous CSD in control (0/17 slices), and success rate for neocortical induction with bath-application of Hm1a (16/71), which never triggered CSD in other structures (Fisher's exact test, Bonferroni correction, neocortex control vs neocortex Hm1a, $*p = 0.04$; neocortex Hm1a vs other structures Hm1a, $****p = 10^{-4}$). **D.** Upper-left panel, raw transmitted light image of a representative coronal slice including the neocortex, the hippocampus, the dorsal striatum, the globus pallidus and the thalamus; upper-right panel, illustration of a whole hemisphere (Brain Explorer, Allen Institute) in which the imaged area is indicated by the circle (see Fig. $S_2$ for more details). The four bottom panels correspond to time series of image processing of IOS acquisitions (one image every 5 s, the first one 5 s after CSD initiation; see Methods), which show that CSD was triggered only in the neocortex. Scale bar: 500 µm. **E.** Raw transmitted light image of another representative coronal slice including the neocortex, the dorsal striatum, the globus pallidus and the thalamus (upper-left);, illustration of a whole hemisphere (Brain Explorer, Allen Institute) in which the imaged area is indicated by the circle (see Fig. $S_2$ for more details). The four bottom panels are time series of processed IOS images, which show that CSD was triggered only in the neocortex. Scale bar: 500 µm. See Video 1.

Then, we performed current-clamp patch-clamp recordings from both GABAergic and pyramidal neurons in neocortical Layer II-III of brain slices from GAD67-GFP knock-in mice (which selectively label GABAergic neurons), to confirm that the Hm1a-induced

gain-of-function of $Na_V1.1$ can increase excitability preponderantly of GABAergic neurons in the neocortex. We maintained the resting membrane potential at around −70 mV and elicited action potential discharges with injections of 2.5 s-long depolarizing current steps of increasing amplitude, comparing the properties of input-output relationships before and after 10 min perfusion with 10 nM Hm1a. In order to minimize the variability of firing patterns of GABAergic neurons, we selected for the analysis fast-spiking non-adapting neurons (Fig. 2.2 A - C), firing features that are typical of parvalbumin-positive (PV+) neurons. All the recorded pyramidal neurons showed regular spiking discharges (Fig. 2.2 D - F). The application of Hm1a induced in GABAergic neurons a leftward shift of the input-output relationship (28 % mean increase of firing frequency at 50 % of the input-output) and an increase of the maximal firing frequency (7 % mean increase), whereas the firing properties of pyramidal glutamatergic neurons were not modified. Thus, Hm1a induces in the neocortex hyperexcitability of GABAergic neurons but not of pyramidal neurons, and specifically triggers CSD in the neocortex, although in our experimental conditions spreading depolarizations can be induced by puffs of KCl in all the structures tested (neocortex, hippocampus and striatum).

### 2.2.2 Optogenetic hyperactivation of GABAergic neurons can initiate CSD selectively in the neocortex

To directly investigate the role of GABAergic neurons, we used hemizygous VGAT.cre-ChR2(H134R)tdTomato.lox (VGAT-ChR2) mice, in which channelrhodopsin(ChR2)-H134R is selectively expressed in these neurons in different brain regions (Fig. $S_4$) [38]. We activated GABAergic neurons in coronal brain slices illuminating with blue light an entire cerebral hemisphere, and we monitored CSD generation by both LFP recordings and IOS imaging of several brain structures (Fig. 2.3 A, B and Video 5). Notably, similar to the experiments performed with Hm1a, the optogenetic activation of GABAergic interneurons induced CSD only in the neocortex: we never observed it in the hippocampus, striatum or thalamus. Mean latency to induction was 26.2±1.8 s ($n$ = 104) and propagation speed was 3.2±0.1 mm/min ($n$ = 104) (Fig. 2.3 C). Macroscopic features of CSD induced by optogenetic stimulation were similar to those of CSD triggered by a focal puff of 130 mM KCl in the neocortex (Fig. $S_3$ A - C and Video 2) or by perfusion with Hm1a (Fig. 2.1 and Video 1). We performed a subset of experiments for determining the rate of success of optogenetic CSD induction (Fig. 2.3 D; see Methods for detailed procedure), observing that it was induced in 85 % of VGAT-ChR2 slices (always only in the neocortex) and never with control littermates (i.e. slices from VGAT-Cre, ChR2.lox or WT mice). Notably, CSD was readily induced by focal puff of 130 mM KCl in all the slices, both from VGAT-ChR2 mice and control littermates (Fig. $S_3$ C), confirming that all the slices could generate CSD (not only those from VGAT-ChR2 mice). Moreover, as already highlighted before, CSD was readily induced by focal puff of 130 mM KCl also in the hippocampus and the striatum (Fig. $S_3$ D). Several studies in different models have shown that functions of PV+ GABAergic neurons are significantly modified by *SCN1A* mutations [1, 2], FHM3 mutations can induce hyperexcitability of these neurons, as observed in [39], and we have quantified the effect of Hm1a on these neurons (Fig. 2.2). Notably, we were able to induce optogenetically neocortical CSD also in slices from hemizygous PV.cre-ChR2(H134R)tdTomato.lox (PV-ChR2) mice (Fig. 2.3 E), in which ChR2-H134R is selectively expressed in PV+ neurons, although with a lower success rate (28 %) than in VGAT-ChR2 slices. Thus, CSD initiation by over-activation of GABAergic neurons is a neocortex-specific mechanism, similarly to CSD initiation by Hm1a, and over-activation of a GABAergic subpopulation (PV+ neurons) is sufficient for its induction.

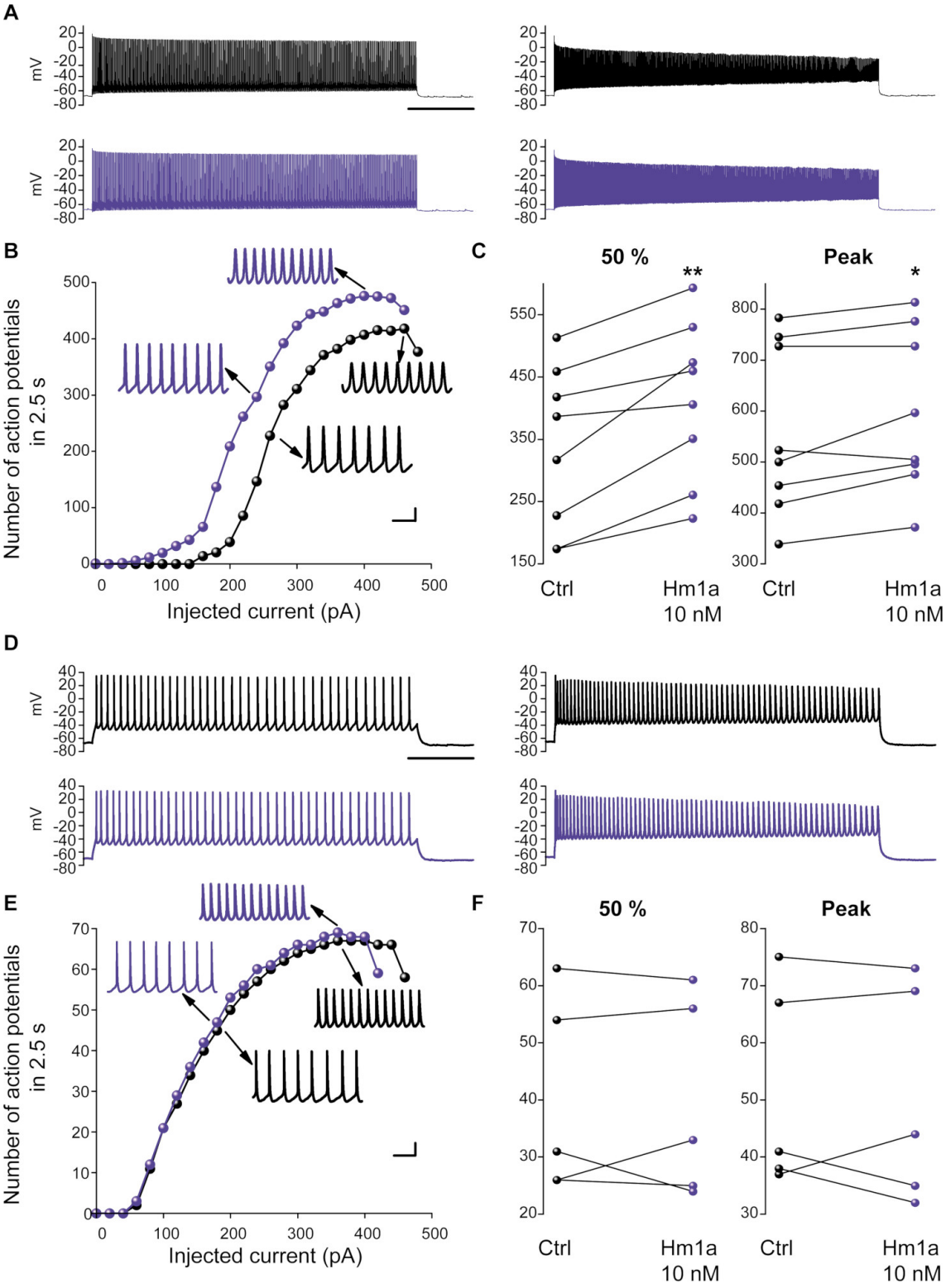


**Figure 2.2: Hm1a increases the excitability of fast spiking GABAergic neurons but not of pyramidal neurons.** Recordings in neocortical Layer II-III of GAD67-GFP knock-in mice (which label GABAergic neurons). **A.** Left, representative traces at 50 % of the input-output relationship, recorded from a fast spiking neuron before (black) and during (violet) perfusion with 10 nM Hm1a, scale bar 500 ms; right, representative traces recorded from the same interneuron at the peak of the input-output relationship. **B.** Representative plot of the *(continued next page)*

**Figure 2.2** ***(previous page)*****:** effect of Hm1a on the input-output relationship recorded from the same fast spiking interneuron; and magnified traces taken from a 50 ms time window at the middle of the traces displayed in A; scale bars 20 mV, 10 ms. **C.** Firing frequency for each recorded neuron before and during Hm1a perfusion at 50 % (mean increase $\Delta = 28.4 \pm 7.0$ %, ** $p = 0.008$; 352 AP/2.5 s median 334±46 mean±SEM in control; 433, 412±45 with Hm1a) and at the peak of the input-output relationship (mean increase $\Delta = 7.1 \pm 2.6$ %; * $p = 0.03$; 511 AP/2.5 s, 561±59 in control; 551, 595±57 with Hm1a) ($n = 8$). **D.** Left, representative traces at 50 % of the input-output relationship, recorded from a pyramidal neuron before (black) and during (violet) perfusion with Hm1a, scale bar 500 ms; right, representative traces recorded from the same pyramidal neuron at the peak of the input-output relationship, before (black) and during (violet) perfusion with Hm1a. **E.** Representative input-output relationship obtained from the same pyramidal neuron and magnified traces taken from a 50 ms time window in the middle of the traces displayed in D; scale bars 20 mV, 10 ms. **F.** Firing frequency for each recorded neuron before and during Hm1a perfusion at 50 % (Δ=-2.2±6.4%, $p = 1$; 31AP/2.5 s median 40.0±7.7 mean±SEM in control; 33, 39.8±7.8 with Hm1a) and at the peak of the input-output relationship ($\Delta = 0.2 \pm 7.9$ %, $p = 0.9$; 41 AP/2.5 s, 51.6±8.0 in control; 44, 50.6±8.6 with Hm1a) ($n = 5$). Wilcoxon Signed Ranks test for all the comparisons.

We then evaluated the response of pyramidal and GABAergic neurons in Layer II-III of the neocortex of VGAT-ChR2 mice to the optogenetic stimulation before the induction of CSD, to validate the specific response of GABAergic neurons to the illumination, performing whole-cell patch-clamp recordings (Fig. 2.3 F). We observed that GABAergic neurons (which we identified as non-pyramidal fast spiking non-adapting neurons), directly responded with short latency to the illumination, which triggered long lasting firing, whereas pyramidal neurons did not respond directly to the illumination and begun to spike after few tens of seconds of illumination, consistent with a specific rapid and long lasting activation of GABAergic neurons.

In a further series of experiments, we evaluated the effect of Hm1a on optogenetic-induced CSD, hypothesizing a synergic role (Fig. 2.4). In fact, in brain slices in which Hm1a application did not induce CSD, subsequent optogenetic stimulation induced CSD with a 28 % reduction of triggering latency and a 20 % increase of propagation speed, compared to control slices without Hm1a. CSD was triggered only in the neocortex also in this series of experiments and its duration, evaluated measuring the LFP half-width, was not modified by Hm1a. Therefore, optogenetic CSD was facilitated by Hm1a, confirming the key role of $Na_V1.1$ channels' gain-of-function and over-activation of GABAergic neurons in the mechanism of CSD initiation that we have disclosed.

### 2.2.3 Computational model of CSD initiation by overactivation of $Na_V1.1$ channels and GABAergic neurons

We have recently shown that in simulations obtained with a conductance-based model of a GABAergic neuron connected to a pyramidal neuron, an overactivation of the GABAergic neuron can lead to depolarizing block of the pyramidal neuron, which we considered the initiation of CSD [35]. In that model, the overactivation of the GABAergic neuron was obtained increasing its external depolarizing input (modeling a pathological state, as well as a condition similar to our optogenetic stimulation). Several putative GABAergic activation-related mechanisms were tested, and we identified the frequency of interneuron firing and the related increase of $[K^+]_{out}$ as the key element for inducing depolarizing block of the pyramidal neuron [35].

Here, we have refined the model, in particular improving the features of the GABAergic neuron, which now better models a fast spiking cortical interneuron [40], and including complete dynamics of ion concentrations for both neurons (Fig. 2.5 A; see Methods), so

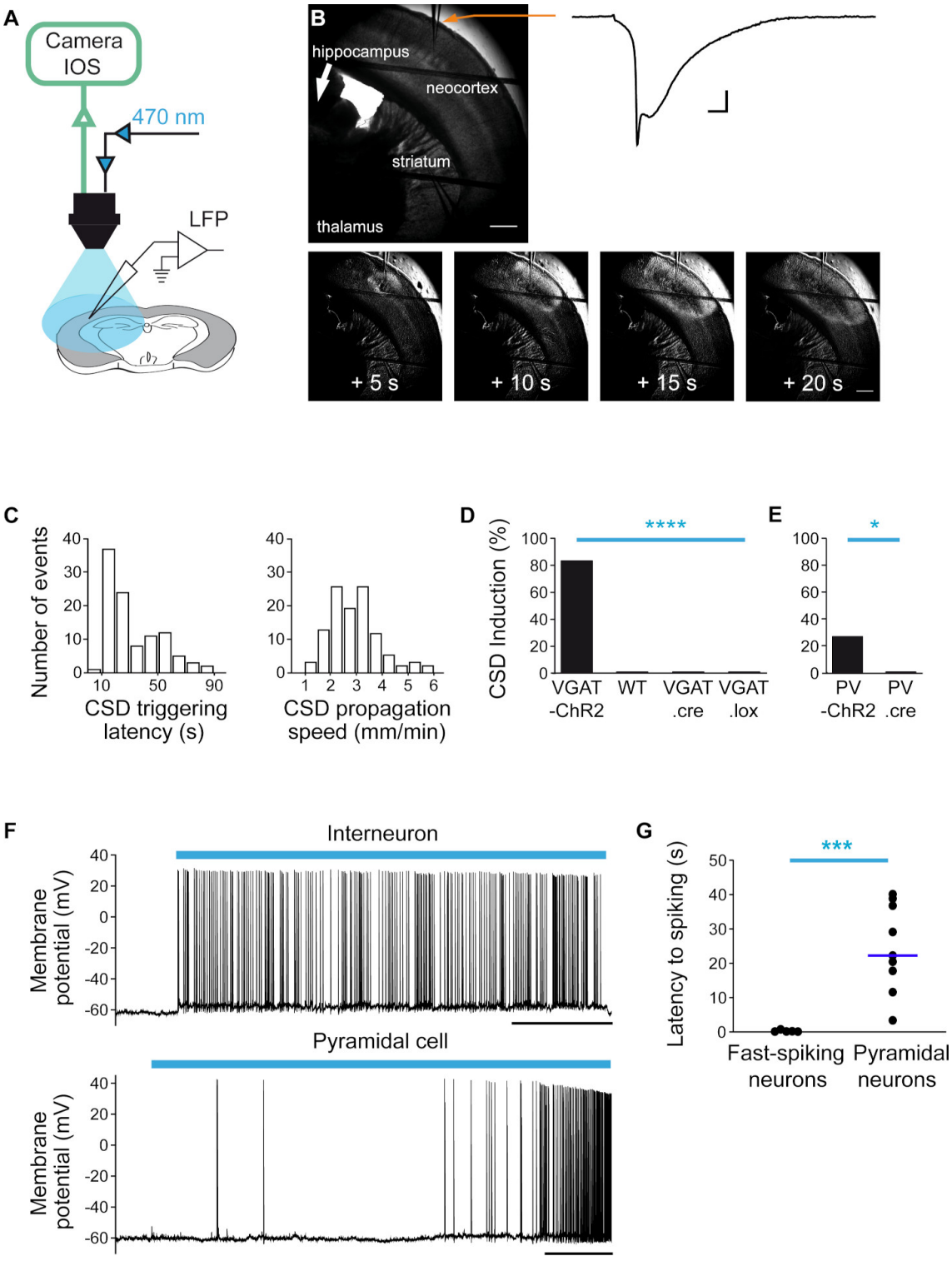


**Figure 2.3: CSD is triggered specifically in the neocortex by optogenetic–induced hyperactivity of GABAergic neurons. A.** Experimental setting for optogenetic stimulations of a complete hemisphere in coronal slices (the area of illumination was larger than the area of image acquisition). **B.** Representative CSD that was induced only in the neocortex in slices from VGAT-ChR2 mice containing neocortex, hippocampus, dorsal striatum and thalamus, revealed by both the negative DC shift in the LFP and the IOS propagating wave. The four bottom panels are time series corresponding to image-processed IOS acquisitions (one image *(continued next page)*

**Figure 2.3** ***(previous page)*****:** every 5 s, the first one 5 s after CSD initiation; see Methods). Scale bars: 500 µm. **C.** Left panel, distribution of latencies of CSD initiation upon 470 nm illumination in VGAT-ChR2 slices (median=19 s, $n = 103$ slices); right panel, distribution of propagation speed of optogenetic-induced CSD in VGAT-ChR2 slices (median=3.18 mm/min, $n = 103$ slices). **D.** Success rate of optogenetic CSD obtained in a different series of experiments comparing slices from VGAT-ChR2 (11/13 slices), WT (0/14), VGAT.Cre (0/10) and ChR2.lox (0/10) mice (Fisher's exact test, **** $p = 7 \cdot 10^{-5}$). **E.** Success rate of optogenetic CSD obtained in slices from PV-ChR2 mice (4/14 slices) or control PV-cre littermates (0/15 slices) (Fisher's exact test, * $p = 0.04$). **F.** Left panels, representative whole-cell patch-clamp recordings of GABAergic and pyramidal neurons in layer II-III upon optogenetic illumination: a fast spiking GABAergic neuron responded to the 470nm illumination (blue bar) with short latency, whereas a pyramidal neuron responded with longer latency, scale bar 20 s. **G.** overall latencies to spiking during 470 nm illumination for fast spiking neurons (median = 0.30 s; $n = 5$) and pyramidal neurons (median = 22.26 s; $n = 12$) (Mann-Whitney test, *** $p = 0.001$); these recordings were not performed at the site of initiation, which with this experimental setting was variable within the neocortex and not identifiable a priori.

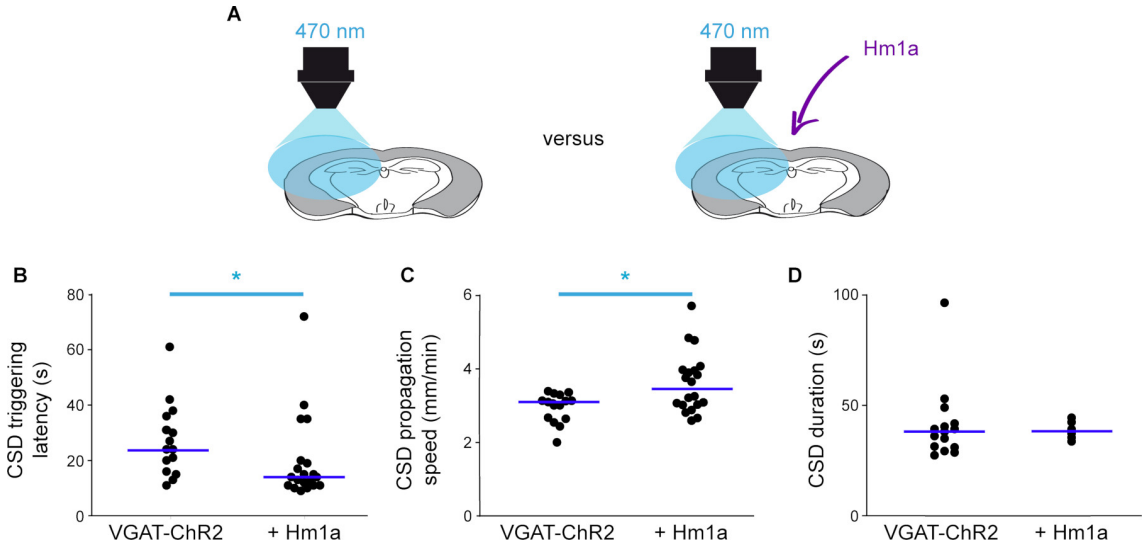


**Figure 2.4: Effect of Hm1a on optogenetic CSD induction. A.** Further series of experiments in which features of optogenetic CSD induction were compared in VGAT-ChR2 slices perfused with Hm1a (but in which the toxin did not induce CSD within 10 min) and control VGAT-ChR2 slices, waiting 10 min before to illuminate (these experiments have been included in Fig. 2.1 D). **B.** Latencies of optogenetic CSD measured in control VGAT-ChR2 slices (median = 24 s, mean ± SEM = 27.3 ± 3.4 s; $n = 15$ slices) and VGAT-ChR2 slices perfused with Hm1a (median = 14 s, mean ± SEM = 19.8 ± 3.4 s; $n = 20$ slices) (Mann-Whitney test, * $p = 0.014$); **C.** Propagation speed of optogenetic CSD in the same slices (control VGAT-ChR2, median = 3.14 mm/min, mean ± SEM = 3.0 ± 0.1 mm/min, $n = 15$ slices; VGAT-ChR2 slices perfused with Hm1a without CSD, median = 3.50 mm/min, mean ± SEM = 3.6 ± 0.2 mm/min, $n = 20$ slices) (Mann-Whitney test, * $p = 0.025$). **D.** Duration of optogenetic-induced CSD measured at half width of the LFP DC shift (control VGAT-ChR2 slices, median = 38.1 s, mean ± SEM = 41.1 ± 4.4 s, $n = 15$ slices, VGAT-ChR2 slices perfused with Hm1a but without CSD, median = 38.3 s, mean ± SEM = 38.7 ± 1.7 s, $n = 6$ slices) (Mann-Whitney test, $p = 0.7$).

that the modifications of ion concentrations can modulate the activity of both neurons. The direct overactivation of the GABAergic neuron, with conditions similar to those that we used in [35], generated simulations that were similar to those obtained in [35] (not shown). Then, we tested the effect of an increase of the persistent $Na^+$ current of the GABAergic neuron, which mimics the common effect of most FHM3 mutations [1, 5–8, 12, 32–34, 39], as well as that of Hm1a. We modeled the control physiological condition implementing a persistent conductance equal to 1 % of the maximal $Na^+$ conductance, and

we increased it up to 6 % to simulate a pathological condition or the presence of Hm1a (which is conservative in comparison with the quantitative effect of FHM3 mutations or Hm1a). In the physiological condition (Fig. 2.5 B), an external depolarizing input to the GABAergic neuron ($g_{D,i}$) of 0.1 mS/cm$^2$, without application of external input to the pyramidal neuron ($g_{D,e}$), was able to induce high frequency firing of the GABAergic neuron. As in [35], long lasting high frequency firing of the GABAergic neuron overcame its inhibitory effect, because it increased $[K^+]_{out}$. In the simulation of Fig. 2.5 B, $[K^+]_{out}$ reached a maximum of 11.2 mM, depolarizing the pyramidal neuron and triggering its spiking, which was transient and ended after few seconds, when $[K^+]_{out}$ relaxed to lower levels. In this condition, there was no depolarizing block (CSD initiation). When the same simulation was run with persistent $Na^+$ conductance of the GABAergic neuron increased to 6 % (Fig. 2.5 C), in the initial phase the GABAergic neuron discharged at higher frequency leading to a larger increase of $[K^+]_{out}$ (up to 13.6 mM). Importantly when the pyramidal neuron was engaged in firing, both neurons underwent depolarizing block, with $[K^+]_{out}$ rising to >60 mM, indicating CSD initiation. In fact, the increase of persistent $Na^+$ current of the GABAergic neuron facilitated CSD, leading to a decrease of the minimal $g_{D,i}$ that can induce CSD initiation (Fig. 2.5 D). Moreover, similar to the experimental data of Fig. 2.4 B, the increase of persistent current led to a reduction of the CSD initiation latency (Fig. 2.5 E); CSD was induced in this simulation with $g_{D,i} = 0.349$ mS/cm$^2$, which was the minimal input able to induce CSD with 0 % persistent current (Fig. 2.5 D).

Finally, in simulations in which the pyramidal neuron was removed from the model, we evaluated the effect of an increase of persistent current on the "intrinsic" firing frequency of the GABAergic neuron. We observed that it was increased at all the levels of external input tested (Fig. 2.5 F). This shows that the persistent current can increase the firing frequency of the GABAergic neuron independently from the interactions with the pyramidal neuron (e.g. synaptic input and modifications of ion concentrations).

Overall, the model shows that an increase of persistent $Na^+$ current, mimicking FHM3 mutations or Hm1a, induces hyperexcitability of the GABAergic neuron, leading to a facilitation of CSD, which is ignited with lower values of external input and shorter latency, consistent with the experimental data. Interestingly, a prediction of the model obtained in the simulations presented here and in those of [35], is that the key factor for CSD initiation induced by overactivation of GABAergic neurons is an increase of $[K^+]_{out}$, initially directly generated by the spiking of the GABAergic neuron. Thus, we investigated in our experimental system the detailed mechanisms of CSD initiation.

### 2.2.4 Detailed mechanism of CSD initiation

We initially evaluated the effect of $Na_V1.1$ loss-of-function on CSD initiation, to compare it with the gain-of-function tested above. We crossed VGAT-ChR2 mice with knockout *Scn1a*$^{+/-}$ mice, which model the epileptic encephalopathy Dravet syndrome and in which one allele of the *Scn1a* gene is not functional, causing $Na_V1.1$ haploinsufficiency and hypo-excitability of GABAergic neurons [1, 22]. This selective effect on GABAergic neurons has been observed in numerous studies, also at the age that we have used for our investigation, although there could be remodeling at later developmental stages [41]. In brain slices from VGAT-ChR2/*Scn1a*$^{+/-}$ mice, the success rate of optogenetic CSD induction was reduced 2.4-fold (Fig. 2.6 A), showing that $Na_V1.1$ loss-of-function and reduced excitability of GABAergic neurons can inhibit CSD initiation by optogenetic activation of GABAergic neurons. Then, we tested the importance of extracellular $K^+$ accumulation as a key parameter for CSD initiation. We initially used VGAT-ChR2/*Scn1a*$^{+/-}$ slices in which the optogenetic stimulation did not trigger CSD, perfusing them with rACSF in which $[K^+]_{out}$ was moderately increased (from 3.5 to 8 mM),

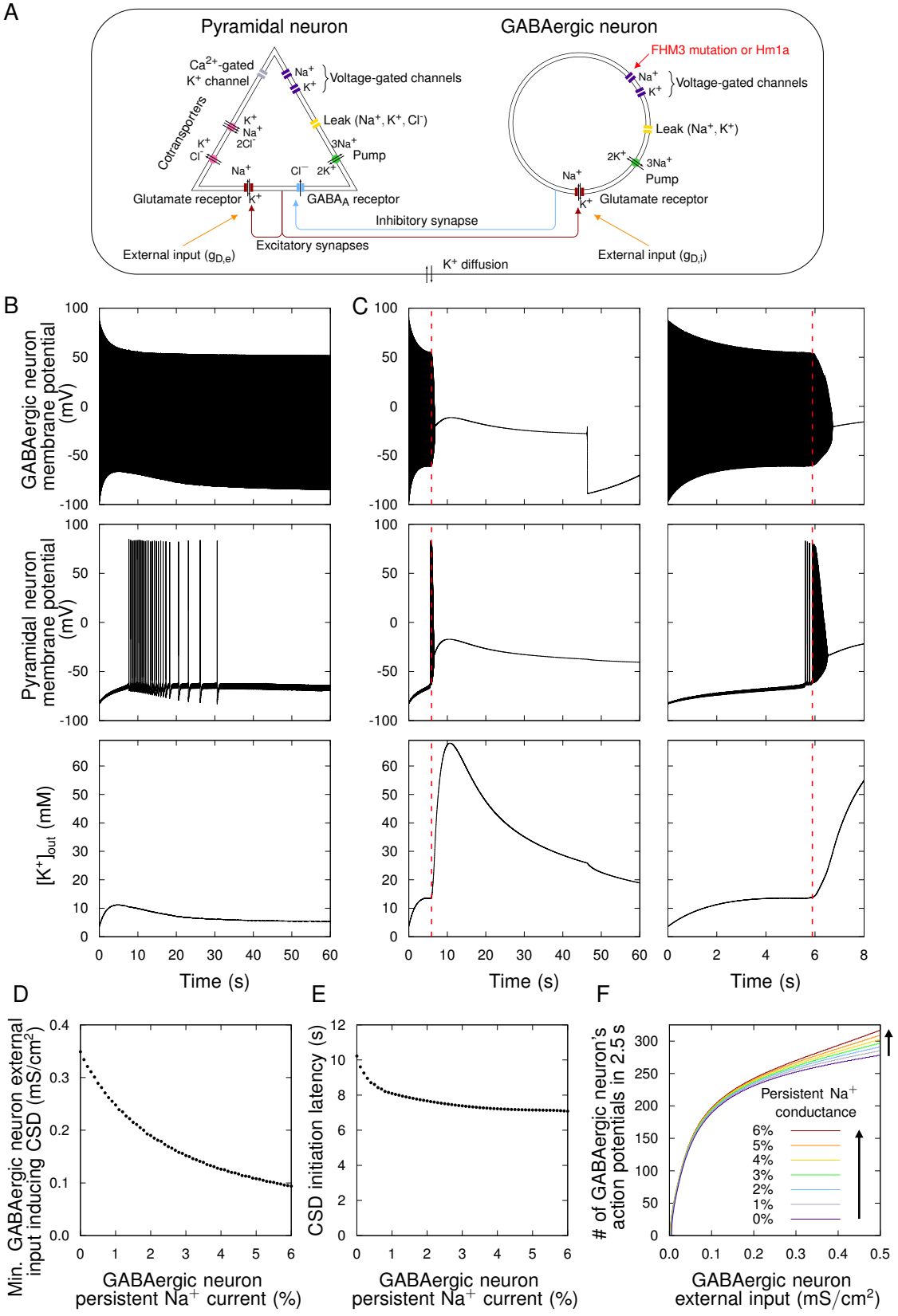


**Figure 2.5: The increase of GABAergic neuron's persistent current facilitates the initiation of CSD in a computational model. A.** Diagram illustrating the conductance-based computational model that we used to model the effect of migraine *(continued next page)*

**Figure 2.5** ***(previous page)*****:** mutations and of Hm1a by increasing the persistent $Na^+$ current of the GABAergic neuron. $g_{D,e}$ and $g_{D,i}$ are glutamatergic conductances that model the baseline excitatory inputs ("excitatory drive") of the pyramidal and of the GABAergic neuron, respectively. **B.** Simulation, with GABAergic neuron's physiologic persistent $Na^+$ current (1 %), of the effect of a constant external depolarizing input to the GABAergic neuron ($g_{D,i} = 0.1\,mS/cm^2$) without input to the pyramidal neuron ($g_{D,e} = 0\,mS/cm^2$): membrane potential of the GABAergic neurons (upper panel), membrane potential of the pyramidal neuron (middle panel) and extracellular $K^+$ concentration (lower panel). **C.** Same simulation with increased GABAergic neuron's persistent $Na^+$ current (6 %, mimicking the effect of FHM3 mutations and of Hm1a); the right panels display with an enlarged time scale the first phase of the simulation shown in the panels on the left. The vertical red line indicates the beginning of the large $[K^+]_{out}$ increase that leads to depolarizing block. **D.** Effect of an increase of the GABAergic neuron's persistent $Na^+$ current on the lowest external input to the GABAergic neuron ($g_{D,i}$) sufficient to induce depolarizing block. **E.** Effect of an increase of the GABAergic neuron's persistent $Na^+$ current on the latency of depolarizing block with $g_{D,i} = 0.349\,mS/cm^2$ (the lowest input to the GABAergic neuron able to generate CSD with 0 % persistent $Na^+$ conductance; see panel D). **F.** Effect of the amount of persistent current on the firing frequency of the GABAergic neuron, in a simulation in which the pyramidal neuron was removed, reflecting the direct effect of the persistent current on the firing properties of the GABAergic neuron.

and applying a second optogenetic stimulation. Notably, we found that the reduced success rate of CSD induction in VGAT-ChR2/*Scn1a*$^{+/-}$ slices was rescued with 8 mM $[K^+]_{out}$ (Fig. 2.6 B). The latency of optogenetic CSD induction was not different in the three conditions (median 39 s, mean±SEM 39±4 s for control VGAT-ChR2, $n$ = 23, 4 slices not included because initiation was outside the imaged area; 38 s, 45±5 s for VGAT-ChR2/*Scn1a*$^{+/-}$, $n$ = 11, one slice not included; 47 s, 51±14 s for VGAT-ChR2/*Scn1a*$^{+/-}$ with 8 mM KCl, $n$ = 6, one slice not included; $p$ = 0.70 Kruskal-Wallis test), and there was a trend towards an increase of the propagation speed in VGAT-ChR2/*Scn1a*$^{+/-}$ slices (median 3.07 mm/min, mean±SEM 2.41±0.15 mm/min for control VGAT-ChR2, $n$ = 27; 3.12 mm/min, 3.2±0.2 mm/min for VGAT-ChR2/*Scn1a*$^{+/-}$, $n$ = 12; 3.95 mm/min, 3.97±0.28 mm/min for VGAT-ChR2/*Scn1a*$^{+/-}$ with 8 mM KCl, $n$ = 7; $p$ = 0.07 Kruskal-Wallis test). Importantly, the threshold of CSD induced applying puffs of 130 mM KCl (obtained by quantifying the area of KCl application as in [37]) was not different in slices from VGAT-ChR2/*Scn1a*$^{+/-}$ and VGAT-ChR2 mice (Fig. 2.6 C), confirming that the inhibition of optogenetic CSD in VGAT-ChR2/*Scn1a*$^{+/-}$ slices is not caused by a generic reduced propensity to CSD generation caused by modifications induced by the epileptic condition. Notably, CSD propagation speed was increased (median 4.32mm/min, mean±SEM 4.39±0.29 mm/min, $n$ = 14) compared to VGAT-ChR2 littermates (3.02 mm/min, 3.27±0.35 mm/min, $n$ = 8; $p$ = 0.047 Mann-Whitney test), consistent with the trend observed in optogenetic experiments and with different mechanisms of initiation and propagation.

Next, in optogenetic experiments in which we used the $K^+$ scavenger Kryptofix2.2.2 (2 mM) to chelate extracellular $K^+$ [42] we observed a 5.6-fold reduction of optogenetic CSD success rate (Fig. 2.6 D). This confirmed the importance of extracellular $K^+$ in the mechanism of CSD initiation, although chelation of basal extracellular $K^+$ could also interfere with neuronal excitability. Even though our computational model points to extracellular $K^+$ build-up directly induced by the spiking of GABAergic neurons, it has been shown that hyperactivity of GABAergic neurons can favor neuronal network excitation also by other mechanisms, including synaptic transmission-driven activation of neuronal-glial networks [43–46]. Thus, we performed pharmacological experiments to disclose the detailed mechanism linking hyperactivity of GABAergic neurons to CSD initiation. In

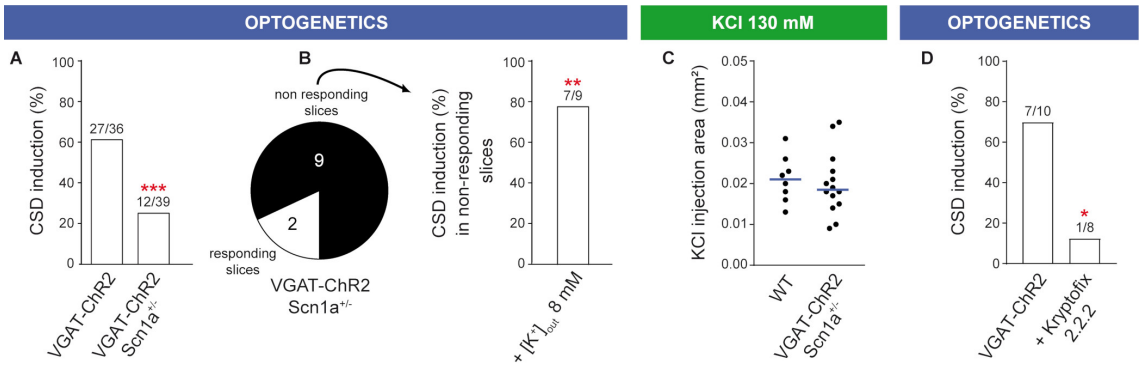


**Figure 2.6: Effect of the reduction of GABAergic neurons' excitability, extracellular $K^+$ chelation on optogenetic CSD induction. A.** Reduction of optogenetic CSD induction success rate in slices from VGAT-ChR2-*Scn1a*$^{+/-}$ mice compared to slices of VGAT-ChR2 littermates (Fisher's exact test, *** $p = 0.0002$). **B.** A different series of experiments in which optogenetic CSD was induced after the increase of $[K^+]_{out}$ to 8 mM in VGAT-ChR2-*Scn1a*$^{+/-}$ slices in which optogenetic CSD was previously not induced with standard $[K^+]_{out}$ (Fisher's exact test, ** $p = 0.002$). **C.** Threshold of CSD induction quantified by the area of puff applications of KCl 130 mM in slices from VGAT-ChR2-*Scn1a*$^{+/-}$ (median 0.021, mean±SEM 0.021±0.002 mm$^2$, $n = 14$) compared to VGAT-ChR2 littermates (0.019; 0.020±0.002 mm$^2$, $n = 8$; Mann-Whitney test, $p = 0.58$). **D.** Reduction of optogenetic CSD induction rate with extracellular $K^+$ chelation by application of 2.2.2-cryptand (Kryptofix2.2.2): success rate 70 % ($n = 10$) in control VGAT-ChR2 slices, 12.5 % ($n = 8$) with 2 mM Kryptofix2.2.2 (Fisher's exact test, * $p = 0.025$).

particular, the $K^+$-$Cl^-$ cotransporter KCC2 can induce post-synaptic $K^+$ efflux and is involved in excitatory actions of GABAergic transmission leading to hyperexcitability [44]. However, two different selective KCC2 inhibitors did not modify the success rate and dynamics (latency, propagation speed) of CSD induced by optogenetic stimulation, not even upon pre-treatment of slices with the GABA-A receptor agonist isoguvacine that we used to increase KCC2 baseline activity (Fig. 2.7 A - C). Further, we tested blockers of neuronal excitability or synaptic transmission. The $Na^+$ channel/action potential blocker tetrodotoxin (TTX) completely suppressed CSD induction (Fig. 2.7 D), whereas the block of glutamate (Kainate-AMPA-NMDA) and/or GABA-A receptors (with CNQX-CPP and gabazine, respectively), or the application of the $Ca^{2+}$ channel blocker $Cd^{2+}$, which completely blocked synaptic transmission (Fig. $S_5$), did not modify the success rate of CSD induction (Fig. 2.7 D). Latency to induction was instead longer with $Cd^{2+}$(Fig. 2.7 E). Notably, neurotransmission, in particular glutamatergic one, was important for sustaining CSD propagation, because in the presence of CNQX-CPP or $Cd^{2+}$, the speed of CSD propagation was reduced (Fig. 2.7 F) and CSD often aborted, ending after an initial propagation around the initiation site (Supplementary Table). Gabazine induced a trend towards higher propagation speed (Fig. 2.7 F), which is consistent with the results that we obtained with *Scn1a*$^{+/-}$ mice. These data highlight once more different mechanisms for initiation and propagation.

Altogether, these results demonstrate that GABAergic neurons' hyperexcitability is sufficient for CSD initiation in the neocortex, that CSD is not directly triggered by ion flux through channelrhodopsin, and that synaptic transmission-driven mechanisms are not necessary, although they are implicated in propagation. Also, they suggest that the mechanism of initiation could involve spike-generated $[K^+]_{out}$ increase.

To disclose whether spike-generated $[K^+]_{out}$ increase was directly involved in CSD initiation, we first evaluated the $[K^+]_{out}$ dynamics during optogenetic illumination, measuring $[K^+]_{out}$ at the site of CSD initiation with $K^+$-sensitive electrode recordings, together with LFP/multi-unit activity (MUA) recordings. In order to perform recordings at the site of

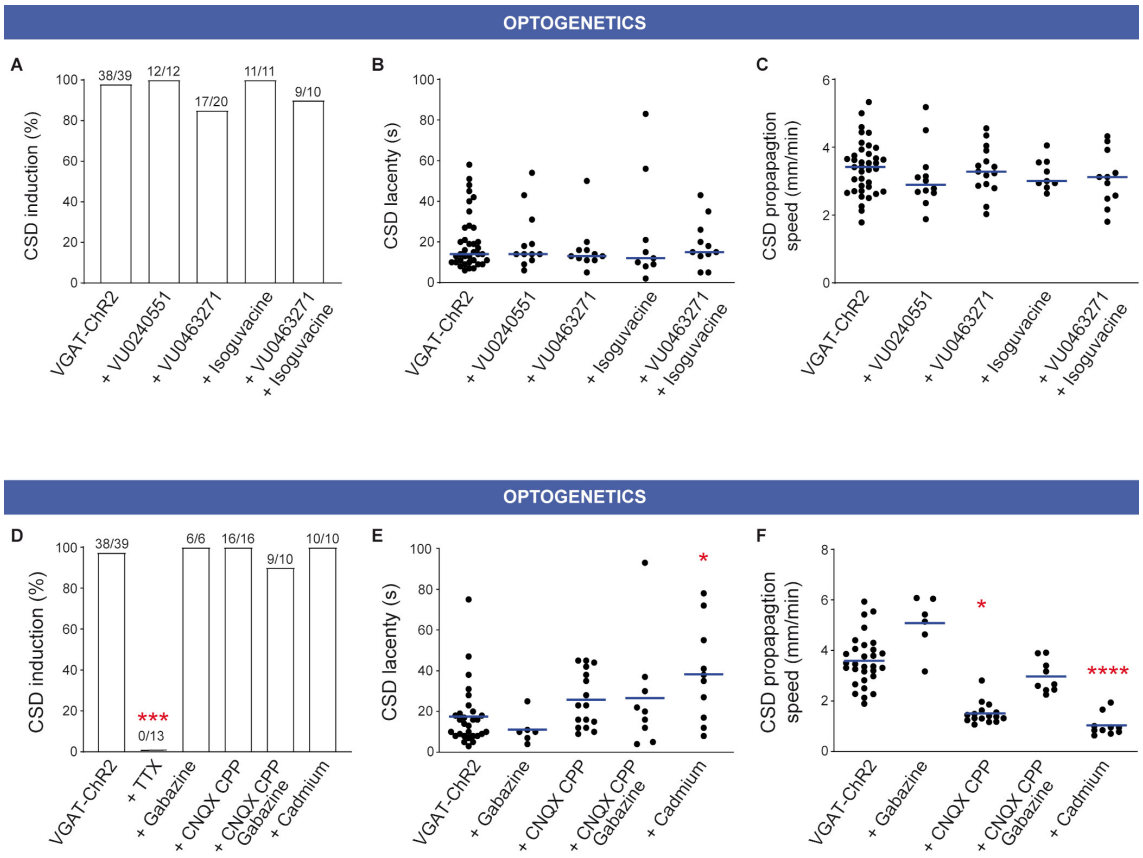


**Figure 2.7: Effect of block of KCC2, neuronal excitability or synaptic transmission on optogenetic CSD induction. A.** Success rate of optogenetic CSD in VGAT-ChR2 slices in control (100 %, $n = 39$) with the KCC2 blocker VU0240551 10 µM (100 %, $n = 12$), the KCC2 blocker VU04663271 10 µM (85 %, $n = 20$), the GABA-A agonist Isoguvacine 10 µM (100 %, $n = 11$) or VU0463271 10 µM + Isoguvacine 10 µM (90 %, $n = 10$); $p = 0.0493$ overall Fisher's exact test, not significant with Bonferroni-corrected pairwise test. **B.** Latency to optogenetic CSD induction in VGAT-ChR2 slices in control (median 14.0 s, mean±SEM 20.0±2.3 s; $n = 38$), with VU0240551 (14.0, 21.0±4.2 s, $n = 12$), with VU04663271 (13.0, 16.5±3.5 s, $n = 11$), Isoguvacine (15.0, 19.0±3.5 s, $n = 11$) or VU0463271+Isoguvacine (12, 24±9.1 s, $n = 9$) (Kruskal-Wallis test $p = 0.93$). **C.** CSD propagation speed in control (median 3.42 mm/min, mean±SEM 3.38±0.13 s; $n = 38$), with VU0240551 (2.89, 3.12±0.26 mm/min, $n = 12$), with VU04663271 (3.28, 3.32±0.18 mm/min, $n = 15$), Isoguvacine (3.12, 3.08±0.25 mm/min, $n = 11$) or VU0463271+Isoguvacine (3.00, 3.19±0.16 mm/min, $n = 9$) (Kruskal-Wallis test $p = 0.93$). **D.** Success rate of optogenetic CSD in VGAT-ChR2 slices in control (100 %, $n = 39$) with the $Na^+$ channel blocker TTX 1 µM (0 %; $n = 13$), with GABA-A (Gabazine 15 µM) and/or NMDA-AMPA-Kainate (CPP 10 µM, CNQX 20 µM) receptor antagonists (Gabazine 0 %, $n = 6$; CCP+CNQX, 100 %, $n = 16$; Gabazine+CCP+CNQX, 90 %, $n = 10$), or the $Ca^{2+}$ channel blocker $Cd^{2+}$ (100 µM) to fully block synaptic release (100 %, $n = 10$) (Fisher's exact test, $^{****}p = 4 \cdot 10^{-14}$; Bonferroni-corrected post-test, $^{****}p < 0.0001$ for TTX). **E.** Latency to optogenetic CSD induction in control (median 14.0 s, mean±SEM 17.6±2.5 s; $n = 29$), with Gabazine (10.0, 11.2±3.0 s, $n = 6$), with CPP+CNQX (23.0, 25.8±3.4 s, $n = 16$), CPP+CNQX+Gabazine (20.0, 26.6±9.1 s, $n = 9$) or $Cd^{2+}$ (36.6, 38.3±7.6 s, $n = 10$) (Kruskal-Wallis test $^{***}p = 0.0098$; Dunn's post-hoc test $^{*}p < 0.05$ for $Cd^{2+}$). **F.** CSD propagation speed in control (median 3.45 mm/min, mean±SEM 3.57±0.18 s; $n = 30$), with Gabazine (5.28, 5.08±0.44 mm/min, $n = 6$), with CPP+CNQX (1.39, 1.51±0.11 mm/min, $n = 16$), CPP+CNQX +Gabazine (2.66, 2.97±0.21 mm/min, $n = 9$) or $Cd^{2+}$ (0.9, 1.03±0.13 mm/min, $n = 10$) (Kruskal-Wallis test $^{****}p < 0.0001$; Dunn's post-hoc test $^{*}p = 0.011$ for CPP+CNQX and $^{****}p < 0.0001$ for $Cd^{2+}$).

initiation, which cannot be performed with classical methods of CSD induction, we used spatial optogenetic illumination, both continuous (Video 6 and Video 9) and discontinuous (100 ms, 5 Hz; Video 7), to specifically control the site of CSD induction and allow recordings within the site (Fig. 2.8 A, B). Both illumination methods induced CSD with features that were similar to that induced with the large field of illumination, although success rate was smaller (30-35 % vs about 80 %). Our results show that $[K^+]_{out}$ slowly and progressively increased during illumination, reaching 12 mM when CSD was ignited (identified as the end of the multi-unit activity) (Fig. 2.8 C, D, Fig. $S_6$). Notably, this phase of slow increase was not observed in the CSD propagating in the cortical tissue outside the initiation site (Fig. $S_6$). However, at CSD ignition, $[K^+]_{out}$ was similar to that observed at the site of initiation (Fig. $S_6$). This suggests that at CSD initiation, $[K^+]_{out}$ can progressively accumulate near neuronal membranes, until CSD ignition threshold is reached. We confirmed this hypothesis by inducing CSD with focal applications of 12 mM KCl in a neocortical area that was comparable in size to that of spatial optogenetic illuminations (Fig. 2.8 E and Video 8).

In order to study the dynamics of the firing of both GABAergic interneurons and pyramidal neurons in the site of CSD initiation, we performed juxtacellular-loose patch voltage recordings during CSD initiation (Fig. 2.8 F and Video 9). Neurons were recorded in the initiation site during optogenetic triggering of CSD, using spatial illumination (34 % success rate for CSD induction, 121 slices). Only cells that were located in the core of CSD induction site were selected for analysis ($n = 7$ GABAergic neurons, $n = 5$ pyramidal neurons). Occasionally pair recordings of GABAergic and pyramidal neurons were achieved ($n = 2$ pairs, Fig. 2.8 F). GABAergic neurons begun to fire early after the illumination (60.5±11.3 s mean±SEM, 52.3 s median, before the beginning of CSD initiation, $n = 7$) and fired at moderate frequency (on average 48.4±6.8 Hz, mean±SEM) till their firing frequency abruptly increased (to 349±36 Hz, which was comparable to the maximal firing frequency observed in Fig. 2.2 C) few seconds before CSD initiation. Thus, GABAergic neurons fired during the first (longer) phase at just about 15 % of their maximal firing frequency. Pyramidal neurons fired later during the illumination, just for few seconds before CSD initiation (2.9±0.6 s mean±SEM, median 3.5 s, $n = 5$; $p = 0.006$ compared to GABAergic neurons, Mann-Whitney test). Therefore, the firing of the GABAergic neurons at moderate frequency is implicated in the slow $K^+$ build-up observed at the site of initiation, whereas pyramidal neurons contribute later to the $K^+$ build-up, for few seconds before CSD initiation, when the whole network is engaged.

### 2.2.5 Overactivation of GABAergic neurons or $Na_V1.1$ can initiate/facilitate CSD in vivo

We performed experiments to evaluate the effect of overactivation of GABAergic neurons or $Na_V1.1$ in vivo, a condition in which blood circulation, long range connections and neuromodulations are present. For optogenetic experiments, we illuminated with an optical fiber the somatosensory cortex of VGAT-ChR2 mice, monitoring CSD by LFP recordings (Fig. 2.9 A - C); CSD was induced in 50 % of VGAT-ChR2 mice and never in control littermates. Moreover, we tested the effect of acute injection of Hm1a into the somatosensory cortex (Fig. 2.9 D). We initially directly injected Hm1a (10 nM, $N = 7$, or 100 nM, $N = 5$), but we did not observe CSD with LFP recordings (1.3 mm rostral of the site of injection). In further experiments, we evaluated the effect of Hm1a on CSD triggered by injecting 130 mM KCl. Notably, Hm1a 10 nM induced a 20 % reduction in the latency to CSD induction, whereas control injections with ACSF did not modify it (Fig. 2.9 E, G). Moreover, injection of Hm1a 100 nM induced a 35 % reduction in latency (117 s median, 108±15 s, mean±SEM, before Hm1a 100 nM; 64 s, 70±14 s upon Hm1a injection; $N = 7$,

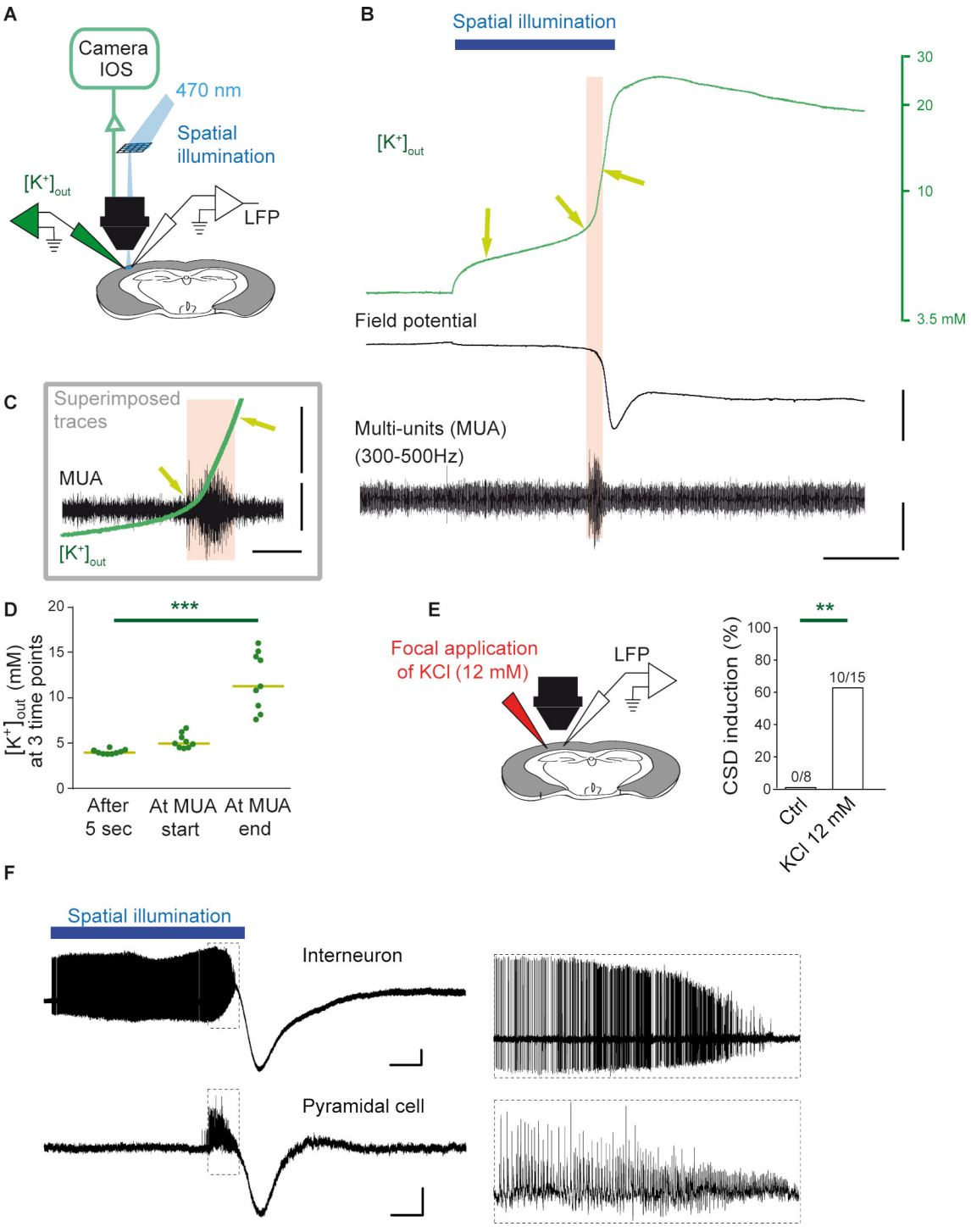


**Figure 2.8: Spike-induced increase of $[K^+]_{out}$ is directly involved in CSD induction by spatial illumination. A.** Experimental setting for spatial 470 nm illumination used to specifically control the area of CSD induction, allowing $[K^+]_{out}$, LFP and IOS recordings at the site of CSD initiation. See Video 6 and Video 7. **B.** $[K^+]_{out}$ dynamics before and during CSD, correlated to the LFP and multi-unit activity (MUA), which were paroxysmal at CSD initiation. Only the first component of the CSD is shown. **C.**. Enlargement and superposition of $[K^+]_{out}$ and MUA traces shown in B. **D.** Quantifications of $[K^+]_{out}$ after the first 5 s of illumination, at the beginning of the paroxysmal MUA firing and at the end of the MUA firing (beginning of the depolarizing block) (arrows in B and C), $n = 9$ slices. Bars represent medians. Friedman test ($p < 0.0001$) and Dunn's post-test (*** $p < 0.001$). **E.** Success rate of CSD *(continued next page)*

**Figure 2.8** ***(previous page)*:** induced by long-lasting puff of 12 mM KCl (dissolved in 125 mM NaCl), which corresponds to the $[K^+]_{out}$ at the beginning of the depolarizing block, compared to a control 137 mM NaCl solution (Ctrl; Fisher exact test, ** $p = 0.0027$). Injection area: $0.75 \pm 0.11\,mm^2$ ($n = 10$ slices with successful CSD inductions). See Video 8. **F.** Representative simultaneous juxtacellular-loose patch recordings of a GABAergic interneuron (upper trace) and of a pyramidal neuron (bottom trace) at the site of initiation of CSD induced with spatial optogenetic illumination as in (A) (see Video 9); the negative deflection is the LFP generated by the CSD and recorded by the juxtacellular electrode; scale bars 500 µV, 5 s. The right insects show the firing (1.5 Hz highpass filtered to remove the slow components) immediately before the CSD initiation (highlighted in the traces on the left with the dashed boxes). See text for $n$ and statistics.

Wilcoxon Signed Ranks Test $p = 0.03$; not shown in the figure). Therefore, these data confirm the results obtained in brain slices, showing that overactivation of GABAergic neurons or $Na_V1.1$ can lead to/facilitate CSD induction also in vivo.

## 2.3 Discussion

We have identified and characterized a mechanism of CSD initiation specific of the neocortex, showing in acute experimental models a causal relationship between $Na_V1.1$ gain of function leading to initial hyperactivity of GABAergic neurons, progressive engagement of the whole neuronal network and CSD ignition, driven by the progressive increase of $[K^+]_{out}$ at the initiation site and in which synaptic transmission is not necessary (see Graphical abstract). This mechanism was supported by simulations obtained with a computational model. CSD was induced in the neocortex both by activation of $Na_V1.1$ with the specific toxin Hm1a [36], which mimics gain-of-function FHM3 mutations and increases excitability of cortical GABAergic neurons, and by direct optogenetic activation of GABAergic neurons. This is consistent with the key role of $Na_V1.1$ in GABAergic neurons' excitability and with the effect of FHM3 mutations, which cause gain of function of $Na_V1.1$ and can induce an increase of the persistent $Na^+$ current similar to that observed with Hm1a [1, 2, 5–7, 12, 32–34, 39]. Notably, it has been recently reported that Hm1a rescued the hypoexcitability of hippocampal GABAergic neurons and the severity of the epileptic phenotype in epileptic *Scn1a*$^{+/-}$ knock-out mice, but it did not modify firing properties of wild type hippocampal GABAergic neurons in brain slices [47]. However, we found that application of Hm1a at a concentration at which it is specific for $Na_V1.1$ can induce in neocortical slices from wild type mice hyperexcitability of GABAergic neurons, in particular fast spiking ones, whereas the firing properties of glutamatergic pyramidal neurons were not significantly modified, consistent with the different role of $Na_V1.1$ in the two neuronal subtypes and with a specific role of GABAergic neurons in CSD initiation induced by Hm1a (see Supplementary Methods "Brain Slices: electrophysiological recordings" for more information on this issue).

Additionally, we found that the loss-of-function of $Na_V1.1$ in slices from VGAT-ChR2-*Scn1a*$^{+/-}$ mice [22] inhibited the initiation of CSD by optogenetic stimulation, consistent with the involvement of $Na_V1.1$ and of GABAergic neurons' hyperexcitability in the mechanism of initiation. Importantly, different than what has been observed in some other epileptic models [48–51], this effect is not caused by the inhibition of CSD generation induced by the epileptic network, because threshold of CSD triggered by puffs of 130 mM KCl was not modified in VGAT-ChR2-*Scn1a*$^{+/-}$ slices. Opposite to CSD inhibition, experiments in anesthetized mice have shown that $Na_V1.1$ loss-of-function facilitates SD in the brainstem, which can cause post-seizure sudden death (SUDEP) in *Scn1a*$^{+/-}$ mice

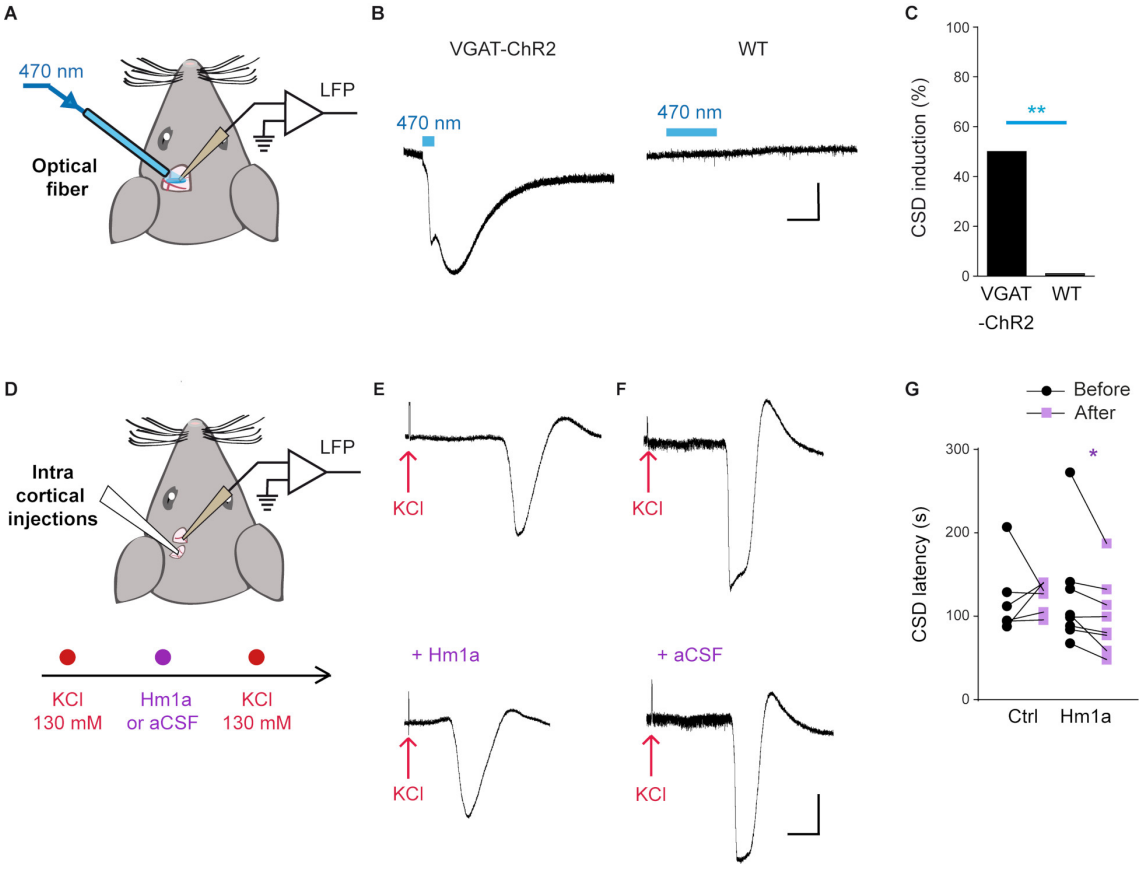


**Figure 2.9: CSD induction in vivo. A.** Experimental design of optogenetic induction: blue light optogenetic stimulation (100 Hz trains of 0.8 ms pulses) was applied to the barrel cortex of anesthetized mice with an optical fiber through a craniotomy; DC field potential recordings were performed with a glass pipette (Ag/AgCl electrode). **B.** Representative field potential traces of CSD in a VGAT-ChR2 mouse, whereas there was no response in a control WT mouse. **C.** Proportion of optogenetic CSD induction in VGAT-ChR2 (5/10) and control mice (0/13, including WT, $N = 5$, VGAT.Cre, $N = 4$, and ChR2.lox $N = 4$. Fisher's exact test; ** $p = 0.0075$). **D.** Experimental design of Hm1a injections into the somatosensory cortex: CSD was induced by injecting 130 mM KCl with a 30-gauge needle and monitored by DC field potential recordings (1.3 mm more rostral), Hm1a or ACSF (negative control) were injected at the same location after CSD induction and then a second CSD was induced by injecting again 130 mM KCl. **E.** Representative CSD traces obtained before (top) and after (bottom) the injection of 10 nM Hm1a. **F.** Representative traces obtained before (top) and after (bottom) the injection of ACSF. **G.** Comparison of CSD latency observed before and after injection of ACSF (control) or Hm1a 10 nM: 103 s (median), 121±18 s (mean±SEM) before ACSF; 129 s, 123±8 s after ACSF ($N = 6$; Wilcoxon Signed Ranks Test $p = 0.69$); 100 s, 123±23 s before Hm1a 10 nM; 90 s, 99±16 s after Hm1a 10 nM ($N = 8$; Wilcoxon Signed Ranks Test; * $p = 0.016$). Scale bars 5 mV, 1 min for all the panels.

because of block of cardiorespiratory pacemaking [52]. However, this apparent discrepancy could be consistent with different mechanisms of initiation and propagation. In fact, contrary to CSD initiation, we observed in VGAT-ChR2-*Scn1a*$^{+/-}$ slices a trend towards increased propagation velocity for optogenetic-induced CSD and higher propagation velocity for KCl-induced CSD. This effect could facilitate the generation/propagation of SD in the brainstem upon induction of epileptic discharges leading to post-ictal depression in the neocortex, as observed in *Scn1a*$^{+/-}$ mice by [52].

We have also demonstrated that CSD initiation by direct GABAergic neurons' hyperactivation is not dependent on synaptic transmission. In fact, the only manipulations

able to inhibit CSD initiation were the generalized block of action potentials' generation (applying TTX) or the reduction of GABAergic neurons' excitability (in brain slices from VGAT-ChR2-*Scn1a*$^{+/-}$ mice), consistent with the simulations that we obtained in [35]. Differently than initiation, CSD propagation was inhibited by blocking $Ca^{2+}$ channel-dependent synaptic release or glutamate receptors, but not by blocking GABA-A receptors. These results show that mechanisms linked to increased GABAergic synaptic transmission [43–46], possibly induced by GABAergic neurons' hyperexcitability, are not involved in CSD. Moreover, glutamatergic transmission has an important role in propagation, but not in initiation when GABAergic neurons are over-activated. Overall, these results are consistent with different mechanisms of initiation and propagation. Notably, numerous studies have performed pharmacological investigations of mechanisms of CSD triggered with classic methods, revealing a complex picture with results that often are specific for different methods and for initiation vs. propagation [9], consistent with different cellular/molecular mechanisms. Optogenetic experiments with spatial illumination (Fig. 2.8; Fig. $S_6$) allowed us to investigate the properties of the site of initiation modeling the effect of FHM3 mutations. We have found that progressive $K^+$ build-up induced by neuronal firing is a key factor at the site of CSD initiation by hyperactivation of GABAergic neurons, and chelation of extracellular $K^+$ blocks CSD initiation. In our experiments, GABAergic neurons at the site of initiation initially fire at moderate frequency, sharply increasing their activity few seconds before CSD initiation, when the whole network is engaged. This is a novel mechanism of CSD induction, different in comparison with that implicated in models of FHM1 and FHM2, in which it has been proposed that excessive glutamate release/accumulation is the major pathological dysfunction [29–31]. Notably, a recent optogenetic CSD model of glutamatergic neurons' hyperactivation probably mimics mechanisms at play in FHM1 and FHM2, including the necessity of NMDA receptor activation for CSD initiation [53]. Consistent with a different mechanism in comparison with FHM3, FHM1 and FHM2 patients often show complex phenotypes that are more severe than those of FHM3 and include several neurologic/psychiatric co-morbidities, including seizures that herald or are concomitant with hemiplegic migraine attacks, as well as peri-ictal death [16, 54]. In FHM3 there are no patients with these complex phenotypes, and in the few cases in which seizures have been reported, they are always independent from migraine attacks and present in different developmental windows, as we have recently reviewed [12]. Supporting these clinical observations, a recent work has reported that the knock-in mouse model of the FHM3 L263V $Na_V1.1$ mutation shows spontaneous CSD events, but not seizures [17]. Moreover, migraine or hemiplegia are not part of the phenotypes of epileptogenic $Na_V1.1$ mutations that cause loss-of-function of the channel and hypoexcitability of GABAergic neurons [55–57], consistent with different pathologic mechanisms. Congruously, we have never observed ictal-like epileptiform activities in our experiments, although it has been shown that ictal-like activities generated by application of convulsants in brain slices could be enhanced/induced [45, 58] or, depending on the brain region, inhibited [59] by the optogenetic activation of GABAergic neurons. This probably reflects the requirement of a network that already generates epileptic activities for induction/modulation of these activities by the activation of GABAergic neurons. Nevertheless, it is interesting to note that, in some of those studies, different mechanisms of onset (some requiring activation of GABAergic neurons, others activation of glutamatergic neurons) have been identified for epileptiform activities that appear phenomenologically similar [45]. This could be the case, as we have already highlighted, also for network activities that lead to CSD initiation, which could be specific for different types of migraine, in particular for FHM3 compared to FHM1 and FHM2.

In our experiments, latencies to CSD induced by activation of GABAergic neurons

were of few tens of seconds. In most of the classical experimental models, CSD is induced with strong stimuli (e.g. injections of KCl in the tens of mM to molar range, the latter well beyond pathophysiological limits) [9], which often result in shorter latencies most likely because they do not reproduce the complete dynamic process of CSD onset at the initiation site, mimicking conditions that are those of the generalized depolarization phase. There is no information about activities of single neurons leading to CSD induction in migraine patients. As in other episodic and paroxysmal disorders [60], pathologic dysfunctions of migraine are probably controlled by homeostatic mechanisms in the period between attacks, and different factors (e.g. hormonal/neuromodulatory changes or increase of incoming neuronal signals from the periphery) may affect neuronal excitability and activities of cortical networks, triggering CSD induction and migraine attacks. It can be hypothesized that, in the restricted volume of cortex in which CSD is initially initiated, these factors could weaken homeostatic controls and hyperexcitable GABAergic neurons could be hyperactivated (at moderate firing frequency) for tens of seconds (even intermittently, as in Video 7), similar to our acute model. Interestingly, neurons can show early and long lasting increase of activity also in other episodic neurological disorders, as observed for instance with single unit recordings in epileptic foci of patients [61], in which increased neuronal activity can begin minutes before the attack.

The paper by Auffenberg et al. [39] provides results that complement our work. In fact, the authors studied in a knock-in mouse model the pathogenic mechanisms of the human FHM3 L1649Q *SCN1A* mutation, which we previously studied in expression systems [6]. They demonstrated in an animal model that L1649Q induces $Na_V1.1$ gain-of-function (in particular because of slowed and incomplete inactivation, an effect that is similar to that of Hm1a), which causes enhanced firing of GABAergic interneurons, in particular PV-positive fast spiking ones (consistent with our experiments showing that their overactivation can be sufficient to trigger CSD), without modifications of pyramidal neuron firing, leading in vivo to facilitation of CSD induction. Importantly, our work provides more than additional evidences, because it discloses detailed mechanisms of CSD initiation that cannot be studied with standard models, and shows that acute hyperactivation of $Na_V1.1$/GABAergic neurons is sufficient to induce CSD in the normal (non-pathologic) neocortex. Future studies for investigating even better detailed pathological mechanisms of FHM3 using the now available knock-in mouse models are warranted. However, in comparison with chronic models (i.e. genetic), our acute models allowed us to study mechanisms and dynamics of CSD initiation and demonstrate that other possible pathological modifications (e.g. remodeling of gene expression) are not necessary.

## 2.4 Methods

See Supplementary Methods for more details.

### 2.4.1 Animal care and mouse lines

All efforts were made to minimize the number of animals used and their suffering. They were group housed (5 mice per cage, or 1 male and 2 females per cage for breeding) on a 12 h light/dark cycle, with water and food *ad libidum*. Mouse lines have been obtained from Jackson laboratory (JAX, USA), besides GAD67-GFP knock-in mice [62], which have been obtained from Yuchio Yanagawa (Gunma University, Maebashi, Japan).

To have specific expression of channelrhodopsin-H134R/tdtomato in GABAergic neurons, most of the experiments have been performed with male and female double hemizygous transgenic mice VGAT-hChR2(H134R)/tdtomato (VGAT-ChR2 in the text) and control littermates (F1 generation). They were obtained by mating hemizygous females

loxP-STOP-loxP-hChR2(H134R)-tdtomato (Ai27D, B6.Cg-Gt(ROSA)26Sortm27.1(CAG-COP4*H134R/tdTomato)Hze/J, JAX n°012567) [63] with transgenic males (to avoid off-target Cre expression in the female germline) hemizygous for the Viaat-Cre transgene (Cre recombinase expression driven by the vesicular GABA transporter, VGAT, promoter) (B6.FVB-Tg(Slc32a1-Cre)2.1Hzo/FrkJ, JAX n°017535), line 2.1 in [38]. To avoid germline transmission of recombined floxed alleles (see `www.jax.org/strain/017535`), we have never used VGAT-ChR2 F2 offspring. VGAT-Cre mice have been previously used for obtaining specific expression of floxed alleles in GABAergic neurons [38, 64–67]. To evaluate the effect of a reduction of $Na_V1.1$ expression in interneurons, we crossed double hemizygous VGAT-ChR2 mice with heterozygous $Na_V1.1$ knock-out mice ($Scn1a^{+/-}$) [22]. To express ChR2 selectively in parvalbumin positive (PV+) neurons, we crossed hemizygous loxP-STOP-loxP-hChR2(H134R)-tdtomato female mice with homozygous Pvalb-IRES-Cre (JAX n°017320) male mice. Moreover, for immunohistochemistry, we used mice expressing a floxed td-tomato transgene (Ai9, B6;129S6-Gt(ROSA)26Sortm9(CAG-tdTomato)Hze/J; Jackson Lab. n°007905) as a cell filling reporter line, because it was difficult to identify hChR2(H134R)/tdtomato expressing cells with the plasma membrane fluorescence of the tagged ChR2 in VGAT-ChR2 mice.

All mouse lines were in the C57BL/6J background (>10 generations, Charles River, USA), besides $Scn1a^{+/-}$ mice that were in a mixed background (C57BL/6J-CD1 85:15%).

Offspring was genotyped either by PCR, following the standard JAX protocols, using our standard protocol for $Scn1a^{+/-}$ knock-out mice [68] or, for mice with cell filling fluorescent protein, controlling the fluorescence of newborn mice with a Dual Fluorescent Protein Flashlight (NightSea, USA). We used mice of both sexes, 4-6 weeks old for ex-vivo experiments and 4-8 weeks old for in vivo experiments.

### 2.4.2 Preparation of brain slices, electrophysiological recordings and imaging in slices

Brain slices were prepared as in [24, 37], patch-clamp recordings performed as in [24, 37], local field potential recordings as in [24, 37, 68], recordings with $K^+$ selective electrodes as in [69] and intrinsic optical signal (IOS) imaging as in [37]. See Supplementary Methods for more details.

### 2.4.3 Optogenetic illumination of brain slices

Activation of ChR2 was obtained illuminating brain slices through the 4x objective with blue light generated using a white light source (Intensilight, Nikon, Japan) and appropriate filters. Spatial illumination was performed with a digital micromirror device (DMD)-based patterned photostimulator (Polygon 400, Mightex, Canada). We used either continuous illumination or trains of illumination (5 Hz, duty cycle 50 %). See Supplementary Methods for more details.

### 2.4.4 Induction of CSD by application of KCl in brain slices

Brief puffs of KCl (130 mM) and Fastgreen (0.1 %, SIGMA-Aldrich, USA; to visualize the injection area) were applied in the superficial cortical layers (layers 2-3) with a glass micropipette (2-4 MΩ) connected to an air pressure injector, as in [37]. See Supplementary Methods for more details.

### 2.4.5 Processing and analyses of IOS images

CSD waves obtained by intrinsic optical imaging were processed and analyzed with ImageJ-Fiji as in [37]. See Supplementary Methods for more details.

### 2.4.6 Immunohistochemistry

Brains were fixed with paraformaldehyde 4 %. Experiments were performed on 40 µm coronal sections. Image acquisitions were obtained with a confocal laser-scanning microscope (FV10i, Olympus, Japan). See Supplementary Methods for more details.

### 2.4.7 In vivo experiments

Mice were deeply anesthetized with ketamine/xylazine (100 mg/kg and 5 mg/kg, respectively) and DC field potentials were recorded with a glass pipette filled with ACSF, inserted into the barrel cortex through a craniotomy. Optogenetic stimulations were applied on the surface of the cortex with a 400 µm diameter optical fiber, connected to a 470 nm LED light source (100 Hz trains of 0.8 ms pulses); Hm1A or control ACSF were injected with a 30-gauge needle. Mice were sacrificed at the end of the recordings by cervical dislocation.

### 2.4.8 Patch-clamp recordings in cell-lines

Plasmids were propagated, cells transfected, whole-cell patch-clamp recordings performed and analyzed as in [6, 70]. See Supplementary Methods for more details.

### 2.4.9 Pharmacological agents and chemicals

Gabazine, Isoguvacine and CdCl2 were bought from Sigma-Aldrich (USA), CNQX, VU0240551 and VU0463271 from Tocris Bioscience (UK), CPP and TTX-citrate from Alomone labs (Israel), Kryptofix2.2.2 from Fisher Scientific (USA). Synthetic Hm1a was purchased from Smartox S.A.S (France). All other chemicals were purchased from Sigma-Aldrich. Drugs were applied for 15 min before to test the induction of CSD.

### 2.4.10 Computational model

The model of two coupled neurons, GABAergic and pyramidal, was based on the one we developed in [35]. Here, we refined the model introducing the modifications described in the Supplementary Methods. A complete description of the model is given in Section 3.2.2 of Chapter 3, and Table 3.3 lists the differences between the current version and the extended version of Chapter 3, which additionally models the epileptogenic mutations of $Na_V1.1$.

We performed the numerical simulations with the software XPPAUT [71]. The code is available in ModelDB [72] at `http://modeldb.yale.edu/267157`.

### 2.4.11 Statistics

For experiments with mice, we used data pooled from at least 3 animals per condition (including negative controls) to ensure reproducibility of results. Mice were used after genotyping and littermates were negative controls; in mice expressing fluorescent proteins, systematic tests using a flashlight were performed before the experiment to confirm the genotyping results. Statistical tests were performed with Origin 8 (OriginLab) and R. Fisher's exact test followed by a pairwise test adjusted with Bonferroni correction was performed for the analysis of contingency tables. Two-tailed nonparametric Mann–Whitney

U test, Kruskal-Wallis test and Friedman 1-way ANOVA were performed because groups are not large enough to accurately verify normality and equality of variance. Dunn's non-parametric comparison and Bonferroni correction (comparisons with the control group) were used for post hoc tests when appropriate. The one sample Wilcoxon signed-rank nonparametric one-sided test was used to evaluate the effect of Hm1a on $Na^+$ currents in cell lines (fold increase of INaP larger than 0) and the paired Wilcoxon Signed Rank Test was used for effect of Hm1a on firing in brain slices. Differences were considered significant at $p < 0.05$.

### 2.4.12 Study approval

Experiments were carried out according to the ARRIVE guidelines and the European directive 2010/63/UE and approved by institutional and ethical committees (approval C06-152-5 and 04551.02 for France, 711/2016-PR for Italy).

## 2.5 Acknowledgements

We thank Frederic Brau for his skillful expertise on imaging and image processing, Michelle Studer and Pascal Ezan for advices on immunohistochemistry experiments, Etienne Audinat for insightful discussions and advices, and Yuchio Yanagawa for donating GAD67-GFP knock-in mice. Our laboratory is member of the "Fédération Hospitalo-Universitaire" FHU-INOVPAIN and of the Neuromod Institute (Université Cote d'Azur, France; www.univ-cotedazur.fr/neuromod). This research was supported by the Investissements d'Avenir-Laboratory of Excellence "Ion Channels Science and Therapeutics" (grant LabEx ICST ANR-11-LABX-0015-01 to MM), University Côte d'Azur (grant IDEX Jedi ANR-15-IDEX-01 to MM) and the European Commission project DESIRE (grant n. EFP7-602531 to MM). SZ was a Ph.D. student of the "Ecole doctorale 85" and received a Ph.D. fellowship from the French Research Ministry (MENRT).

## 2.6 Videos and supplementary material

Videos and supplementary material are available at https://www.jci.org/articles/view/142203/.

# Chapter 3

# Modeling $Na_V1.1$ epilepsy and migraine mutations in a microcircuit with dynamic ion concentrations

The content of this chapter is published in [26]: L. Lemaire et al. "Modeling $Na_V1.1$/*SCN1A* Sodium Channel Mutations in a Microcircuit with Realistic Ion Concentration Dynamics Suggests Differential GABAergic Mechanisms Leading to Hyperexcitability in Epilepsy and Hemiplegic Migraine". *PLOS Computational Biology* 17.7 (July 27, 2021), e1009239.

## 3.1 Introduction

The model presented in Chapter 2 builds up upon previous work. In [35], we developed a two-neuron (GABAergic and pyramidal) conductance-based model, which partially accounted for ion concentration dynamics. We assumed that FHM3 mutations cause hyperactivity of the GABAergic neuron, and found that it promotes CSD initiation in the model. The simulations highlighted the key role of spiking-induced extracellular potassium build-up. In Chapter 2, we substantially improved the model from [35]: we explicitly modeled FHM3 mutations, and modeled ion concentration dynamics more consistently. A detailed description of the modifications compared to [35] is given in Section 3.2.2. In this chapter, we extend the model further by adding the implementation of $Na_V1.1$ epileptogenic mutations, as described in Section 3.2.2.7.

Several other modeling studies have addressed issues similar to those of interest here, using conductance-based models with dynamic ion concentrations. For instance, Florence et al. [73] suggested that extracellular potassium is fundamental for epileptiform bursting and spreading depolarization [73]. Wei et al. proposed a unified model for studying those two pathological behaviors [74]. Dahlem et al. modeled FHM3 mutations and concluded that they render gray matter tissue more vulnerable to spreading depolarization.

The main novelty of our approach is that we implemented $Na_V1.1$ mutations on a GABAergic neuron, and analyzed their effects on a microcircuit formed by the GABAergic neuron and an interconnected pyramidal neuron. This allowed us to take into account the inhibitory effect of GABAergic neurons on pyramidal neurons. We studied both FHM3 and epileptogenic mutations within the same framework, modifying only two relevant parameter values. We present original experimental results that support predictions of the model and we put the model simulations into perspective with other experimental works. In particular, we qualitatively compared them with results we obtained using the Hm1a $Na_V1.1$ enhancer to mimic FHM3 mutations (Chapter 2) and with results of Freilinger et

al. [39] who generated the knock-in mouse model of the L1649Q FHM3 mutation studying effects on microcircuit features.

## 3.2 Materials and methods

### 3.2.1 Ethics Statement

Experiments with mice were carried out according to the European directive 2010/63/UE and approved by institutional and ethical committees (PEA216-04551.02, France; 711/2016-PR, Italy). All efforts were made to minimize the number of animals used and their suffering. Animals were group housed (5 mice per cage, or 1 male and 2 females per cage for breeding) on a 12 h light/dark cycle, with water and food ad libitum.

### 3.2.2 The model

We developed a conductance-based model formed by a pair of neurons: a GABAergic interneuron and a glutamatergic pyramidal neuron. This model takes into account the dynamics of ion concentrations. It is an essential feature here, since ion gradients, and hence reversal potentials, are modified during migraine and epilepsy attacks. The two neurons are thus coupled through variations of extracellular ion concentrations, in addition to synaptic connections. We implemented several ion transport proteins, such as voltage-gated channels, cotransporters, pumps and synaptic channels, which are sketched in Fig. 3.1. The dynamics of the state variables is given by a system of 18 differential equations: System (3.1). The variables are listed in Table 3.1, the parameters and their default values in Table 3.2. We performed numerical simulations of the model with the software package XPPAUT [71], using a 4th-order Runge-Kutta scheme. The code is available in ModelDB [72] at `http://modeldb.yale.edu/267047`.

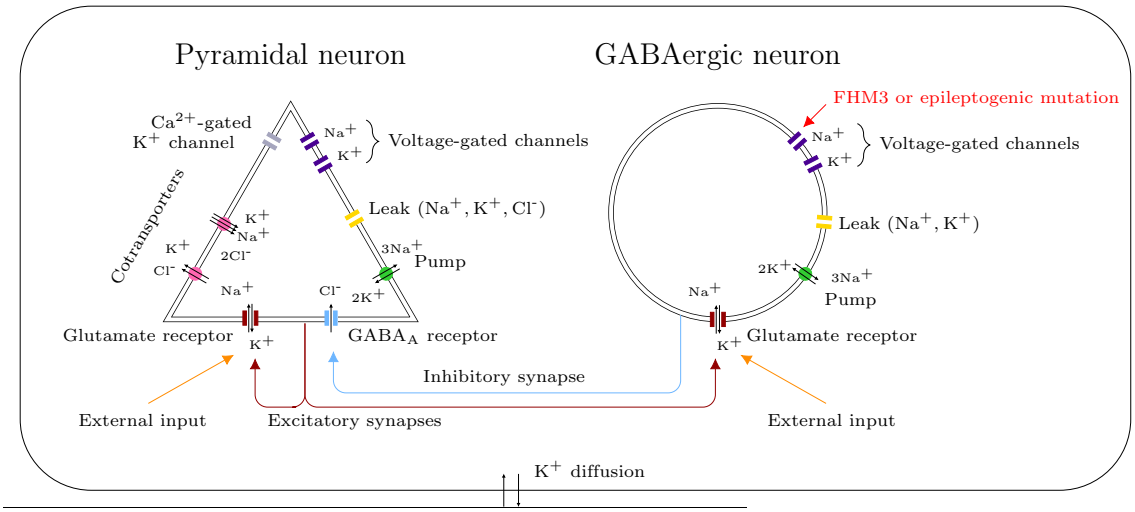


**Figure 3.1: Schematic representation of the model.** Consider a pair of interconnected neurons in a closed volume. We modeled a GABAergic synapse from the GABAergic neuron to the pyramidal one, a glutamatergic synapse from the pyramidal neuron to the GABAergic one and a glutamatergic autapse from the pyramidal neuron to itself. The ion transport mechanisms represented here generate transmembrane ionic currents, which modify the membrane potentials of the neurons and the ion concentrations in the different compartments. The diffusion of extracellular potassium takes into account both passive diffusion and glial buffering. We modeled external stimuli, which reflect the activity of the surrounding network or mimic experimental depolarizations, with glutamate inputs on the glutamatergic receptors. The implementation of $Na_V1.1$'s genetic mutations affects only the GABAergic neuron.

$$C\,\frac{\mathrm{d}v_\mathrm{e}}{\mathrm{d}t} = -\,I_{\mathrm{Na,e}} - I_{\mathrm{K,e}} - I_{\mathrm{Cl,e}} \tag{3.1a}$$
$$\frac{\mathrm{d}m_\mathrm{e}}{\mathrm{d}t} = \alpha_{m,\mathrm{e}}(1-m_\mathrm{e}) - \beta_{m,\mathrm{e}}\,m_\mathrm{e} \tag{3.1b}$$
$$\frac{\mathrm{d}h_\mathrm{e}}{\mathrm{d}t} = \alpha_{h,\mathrm{e}}(1-h_\mathrm{e}) - \beta_{h,\mathrm{e}}\,h_\mathrm{e} \tag{3.1c}$$
$$\frac{\mathrm{d}n_\mathrm{e}}{\mathrm{d}t} = \alpha_{n,\mathrm{e}}(1-n_\mathrm{e}) - \beta_{n,\mathrm{e}}\,n_\mathrm{e} \tag{3.1d}$$
$$\frac{\mathrm{d}[\mathrm{K}^+]_\mathrm{e}}{\mathrm{d}t} = -\,\gamma_\mathrm{e}\,I_{\mathrm{K,e}} \tag{3.1e}$$
$$\frac{\mathrm{d}[\mathrm{Na}^+]_\mathrm{e}}{\mathrm{d}t} = -\,\gamma_\mathrm{e}\,I_{\mathrm{Na,e}} \tag{3.1f}$$
$$\frac{\mathrm{d}[\mathrm{Cl}^-]_\mathrm{e}}{\mathrm{d}t} = \gamma_\mathrm{e}\,I_{\mathrm{Cl,e}} \tag{3.1g}$$
$$\frac{\mathrm{d}[\mathrm{Ca}^{2+}]_\mathrm{e}}{\mathrm{d}t} = -\,\frac{\gamma_\mathrm{e}}{2}\,I_{\mathrm{Ca,e}} - \frac{[\mathrm{Ca}^{2+}]_\mathrm{e}}{\tau_{\mathrm{Ca}}} \tag{3.1h}$$
$$\frac{\mathrm{d}s_\mathrm{e}}{\mathrm{d}t} = -\,\frac{1}{\tau_\mathrm{e}}s_\mathrm{e}\,, \quad \text{if } v_\mathrm{e} = v_{\mathrm{thres,e}} \text{ and } \frac{\mathrm{d}v_\mathrm{e}}{\mathrm{d}t} > 0 \text{ then } s_\mathrm{e} \leftarrow 1 \tag{3.1i}$$

$$C\,\frac{\mathrm{d}v_\mathrm{i}}{\mathrm{d}t} = -\,I_{\mathrm{Na,i}} - I_{\mathrm{K,i}} \tag{3.1j}$$
$$\frac{\mathrm{d}h_\mathrm{i}}{\mathrm{d}t} = \frac{h_{\infty,\mathrm{i}} - h_\mathrm{i}}{\tau_{h,\mathrm{i}}} \tag{3.1k}$$
$$\frac{\mathrm{d}n_\mathrm{i}}{\mathrm{d}t} = \frac{n_{\infty,\mathrm{i}} - n_\mathrm{i}}{\tau_{n,\mathrm{i}}} \tag{3.1l}$$
$$\frac{\mathrm{d}[\mathrm{K}^+]_\mathrm{i}}{\mathrm{d}t} = -\,\gamma_\mathrm{i}\,I_{\mathrm{K,i}} \tag{3.1m}$$
$$\frac{\mathrm{d}[\mathrm{Na}^+]_\mathrm{i}}{\mathrm{d}t} = -\,\gamma_\mathrm{i}\,I_{\mathrm{Na,i}} \tag{3.1n}$$
$$\frac{\mathrm{d}s_\mathrm{i}}{\mathrm{d}t} = -\,\frac{1}{\tau_\mathrm{i}}s_\mathrm{i}\,, \quad \text{if } v_\mathrm{i} = v_{\mathrm{thres,i}} \text{ and } \frac{\mathrm{d}v_\mathrm{i}}{\mathrm{d}t} > 0 \text{ then } s_\mathrm{i} \leftarrow 1 \tag{3.1o}$$

$$\frac{\mathrm{d}[\mathrm{K}^+]_\mathrm{o}}{\mathrm{d}t} = \frac{\mathrm{Vol_e}}{\mathrm{Vol_o}}\gamma_\mathrm{e}\,I_{\mathrm{K,e}} + \frac{\mathrm{Vol_i}}{\mathrm{Vol_o}}\gamma_\mathrm{i}\,I_{\mathrm{K,i}} - I_{\mathrm{K,diff}} \tag{3.1p}$$
$$\frac{\mathrm{d}[\mathrm{Na}^+]_\mathrm{o}}{\mathrm{d}t} = \frac{\mathrm{Vol_e}}{\mathrm{Vol_o}}\gamma_\mathrm{e}\,I_{\mathrm{Na,e}} + \frac{\mathrm{Vol_i}}{\mathrm{Vol_o}}\gamma_\mathrm{i}\,I_{\mathrm{Na,i}} \tag{3.1q}$$
$$\frac{\mathrm{d}[\mathrm{Cl}^-]_\mathrm{o}}{\mathrm{d}t} = -\,\frac{\mathrm{Vol_e}}{\mathrm{Vol_o}}\gamma_\mathrm{e}\,I_{\mathrm{Cl,e}} \tag{3.1r}$$

This model is based upon previous work [35], to which we made the following key improvements:

1. We modeled $\mathrm{Na_V}1.1$'s FHM3 and epileptogenic mutations, considering their effect on the GABAergic neuron. The implementation of those mutations is detailed in Section 3.2.2.6.

2. We propose a more consistent modeling of ion concentration dynamics. In [35], the reversal potentials of the GABAergic neuron were assumed to be constant, and

**Table 3.1: Variables of System (3.1).**

| Variable | Description | Unit |
|---|---|---|
| $t$ | Time | ms |
| | **Pyramidal neuron** | |
| $v_e$ | Membrane potential | mV |
| $m_e$ | Sodium activating gating variable | |
| $h_e$ | Sodium inactivating gating variable | |
| $n_e$ | Potassium activating gating variable | |
| $[K^+]_e$ | Intracellular potassium concentration | mM |
| $[Na^+]_e$ | Intracellular sodium concentration | mM |
| $[Cl^-]_e$ | Intracellular chloride concentration | mM |
| $[Ca^{2+}]_e$ | Intracellular calcium concentration | mM |
| $s_e$ | Synaptic variable | |
| | **GABAergic neuron** | |
| $v_i$ | Membrane potential | mV |
| $h_i$ | Sodium inactivating gating variable | |
| $n_i$ | Potassium activating gating variable | |
| $[K^+]_i$ | Intracellular potassium concentration | mM |
| $[Na^+]_i$ | Intracellular sodium concentration | mM |
| $s_i$ | Synaptic variable | |
| | **Extracellular concentrations** | |
| $[K^+]_o$ | Extracellular potassium concentration | mM |
| $[Na^+]_o$ | Extracellular sodium concentration | mM |
| $[Cl^-]_o$ | Extracellular chloride concentration | mM |

only part of the ion currents of the pyramidal neuron had an effect on its reversal potentials, in addition to the delayed-rectifier potassium current of the GABAergic neuron. Here, we took into account the effect of each transmembrane current on the intracellular ion concentration of the corresponding neuron and on the extracellular concentration. As a consequence, System (3.1) has first integrals linking the membrane potential of a neuron and its intracellular ion concentrations, as we show in Section 3.2.2.1.

3. In [35], the dynamics of the voltage-gated channels of the GABAergic neuron was described using the Wang-Buzsáki model of hippocampal interneurons [82]. We replaced it with a model of fast-spiking cortical interneurons by Golomb et al. [40], which is presented in Section 3.2.2.5. Indeed, CSD that causes migraine aura is generated in the neocortex and experimental results suggest the FHM3 CSD is selectively initiated in the neocortex (Chapter 2).

4. We included the activity of the $Na^+/K^+$ ATPase for both neurons, not only for the pyramidal one as in [35]. We replaced the expression describing its dependence on the intracellular sodium and extracellular potassium concentrations with a more realistic one developed by Kager et al. [83], which is based on experimental data.

**Table 3.2: Model parameters.**

| Symbol | Description | Value | Unit | Source |
|---|---|---|---|---|
| $C$ | Membrane capacitance per area unit | 1 | $\mu F \cdot cm^{-2}$ | [35] |
| $\beta_2$ | Ratio GABAergic over pyramidal neuron volume | $\frac{2}{3}$ | | - |
| $Vol_e$ | Pyramidal neuron volume | $1.4368 \cdot 10^{-9}$ | $cm^3$ | [35] |
| $T$ | Temperature | 309.15 | K | [35] |
| $\rho_{pump,-70}$ | Pump maximal rate at $-70$ mV | 30 | $\mu A \cdot cm^{-2}$ | - |
| $K_{pump,Na}$ | Pump half activation intracellular $[Na^+]$ | 7.7 | mM | [75] |
| $K_{pump,K}$ | Pump half activation extracellular $[K^+]$ | 2 | mM | [75] |
| $a$ | Parameter for the pump voltage dependence | 0.39 | | [76] |
| $b$ | Parameter for the pump voltage dependence | 1.28 | | [76] |
| $\varepsilon$ | Extracellular $K^+$ diffusion rate | $5 \cdot 10^{-4}$ | $ms^{-1}$ | - |
| $K_{bath}$ | $K^+$ bath concentration | 3.5 | mM | [35, 74] |
| | **Pyramidal neuron** | | | |
| $\tau_e$ | Time constant for the decay of $s_e$ | 3 | ms | [35, 77] |
| $v_{thres,e}$ | Voltage threshold defining firing time | 0 | mV | [35, 78] |
| $g_{Na,FI,e}$ | Fast inactivating $Na^+$ maximal conductance | 100 | $mS \cdot cm^{-2}$ | [35, 79] |
| $g_{K,DR,e}$ | Delayed rectifier $K^+$ maximal conductance | 80 | $mS \cdot cm^{-2}$ | [35, 79] |
| $g_{K,AHP,e}$ | $Ca^{2+}$-activated $K^+$ maximal conductance | 1 | $mS \cdot cm^{-2}$ | - |
| $K_{Ca}$ | $Ca^{2+}$-activated $K^+$ half activation $[Ca^{2+}]_e$ | 0.001 | mM | [35, 80] |
| $g_{Na,L,e}$ | $Na^+$ leak conductance | 0.015 | $mS \cdot cm^{-2}$ | - |
| $g_{K,L,e}$ | $K^+$ leak conductance | 0.05 | $mS \cdot cm^{-2}$ | [35] |
| $g_{Cl,L,e}$ | $Cl^-$ leak conductance | 0.015 | $mS \cdot cm^{-2}$ | [35] |
| $\rho_{KCC}$ | KCC2 cotransporter strength | 0.0003 | $mM \cdot ms^{-1}$ | [35, 74] |
| $\rho_{NKCC}$ | NKCC1 cotransporter strength | 0.0001 | $mM \cdot ms^{-1}$ | [35, 74] |
| $K_{NKCC,K}$ | NKCC1 cotransporter half activation $[K^+]_o$ | 16 | mM | [35, 74] |
| $g_{GLU,e}$ | Glutamatergic current maximal conductance | 0.1 | $mS \cdot cm^{-2}$ | [35] |
| $g_{GABA,e}$ | GABAergic current maximal conductance | 2.5 | $mS \cdot cm^{-2}$ | - |
| $g_{D,e}$ | External glutamatergic conductance | 0-0.3 | $mS \cdot cm^{-2}$ | - |
| $g_{Ca,e}$ | $Ca^{2+}$ maximal conductance | 1 | $mS \cdot cm^{-2}$ | [35, 80] |
| $E_{Ca,e}$ | $Ca^{2+}$ reversal potential | 120 | mV | [35, 80] |
| $\tau_{Ca}$ | Time constant for $Ca^{2+}$ extrusion and buffering | 80 | ms | [35, 81] |
| | **GABAergic neuron** | | | |
| $\tau_i$ | Time constant for the decay of $s_i$ | 9 | ms | [35] |
| $v_{thres,i}$ | Voltage threshold defining firing time | 0 | mV | [35, 78] |
| $g_{Na,FI,i}$ | Fast inactivating $Na^+$ maximal conductance | 112.5 | $mS \cdot cm^{-2}$ | [40] |
| $g_{K,DR,i}$ | Delayed rectifier $K^+$ maximal conductance | 225 | $mS \cdot cm^{-2}$ | [40] |
| $g_{Na,L,i}$ | $Na^+$ leak conductance | 0.012 | $mS \cdot cm^{-2}$ | - |
| $g_{K,L,i}$ | $K^+$ leak conductance | 0.05 | $mS \cdot cm^{-2}$ | - |
| $g_{GLU,i}$ | Glutamatergic current maximal conductance | 0.1 | $mS \cdot cm^{-2}$ | [35] |
| $g_{D,i}$ | External glutamatergic conductance | 0-0.3 | $mS \cdot cm^{-2}$ | - |

#### 3.2.2.1 Conserved quantities

We identified several first integrals in System (3.1), namely conservation of mass for sodium and chloride, and a relationship between the membrane potential of a neuron and its intracellular concentrations. In this section, we will explain their role and effect on the system's dynamics. First of all, we introduce the conversion factors $\gamma_e$, $\gamma_i$, $\beta_1$ and $\beta_2$.

**Conversion factors** Let $z$ be the valence of an ion. Then, $\frac{\gamma_e}{z}$ converts the current of this ion across the membrane of the pyramidal neuron in $\mu A \cdot cm^{-2}$ to variation of concentration inside the cell in $mM \cdot ms^{-1}$. The conversion factor $\gamma_e$ is defined as

$$\gamma_e = \frac{S_e}{10^3 \text{Vol}_e N_A e},$$

where $\text{Vol}_e$ and $S_e$ are the volume and surface area of the pyramidal neuron, $e = 1.6 \cdot 10^{-19}\,C$ the elementary charge and $N_A = 6.02 * 10^{23}\,mol^{-1}$ the Avogadro number. We take $\text{Vol}_e = 1.4368 * 10^{-9}\,cm^3$ [35] and we compute $S_e$ assuming the neuron is spherical:

$$S_e = 4\pi \left(\frac{3\text{Vol}_e}{4\pi}\right)^{\frac{2}{3}}.$$

We obtain

$$\gamma_e = 4.45 * 10^{-5}\,mol \cdot cm^2 \cdot \mu C^{-1} \cdot L^{-1}.$$

The conversion factor $\gamma_i$ plays the same role as $\gamma_e$ but for the GABAergic neuron. We assume that the GABAergic neuron is a sphere of volume $\text{Vol}_i = \beta_2 \text{Vol}_e$, with $\beta_2 = \frac{2}{3}$, which gives

$$\gamma_i = 5.09 * 10^{-5}\,mol \cdot cm^2 \cdot \mu C^{-1} \cdot L^{-1}.$$

To convert variation of intracellular concentration to variation of extracellular concentration, we need to multiply by the intracellular volume of the corresponding neuron and to divide by the extracellular volume $\text{Vol}_o$. Let $\beta_1$ be the ratio of total intracellular volume over extracellular volume: $\beta_1 = \frac{\text{Vol}_e + \text{Vol}_i}{\text{Vol}_o} = 4$ [84]. We then have

$$\frac{\text{Vol}_e}{\text{Vol}_o} = \frac{\beta_1}{1+\beta_2},$$
$$\frac{\text{Vol}_i}{\text{Vol}_o} = \frac{\beta_1 \beta_2}{1+\beta_2}.$$

**Conservation of mass** In System (3.1), the sodium and chloride concentrations are only modified by transmembrane currents. We have thus conservation of mass for those ions. Note that it is not the case for potassium, for which we take into account extracellular diffusion (see Section 3.3.1.4). The conserved quantities enable us to reduce the number of unknowns. For sodium,

$$\frac{d}{dt}\left([Na^+]_o \text{Vol}_o + [Na^+]_e \text{Vol}_e + [Na^+]_i \text{Vol}_i\right) = 0.$$

Let

$$Na_\sum = [Na^+]_o + \frac{\text{Vol}_e}{\text{Vol}_o}[Na^+]_e + \frac{\text{Vol}_i}{\text{Vol}_o}[Na^+]_i.$$

We fix

$$Na_\sum = 145 + \beta_1 10 = 185\,mM.$$

We can then express the extracellular sodium concentration as a function of the intracellular concentrations:

$$[\mathrm{Na}^+]_\mathrm{o} = \mathrm{Na}_\sum - \frac{\mathrm{Vol}_\mathrm{e}}{\mathrm{Vol}_\mathrm{o}}[\mathrm{Na}^+]_\mathrm{e} - \frac{\mathrm{Vol}_\mathrm{i}}{\mathrm{Vol}_\mathrm{o}}[\mathrm{Na}^+]_\mathrm{i}.$$

Similarly, for chloride we define

$$\mathrm{Cl}_\sum = [\mathrm{Cl}^-]_\mathrm{o} + \frac{\mathrm{Vol}_\mathrm{e}}{\mathrm{Vol}_\mathrm{o}}[\mathrm{Cl}^-]_\mathrm{e}$$

and choose

$$\mathrm{Cl}_\sum = 130 + \frac{\beta_1}{1+\beta_2}5 = 142\,\mathrm{mM}.$$

**Relation between membrane potential and intracellular ion concentrations** System (3.1) has two other first integrals, which arise from the fact that we take into account the effect of all ionic currents on the dynamics of the intracellular concentrations and that no other mechanism affects those concentrations. For the pyramidal neuron, we have

$$C\frac{\mathrm{d}v_\mathrm{e}}{\mathrm{d}t} - \frac{1}{\gamma_\mathrm{e}}\left(\frac{\mathrm{d}[\mathrm{Na}^+]_\mathrm{e}}{\mathrm{d}t} + \frac{\mathrm{d}[\mathrm{K}^+]_\mathrm{e}}{\mathrm{d}t} - \frac{\mathrm{d}[\mathrm{Cl}^-]_\mathrm{e}}{\mathrm{d}t}\right) = 0. \tag{3.2}$$

This allows us to remove an additional unknown. Let

$$H_1 = Cv_\mathrm{e} - \frac{1}{\gamma_\mathrm{e}}\left([\mathrm{Na}^+]_\mathrm{e} + [\mathrm{K}^+]_\mathrm{e} - [\mathrm{Cl}^-]_\mathrm{e}\right).$$

We fix

$$H_1 = -70 - \frac{1}{\gamma_\mathrm{e}}\left(10 + 140 - 5\right) \approx -3,258,497\,\mu\mathrm{A}\cdot\mathrm{cm}^{-2}.$$

We can then express the potassium concentration in the pyramidal neuron as

$$[\mathrm{K}^+]_\mathrm{e} = \gamma_\mathrm{e}\left(v_\mathrm{e} - H_1\right) - [\mathrm{Na}^+]_\mathrm{e} + [\mathrm{Cl}^-]_\mathrm{e}.$$

We proceed similarly for the GABAergic neuron: let

$$H_2 = Cv_\mathrm{i} - \frac{1}{\gamma_\mathrm{i}}\left([\mathrm{Na}^+]_\mathrm{i} + [\mathrm{K}^+]_\mathrm{i}\right),$$

with

$$H_2 = -70 - \frac{1}{\gamma_\mathrm{i}}\left(10 + 140\right) \approx -2,947,024\,\mu\mathrm{A}\cdot\mathrm{cm}^{-2}.$$

The potassium concentration in the GABAergic neuron is given by:

$$[\mathrm{K}^+]_\mathrm{i} = \gamma_\mathrm{i}\left(v_\mathrm{i} - H_2\right) - [\mathrm{Na}^+]_\mathrm{i}.$$

Note that, in such a configuration, we should not model external inputs to the neurons with a constant current appearing only in the equation for the membrane potential. For

example, if we add a constant external current $J$ to the right hand side of Eq. (3.1a):

$$C\,\frac{\mathrm{d}v_\mathrm{e}}{\mathrm{d}t} = -I_\mathrm{Na,e} - I_\mathrm{K,e} - I_\mathrm{Cl,e} + J,$$

Section 3.2.2.1 becomes

$$C\frac{\mathrm{d}v_\mathrm{e}}{\mathrm{d}t} - \frac{1}{\gamma_\mathrm{e}}\left(\frac{\mathrm{d}[\mathrm{Na}^+]_\mathrm{e}}{\mathrm{d}t} + \frac{\mathrm{d}[\mathrm{K}^+]_\mathrm{e}}{\mathrm{d}t} - \frac{\mathrm{d}[\mathrm{Cl}^-]_\mathrm{e}}{\mathrm{d}t}\right) = J.$$

Integrating, we see that it causes a drift of the system:

$$Cv_\mathrm{e} - \frac{1}{\gamma_\mathrm{e}}\left([\mathrm{Na}^+]_\mathrm{e} + [\mathrm{K}^+]_\mathrm{e} - [\mathrm{Cl}^-]_\mathrm{e}\right) = \text{constant} + Jt,$$

which thus cannot have any steady state nor limit cycle. Instead, we modeled external inputs to the neurons using synaptic currents. We assumed a constant glutamate input on AMPA receptors, which generates sodium and potassium currents. Those currents appear both in the equation for the membrane potential and in the ones for the intracellular ion concentrations, preserving the first integrals $H_1$ and $H_2$. They are defined in Section 3.2.2.2.

#### 3.2.2.2 Transmembrane ion currents

The reversal potentials, which are used to compute ion currents, are typically assumed to be constant. Here, they vary with the ion concentrations, and their dependence on the corresponding ion gradient is given by the Nerst equation:

$$E_\mathrm{ion} = \frac{RT}{z_\mathrm{ion}F}\log\left(\frac{[\mathrm{ion}]_\mathrm{extracellular}}{[\mathrm{ion}]_\mathrm{intracellular}}\right),$$

where $R = 8,314\,\mathrm{mJ}\cdot(\mathrm{K}\cdot\mathrm{mol})^{-1}$ is the ideal gas constant, $T$ the temperature, $F = N_\mathrm{A}e$ the Faraday constant and $z_\mathrm{ion}$ the valence.

**Pyramidal neuron** For the pyramidal neuron, the currents generated by the sodium and potassium voltage-gated channels were modeled as in [35]:

- Fast inactivating sodium current: $I_\mathrm{Na,FI,e} = g_\mathrm{Na,FI,e}\, m_\mathrm{e}^3\, h_\mathrm{e}\, (v_\mathrm{e} - E_\mathrm{Na,e})$,
- Delayed rectifier potassium current: $I_\mathrm{K,DR,e} = g_\mathrm{K,DR,e}\, n_\mathrm{e}^4\, (v_\mathrm{e} - E_\mathrm{K,e})$.

As [35], we took into account a calcium-activated potassium current, which is involved in the afterhyperpolarization (AHP) phase of action potentials. It is defined as

$$I_\mathrm{K,AHP,e} = g_\mathrm{K,AHP,e}\,\frac{[\mathrm{Ca}^{2+}]_\mathrm{e}}{[\mathrm{Ca}^{2+}]_\mathrm{e} + \mathrm{K}_\mathrm{Ca}}\,(v_\mathrm{e} - E_\mathrm{K,e}).$$

The implementation of cotransporters was also directly taken from [35]. Those proteins perform secondary active transport: they use the favorable movement of molecules with their electrochemical gradient as an energy source to move other molecules against their gradient. The potassium-chloride transporter member 5 (KCC2) extrudes potassium and chloride (Fig. 3.1), using the potassium gradient to maintain low intracellular chloride concentration:

$$I_\mathrm{KCC} = \frac{\rho_\mathrm{KCC}}{\gamma_\mathrm{e}}\,\log\left(\frac{[\mathrm{K}^+]_\mathrm{e}[\mathrm{Cl}^-]_\mathrm{e}}{[\mathrm{K}^+]_\mathrm{o}[\mathrm{Cl}^-]_\mathrm{o}}\right).$$

The Na-K-Cl cotransporter isoform NKCC1 transports sodium, potassium and chloride into the cell, with the stoichiometry 1Na:1K:2Cl (Fig. 3.1):

$$I_{\mathrm{NKCC}} = \frac{1}{\gamma_{\mathrm{e}}} \frac{\rho_{\mathrm{NKCC}}}{1+\exp(K_{\mathrm{NKCC,K}}-[\mathrm{K}^+]_{\mathrm{o}})} \left(\log\left(\frac{[\mathrm{K}^+]_{\mathrm{e}}[\mathrm{Cl}^-]_{\mathrm{e}}}{[\mathrm{K}^+]_{\mathrm{o}}[\mathrm{Cl}^-]_{\mathrm{o}}}\right) + \log\left(\frac{[\mathrm{Na}^+]_{\mathrm{e}}[\mathrm{Cl}^-]_{\mathrm{e}}}{[\mathrm{Na}^+]_{\mathrm{o}}[\mathrm{Cl}^-]_{\mathrm{o}}}\right)\right).$$

Contrary to [35], we distinguished the sodium, potassium and chloride components of the leak current:

- Leak sodium current: $I_{\mathrm{Na,L,e}} = g_{\mathrm{Na,L,e}}\,(v_{\mathrm{e}} - E_{\mathrm{Na,e}})$,
- Leak potassium current: $I_{\mathrm{K,L,e}} = g_{\mathrm{K,L,e}}\,(v_{\mathrm{e}} - E_{\mathrm{K,e}})$,
- Leak chloride current: $I_{\mathrm{Cl,L,e}} = g_{\mathrm{Cl,L,e}}\,(v_{\mathrm{e}} - E_{\mathrm{Cl,e}})$.

This allowed us to measure their effect on the different ion concentrations. Similarly, we separated the sodium and potassium currents due to the excitatory autapse, assuming an equal permeability of the glutamatergic receptors to both ions:

- $I_{\mathrm{Na,GLU,e}} = \frac{g_{\mathrm{GLU,e}}}{2} s_{\mathrm{e}}\,(v_{\mathrm{e}} - E_{\mathrm{Na,e}})$,
- $I_{\mathrm{K,GLU,e}} = \frac{g_{\mathrm{GLU,e}}}{2} s_{\mathrm{e}}\,(v_{\mathrm{e}} - E_{\mathrm{K,e}})$.

As explained in Section 3.2.2.1, external inputs to the pyramidal neurons were modeled with a constant glutamate input on those receptors:

- $I_{\mathrm{Na,D,e}} = \frac{g_{\mathrm{D,e}}}{2}(v_{\mathrm{e}} - E_{\mathrm{Na,e}})$,
- $I_{\mathrm{K,D,e}} = \frac{g_{\mathrm{D,e}}}{2}(v_{\mathrm{e}} - E_{\mathrm{K,e}})$.

Those currents represent average excitatory network activity or experimental depolarizations. The inhibitory synaptic current, created by the movement of chloride ions through $\mathrm{GABA_A}$ receptors, was modeled as in [35]:

$$I_{\mathrm{GABA,e}} = g_{\mathrm{GABA,e}}\; s_{\mathrm{i}}\; (v_{\mathrm{e}} - E_{\mathrm{Cl,e}}).$$

To model the activity of the $\mathrm{Na}^+/\mathrm{K}^+$ ATPase, we used this expression [83, 85]:

$$I_{\mathrm{pump,e}} = \rho_{\mathrm{pump}}(v_{\mathrm{e}}) \left(\frac{[\mathrm{Na}^+]_{\mathrm{e}}}{[\mathrm{Na}^+]_{\mathrm{e}} + \mathrm{K}_{\mathrm{pump,Na}}}\right)^3 \left(\frac{[\mathrm{K}^+]_{\mathrm{o}}}{[\mathrm{K}^+]_{\mathrm{o}} + K_{\mathrm{pump,K}}}\right)^2,$$

with half-activation parameters from [75]. Based on Bouret et al. [76], we also introduced a voltage dependence of the pump maximal rate:

$$\rho_{\mathrm{pump}}(v) = \rho_{\mathrm{pump},-70} \frac{f(v)}{f(-70)},$$

where

$$f(v) = \frac{1 + \tanh\left(a\frac{F}{RT}v + b\right)}{2}.$$

To summarize, the net currents for each ion are:

$$\begin{aligned}
I_{\mathrm{Na,e}} &= I_{\mathrm{Na,FI,e}} + I_{\mathrm{Na,L,e}} + 3I_{\mathrm{pump,e}} + I_{\mathrm{NKCC}} + I_{\mathrm{Na,GLU,e}} + I_{\mathrm{Na,D,e}},\\
I_{\mathrm{K,e}} &= I_{\mathrm{K,DR,e}} + I_{\mathrm{K,AHP,e}} + I_{\mathrm{K,L,e}} + I_{\mathrm{KCC}} + I_{\mathrm{NKCC}} - 2I_{\mathrm{pump,e}} + I_{\mathrm{K,GLU,e}} + I_{\mathrm{K,D,e}},\\
I_{\mathrm{Cl,e}} &= I_{\mathrm{Cl,L,e}} - I_{\mathrm{KCC}} - 2I_{\mathrm{NKCC}} + I_{\mathrm{GABA,e}}.
\end{aligned}$$

**GABAergic neuron** The sodium and potassium currents through the voltage-gated channels of the GABAergic neurons were modeled as in [40]:

- Fast inactivating $Na^+$ current: $I_{Na,FI,i} = g_{Na,FI,i}\, m_{\infty,i}^3\, h_i(v_i - E_{Na,i})$,
- Delayed rectifier $K^+$ current: $I_{K,DR,i} = g_{K,DR,i}\, n_i^2(v_i - E_{K,i})$.

For more details on the gating dynamics of those channels, see Section 3.2.2.5.

In the same way as for the pyramidal neuron, we separated the components pertaining to the different ions for the leak currents:

- Leak $Na^+$ current: $I_{Na,L,i} = g_{Na,L,i}\,(v_i - E_{Na,i})$,
- Leak $K^+$ current: $I_{K,L,i} = g_{K,L,i}\,(v_i - E_{K,i})$,

for the glutamatergic synaptic currents:

- $I_{Na,GLU,i} = \frac{g_{GLU,i}}{2} s_e\,(v_i - E_{Na,i})$,
- $I_{K,GLU,i} = \frac{g_{GLU,i}}{2} s_e\,(v_i - E_{K,i})$,

and for the glutamatergic synaptic currents which model an average external input to the GABAergic neuron:

- $I_{Na,D,i} = \frac{g_{D,i}}{2}(v_i - E_{Na,i})$,
- $I_{K,D,i} = \frac{g_{D,i}}{2}(v_i - E_{K,i})$.

The $Na^+/K^+$ ATPase current is given by the same sigmoidal function as for the pyramidal neuron:

$$I_{pump,i} = \rho_{pump}(v_i)\left(\frac{[Na^+]_i}{[Na^+]_i + K_{pump,Na}}\right)^3\left(\frac{[K^+]_o}{[K^+]_o + K_{pump,K}}\right)^2.$$

We obtained the following sodium and potassium net currents:

$$I_{Na,i} = I_{Na,FI,i} + I_{Na,P,i} + I_{Na,L,i} + 3I_{pump,i} + I_{Na,GLU,i} + I_{Na,D,i},$$
$$I_{K,i} = I_{K,DR,i} + I_{K,L,i} - 2I_{pump,i} + I_{K,GLU,i} + I_{K,D,i}.$$

### 3.2.2.3 Calcium concentration in the pyramidal neuron

The conductance of the calcium-activated potassium current $I_{K,AHP,e}$ is determined by the pyramidal neuron's intracellular calcium concentration. As in [35], we modeled the dynamics of this concentration with Eq. (3.1h) from Wang [81]:

$$\frac{d[Ca^{2+}]_e}{dt} = -\frac{\gamma_e}{2} I_{Ca,e} - \frac{[Ca^{2+}]_e}{\tau_{Ca}}.$$

$I_{Ca,e}$ represents high threshold calcium current and is given by:

$$I_{Ca,e} = g_{Ca,e}\, m_{\infty,Ca}\,(v_e - E_{Ca,e}).$$

It is a transmembrane current, but for simplicity we did not take into account its effect on the pyramidal neuron's membrane potential. Unlike in [35], we used the same conversion factor $\gamma_e$ as for the other ions, for consistency. The second term models various extrusion and buffering mechanism, with a first order decay process.

#### 3.2.2.4 Diffusion of extracellular potassium

As in [35], the following term appears in the equation for the extracellular potassium 3.1p:

$$I_{\mathrm{K,diff}} = \varepsilon \left( [\mathrm{K}^+]_\mathrm{o} - \mathrm{K}_\mathrm{bath} \right).$$

It accounts for passive diffusion of extracellular potassium, but also, in a simplistic way, for the buffering of this ion by glial cells. This motivated the use of a large value of the diffusion coefficient $\epsilon$ (see Table 3.2), which is a conservative choice.

#### 3.2.2.5 Gating variables dynamics

Gating variables represent the state of activation of voltage-gated channels. In Sections 3.2.2.2 and 3.2.2.3, they scale the maximal conductance of those channels.

**Pyramidal neuron** For the pyramidal neuron, the dynamics of the potassium and sodium gating variables is given by Eqs. (3.1b) to (3.1d). As in [35], we used a simplified version of the Traub-Miles model [86] due to Wei et al. [74]:

$$\begin{aligned}
\alpha_{m,\mathrm{e}} &= 0.32 \frac{v_\mathrm{e} + 54}{1 - \exp(-\frac{v_\mathrm{e}+54}{4})}, \\
\beta_{m,\mathrm{e}} &= 0.28 \frac{v_\mathrm{e} + 27}{\exp(\frac{v_\mathrm{e}+27}{5}) - 1}, \\
\alpha_{h,\mathrm{e}} &= 0.128 \exp(-\frac{v_\mathrm{e} + 50}{18}), \\
\beta_{h,\mathrm{e}} &= \frac{4}{1 + \exp(-\frac{v_\mathrm{e}+27}{5})}, \\
\alpha_{n,\mathrm{e}} &= 0.032 \frac{v_\mathrm{e} + 52}{1 - \exp(-\frac{v_\mathrm{e}+52}{5})}, \\
\beta_{n,\mathrm{e}} &= 0.5 \exp(-\frac{v_\mathrm{e} + 57}{40}).
\end{aligned}$$

Eq. (3.1h) describes the dynamics of the intracellular calcium concentration, needed to compute the conductance of the calcium-activated potassium channels. As in [35], we assumed that the state of the calcium channels depends instantaneously on the voltage, according to this expression by Wang [81] with parameter values from Gutkin et al. [80]:

$$m_{\infty,\mathrm{Ca}} = \frac{1}{1 + \exp\left(-\frac{v_\mathrm{e}+25}{2.5}\right)}.$$

**GABAergic neuron** For the GABAergic neuron, we replaced the Wang-Buzsáki model [82] with a more recent one by Golomb et al. [40], which is specific to fast-spiking cortical

interneurons:

$$
\begin{aligned}
m_{\infty,\mathrm{i}} &= \frac{1}{1+\exp(-\frac{v_\mathrm{i}-(-24)}{11.5})}, \\
h_{\infty,\mathrm{i}} &= \frac{1}{1+\exp(-\frac{v_\mathrm{i}-(-58.3)}{6.7})}, \\
\tau_{h,\mathrm{i}} &= 0.5 + \frac{14}{1+\exp(-\frac{v_\mathrm{i}-(-60)}{-12})}, \\
n_{\infty,\mathrm{i}} &= \frac{1}{1+\exp(-\frac{v_\mathrm{i}-(-12.4)}{6.8})}, \\
\tau_{n,\mathrm{i}} &= \left(0.087 + \frac{11.4}{1+\exp(\frac{v_\mathrm{i}+14.6}{8.6})}\right)\left(0.087 + \frac{11.4}{1+\exp(-\frac{v_\mathrm{i}-1.3}{18.7})}\right).
\end{aligned}
$$

The sodium activating variable is assumed to be at its steady state value $m_{\infty,\mathrm{i}}$. The dynamics of the sodium inactivating variable $h_\mathrm{i}$ and of the potassium activating variable $n_\mathrm{i}$ is given in Eqs. (3.1k) to (3.1l).

#### 3.2.2.6 Mutations of $Na_V1.1$

$Na_V1.1$ is mainly expressed in GABAergic neurons and $Na_V1.1$ mutations affect mainly these neurons [1]. Thus, we assumed in our simulations that the pyramidal neuron is unaffected by mutations of this channel. As we shall see, to model FHM3 or epilepsy we only modified two parameters: the maximal conductance $g_{\mathrm{Na,FI,i}}$ of the fast-inactivating sodium current and the maximal conductance $g_{\mathrm{Na,P,i}}$ of the persistent sodium current, which we introduce in the case of migraine.

**FHM3 mutations** Increased persistent sodium current is a common effect of most $Na_V1.1$ FHM3 mutations [5–8]. To model them, we partially replaced the GABAergic neuron's fast inactivating sodium current $I_{\mathrm{Na,FI,i}}$ with a persistent sodium current $I_{\mathrm{Na,P,i}}$. We kept the sum of their maximal conductances constant: $g_{\mathrm{Na,FI,i}} + g_{\mathrm{Na,P,i}} = 112.5\,\mathrm{mS}\cdot\mathrm{cm}^{-2}$. We modeled persistent current with the following expression:

$$I_{\mathrm{Na,P,i}} = g_{\mathrm{Na,P,i}} m_{\infty,\mathrm{i}}^3 (v_\mathrm{i} + v_{\mathrm{shift,P}})(v_\mathrm{i} - E_{\mathrm{Na,i}}).$$

Note that it does not include the inactivation mechanism represented by the variable $h_\mathrm{i}$ for the fast inactivating current. We also shifted the voltage dependence of its activation to more negative potentials [87, 88] ($v_{\mathrm{shift,P}} = 8\,\mathrm{mV}$). Let $p_{\mathrm{Na,P}}$ be the percentage of maximal voltage-gated sodium conductance corresponding to persistent current:

$$p_{\mathrm{Na,P}} = \frac{g_{\mathrm{Na,P,i}}}{g_{\mathrm{Na,FI,i}} + g_{\mathrm{Na,P,i}}} \cdot 100.$$

To model $Na_V1.1$ FHM3 mutations, we tested values up to $p_{\mathrm{Na,P}} = 20\,\%$; see Section 3.3.1.

**Epileptogenic mutations** Epileptogenic mutations of $Na_V1.1$ cause a loss of function of the channel [1, 22]. To model them, we decreased the maximal conductance of the GABAergic neuron's fast inactivating sodium current $g_{\mathrm{Na,FI,i}}$. Based on what was experimentally observed in *Scn1a*$^{+/-}$ mice [22], we set it to 40 % of its default value, reflecting the condition of heterozygosis and the expression of other voltage-gated sodium channels

than $Na_V1.1$ in GABAergic neurons:

$$g_{Na,FI,i} = 0.4 \cdot 112.5 = 45\,mS \cdot cm^{-2}.$$

#### 3.2.2.7 Evolution of the model since the version in Chapter 2

In Chapter 2, we modeled only the mutations of $Na_V1.1$ which cause migraine (FHM3). Here, we extended the model to also study $Na_V1.1$ epileptogenic mutations. To capture both migraine and epilepsy scenario within the same framework, we had to adapt some parameter values (see Table 3.3):

- To favor the route towards epilepsy-like activity, rather than CSD initiation, we increased the inhibition of the pyramidal neuron by the GABAergic neuron (parameter $g_{GABA,e}$) and the diffusion of extracellular potassium (parameter $\varepsilon$).
- In Chapter 2, there was no external input to the pyramidal neuron to model the selective activation of GABAergic neurons by optogenetics. Here we stimulate both neurons ($g_{D,e} = g_{D,i}$).

For simplicity, we removed persistent sodium current for pyramidal neuron (parameter $g_{Na,P,e}$), since we are primarily interested in this current for the GABAergic neuron.

Compared to Chapter 2, we reduced the shift of persistent sodium current activation $v_{shift,P}$. We will see in Section 3.3.1 that, even though with this value of $v_{shift,P}$ persistent current does increase the firing frequency of the GABAergic neuron (Fig. 3.2 A), CSD initiation is nevertheless facilitated (Figs. 3.4 to 3.6).

**Table 3.3: Parameter values in Chapter 3 *vs.* Chapter 2.**

| Symbol | Description | Chapter 2 | Chapter 3 | Unit |
|---|---|---|---|---|
| $\varepsilon$ | Extracellular $K^+$ diffusion rate | $4 \cdot 10^{-5}$ | $5 \cdot 10^{-4}$ | $ms^{-1}$ |
| | **Pyramidal neuron** | | | |
| $g_{GABA,e}$ | GABAergic current max. conductance | 0.1 | 2.5 | $mS \cdot cm^{-2}$ |
| $g_{Na,P,e}$ | Persistent $Na^+$ max. conductance | 1 | 0 | $mS \cdot cm^{-2}$ |
| $g_{D,e}$ | External glutamatergic conductance | 0 | 0-0.3 | $mS \cdot cm^{-2}$ |
| | **GABAergic neuron** | | | |
| $v_{shift,P}$ | Persistent $Na^+$ current activation shift | 10 | 8 | mV |

### 3.2.3 Mouse lines, preparation of brain slices and electrophysiological recordings

Whole-cell patch clamp recordings were performed with the F1 generation of crosses between heterozygous *Scn1a*$^{+/-}$ knock-out mice (C57BL/6J-CD1 85:15 %) [22, 68] and C57BL/6J GAD67-GFPΔneo knock-in mice (which label GABAergic neurons with GFP [62]), comparing P15-18 double heterozygous (*Scn1a*$^{+/-}$_GAD67-GFPΔneo) and GAD67-GFPΔneo littermates. Optogenetic experiments for CSD induction and juxtacellular recordings were performed with P25-30 hemizygous transgenic VGAT-hChR2(H134R)/dtomato mice (VGAT-ChR2 in the text) in the C57BL/6J background, in which channelrhodopsin-H134R/tdtomato is specifically expressed in GABAergic neurons. They were the F1 generation obtained by crossing hemizygous females loxP-STOP-loxP-hChR2(H134R)-tdtomato (Ai27D, B6.Cg-Gt(ROSA)26Sortm27.1(CAG-COP4*H134R/tdTomato)Hze/

J; Jackson lab, JAX, n°012567) [63] with hemizygous Viaat-Cre transgenic males, in which selective Cre recombinase expression in GABAergic neurons is driven by the vesicular GABA transporter (VGAT) promoter (B6.FVB-Tg(Slc32a1-Cre)2.1Hzo/FrkJ; JAX n°017535), line 2.1 in [9]). Offspring was genotyped by PCR, following the standard JAX protocols for VGAT-ChR2 mice and using our standard protocol for *Scn1a*$^{+/-}$ mice [25, 68], or selecting fluorescent pups monitored with a Dual Fluorescent Protein flashlight (NightSea).

Brain slices of the somatosensory cortex were prepared as previously described [24, 25, 37, 68]. Briefly, mice were killed by decapitation under isofluorane anesthesia, the brain was quickly removed and placed in ice-cold artificial cerebrospinal fluid (ACSF), which contained (mM): NaCl 129, $MgSO_4$ 1.8, KCl 3, $CaCl_2$ 1.6, $NaHCO_3$ 21, $NaH_2PO_4$ 1.25 and glucose 10 bubbled with 95 % $O_2$ 5 % $CO_2$. Coronal slices (380 µm thick) were prepared with a vibratome (Microm HM650V or Leica VT1200S) in ice-cold ACSF, placed in a holding chamber at room temperature in ACSF continuously bubbled with 95 % $O_2$ 5 % $CO_2$, and used after one hour of recovery period. One slice at the time was placed in the recordings chamber (Warner Instruments, USA) and neurons were visualized by epifluorescence and infrared video microscopy with a Nikon Eclipse FN1 equipped with epifluorescence DIC optics and a CCD camera. Spatial optogenetic stimulation for activating ChR2 and inducing neuronal firing in a specific area was obtained illuminating brain slices through a 4x objective with 473 nm blue light generated using a white light source (130W Intensilight, Nikon) connected with a light guide containing a 420 nm UV blocker filter (series 2000, Lumatec, Germany) to a digital micromirror device (DMD)-based patterned photostimulator (Polygon 400, Mightex), whose output was filtered with a 475/50 filter (Semrock) and the light delivered to the objective with a FF685-Di02 dichroic beamsplitter (Semrock) (see Chapter 2).

Patch-clamp recordings were performed with a Multiclamp 700B amplifier, Digidata 1440a digitizer and pClamp 10.2 software (Axon Instruments, USA); signals were filtered at 10 kHz and acquired at 50 kHz. Whole-cell recordings of neuronal firing were done at 28 °C in current-clamp mode applying the bridge balance compensation; the external recording solution was ACSF (see above) and the internal solution contained (mM): K-gluconate, 120; KCl, 15; $MgCl_2$, 2; EGTA, 0.2; Hepes, 10; $Na_2ATP$, 2; $Na_2GTP$ 0.2; leupeptine, 0.1; P-creatine 20, pH 7.25 with KOH. Patch pipettes were pulled from borosilicate glass capillaries; they had resistance of 2.5-3.0 MΩ and access resistance of 5-10 MΩ . We held the resting potential at −70 mV by injecting the appropriate holding current, and neuronal firing was induced injecting depolarizing current pulses of increasing amplitude. Neurons with unstable resting potential and/or unstable firing were discarded from the analysis. Juxtacellular-loose patch recordings of neuronal firing were performed in voltage-clamp mode perfusing slices with modified mACSF at 34 °C (which contained (in mM): 125 NaCl, 3.5 KCl, 1 $CaCl_2$, 0.5 $MgCl_2$, 1.25 $NaH_2PO_4$, 25 $NaHCO_3$ and 25 glucose, bubbled with 95 % $O_2$ - 5 % $CO_2$) and using the same pipettes used for whole cell experiments, but filled with ACSF. Recordings were performed from GABAergic neurons of Layer 2-3, identified by their fluorescence and morphology. Fast-spiking neurons were selected for the analysis of whole cell recordings, identified by their firing properties (short, $<$ 1 ms, action potentials with pronounced after-hyperpolarization, non-adapting discharges reaching several hundred Hz of maximal firing frequency).

For the statistical analysis, the reported $n$ is the number of cells recorded; each experiment was performed using at least 3 animals. Statistical tests were performed with Origin (Origin Lab. Corp, USA), using the two-tailed non parametric Mann-Whitney U test. Differences were considered significant at $p < 0.05$.

The original raw data is available at https://doi.org/10.5281/zenodo.4926119.

## 3.3 Results

### 3.3.1 $Na_V1.1$ FHM3 mutations can lead to CSD initiation via extracellular potassium build-up also when neuronal input-output features are not modified

#### 3.3.1.1 Persistent sodium current ($I_{Na,P,i}$) in GABAergic neurons amplifies spiking-induced modifications of extracellular ion concentrations, even without modifications of their firing frequency

We first focused on $Na_V1.1$ FHM3 mutations, modeled by the increase of $I_{Na,P,i}$ for the GABAergic neuron which is a common effect of most of those mutations [5–8], and on their effect on the features of the GABAergic neuron itself. To investigate the latter point, we obtained simulations with a version of the model in which the influence of the pyramidal neuron on the GABAergic neuron, through synaptic connections or through variations of extracellular ion concentrations, was removed.

To study how $I_{Na,P,i}$ modifies the excitability of the GABAergic neuron, we computed the following input-output relationships: number of action potentials elicited during the application of a depolarizing external current of fixed duration versus the conductance of this current (Fig. 3.2 A). We found that an increase of $I_{Na,P,i}$ reduces the rheobase (i.e. minimal external input necessary to trigger at least one action potential): $0.0004\,\mathrm{mS \cdot cm^{-2}}$ when $p_{Na,P} = 20\,\%$ (migraine condition) instead of $0.0051\,\mathrm{mS \cdot cm^{-2}}$ when $p_{Na,P} = 0\,\%$ (control condition), where $p_{Na,P}$ is defined in Section 3.2.2.6. This is consistent with a decrease of the rheobase observed experimentally in neocortical mouse neurons transfected with $hNa_V1.1$-L1649Q, a pathogenic mutant of the $Na_V1.1$ channel associated with FHM [6]. However, in contrast to [6], in our model FHM3 mutations do not substantially increase the GABAergic neuron's firing frequency. With external inputs $g_{D,i}$ up to approximately $0.1\,\mathrm{mS \cdot cm^{-2}}$, an increase of $p_{Na,P}$ consistently leads to a moderate increase of the number of action potentials generated, but this is not the case for stronger external inputs. Interestingly, there may be variability among GABAergic neurons, concerning how their firing frequency is affected by FHM3 mutations. In a novel FHM3 knock-in mouse model, Freilinger et al. [39] observed an increase of frequency in fast-spiking GABAergic neurons, but no significant difference in regular spiking interneurons, although they both express $Na_V1.1$.

On the other hand, persistent sodium current clearly enhances the accumulation of extracellular potassium (Fig. 3.2 B) and the uptake of extracellular sodium (Fig. 3.2 C) due to the firing of the GABAergic neuron, even when the number of action potentials is similar or slightly smaller than in the control condition. For example, for an external input of conductance $g_{D,i} = 0.3\,\mathrm{mS \cdot cm^{-2}}$ and $p_{Na,P} = 20\,\%$, with 48 spikes in 0.4 s we obtained an extracellular potassium concentration of 8.6 mM (145 % increase) and an extracellular sodium concentration of 147.5 mM (3.7 % decrease). However, when $p_{Na,P} = 0\,\%$, there were 49 spikes in 0.4 s but only 5.9 mM of extracellular potassium (68 % increase) and still 150.7 mM of extracellular sodium (1.7 % decrease) at the end of the simulation.

This is a counterintuitive result that we have better investigated comparing detailed features of action potentials and underlying ionic currents for those parameter values: $g_{D,i} = 0.3\,\mathrm{mS \cdot cm^{-2}}$ and $p_{Na,P} = 0\,\%$ or $20\,\%$ (Fig. 3.3). With increased $I_{Na,P,i}$, simulations showed larger action potential half width (0.365 ms for the $25^{th}$ action potential with $p_{Na,P} = 0\,\%$ and 0.565 ms with $p_{Na,P} = 20\,\%$, Fig. 3.3 $C_1$). However, modifications of action potential features were relatively small compared to the increase of $I_{Na,P,i}$. We reasoned that the $I_{Na,P,i}$ increase could induce a larger activation of potassium channels during the action potentials, able to limit the modifications of action potential features, but leading to larger potassium currents and consequent spiking-induced extracellular

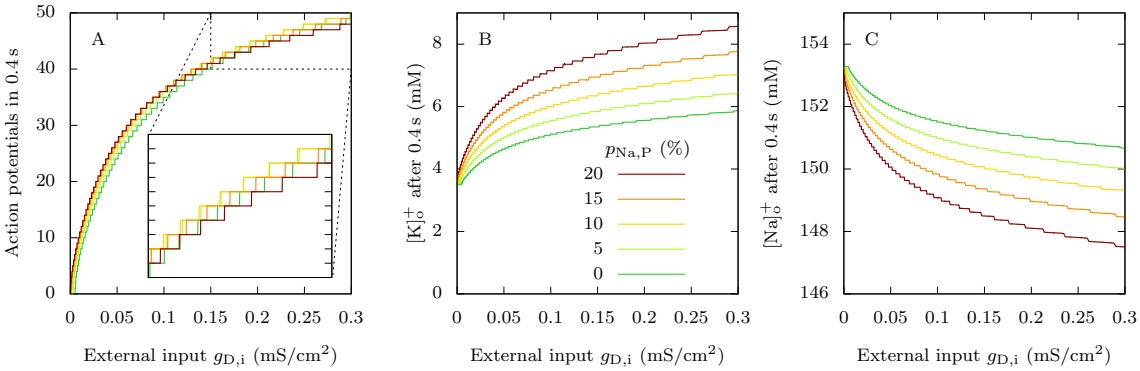


**Figure 3.2: Effect of FHM3 mutations on the firing properties of the GABAergic neuron.** For different values of $p_{Na,P}$ (defined in Section 3.2.2.6, which we increase to model FHM3 mutations, we applied to the GABAergic neuron 0.4 s long excitatory external inputs of conductances $g_{D,i}$. For each $p_{Na,P}$ value, we took as initial condition the steady state in the absence of external input, i.e. when $g_{D,i} = 0\,mS \cdot cm^{-2}$. **A.** Number of action potentials, considered as overshooting spikes (i.e. exceeding 0 mV of peak membrane potential). **B.** Extracellular potassium concentration at the end of the 0.4 s long simulations. **C.** Extracellular sodium concentration at the end of the 0.4 s long simulations.

potassium build-up. Indeed, the plots of the potassium action currents show a large increase when $I_{Na,P,i}$ is higher ($0.520\,\mu A \cdot cm^{-2}$ for the 25$^{th}$ action potential in the discharge with $p_{Na,P} = 0\,\%$, $1.311\,\mu A \cdot cm^{-2}$ with $p_{Na,P} = 20\,\%$, Fig. 3.3 $C_2$), leading to a larger accumulation of extracellular potassium at each action potential (Fig. 3.3 $A_3, B_3, C_3$). As expected, action sodium currents show a large increase as well, in particular during the repolarization phase ($0.478\,\mu A \cdot cm^{-2}$ for the 25$^{th}$ action potential in the discharge with $p_{Na,P} = 0\,\%$, $1.284\,\mu A \cdot cm^{-2}$ with $p_{Na,P} = 20\,\%$, Fig. 3.3 $C_4$), leading to a consequent larger decrease of extracellular sodium concentration at each action potential (Fig. 3.3 $A_5$, $B_5, C_5$).

#### 3.3.1.2 Dynamics of neuronal firing at CSD initiation

In this section, we show how FHM3 mutations in the GABAergic neuron influence the entry of the pyramidal neuron into depolarization block, which we consider as the initiation of a CSD, when the two neurons are coupled. We depolarized them with the same external inputs $g_{D,e} = g_{D,i} = 0.3\,mS \cdot cm^{-2}$, and we compared the control condition ($p_{Na,P} = 0\,\%$) with a pathological one ($p_{Na,P} = 15\,\%$).

In the first case, tonic spiking of the GABAergic neuron begins immediately while there is a latency of a few seconds before the pyramidal neuron also starts to generate repetitive action potentials (Fig. 3.4 A). Those initial subthreshold oscillations demonstrate the inhibitory nature of the GABAergic neuron in a physiological situation. As expected, the firing frequency is larger in the GABAergic neuron than in the pyramidal one (Fig. 3.5 A, B). With pathological persistent sodium current in the GABAergic neuron, the voltage traces are very different (Fig. 3.4 B). As in the control condition, there is a delay before sustained firing of the pyramidal neuron, but both the GABAergic interneuron and the pyramidal neuron show two phases of activity, and during the first phase extracellular potassium rises faster and to a larger extent than in control (Fig. 3.4 C). This is coherent with the results obtained on the GABAergic neuron alone in Section 3.3.1.1. Shortly after the pyramidal neuron begins to spike, we observe an increase of its firing frequency to towards an initial plateau, together with a steeper slope for the increase in extracellular potassium concentration. This is followed by a further increase of the pyramidal neuron's firing frequency. The second phase leads to the beginning of depolarization block for

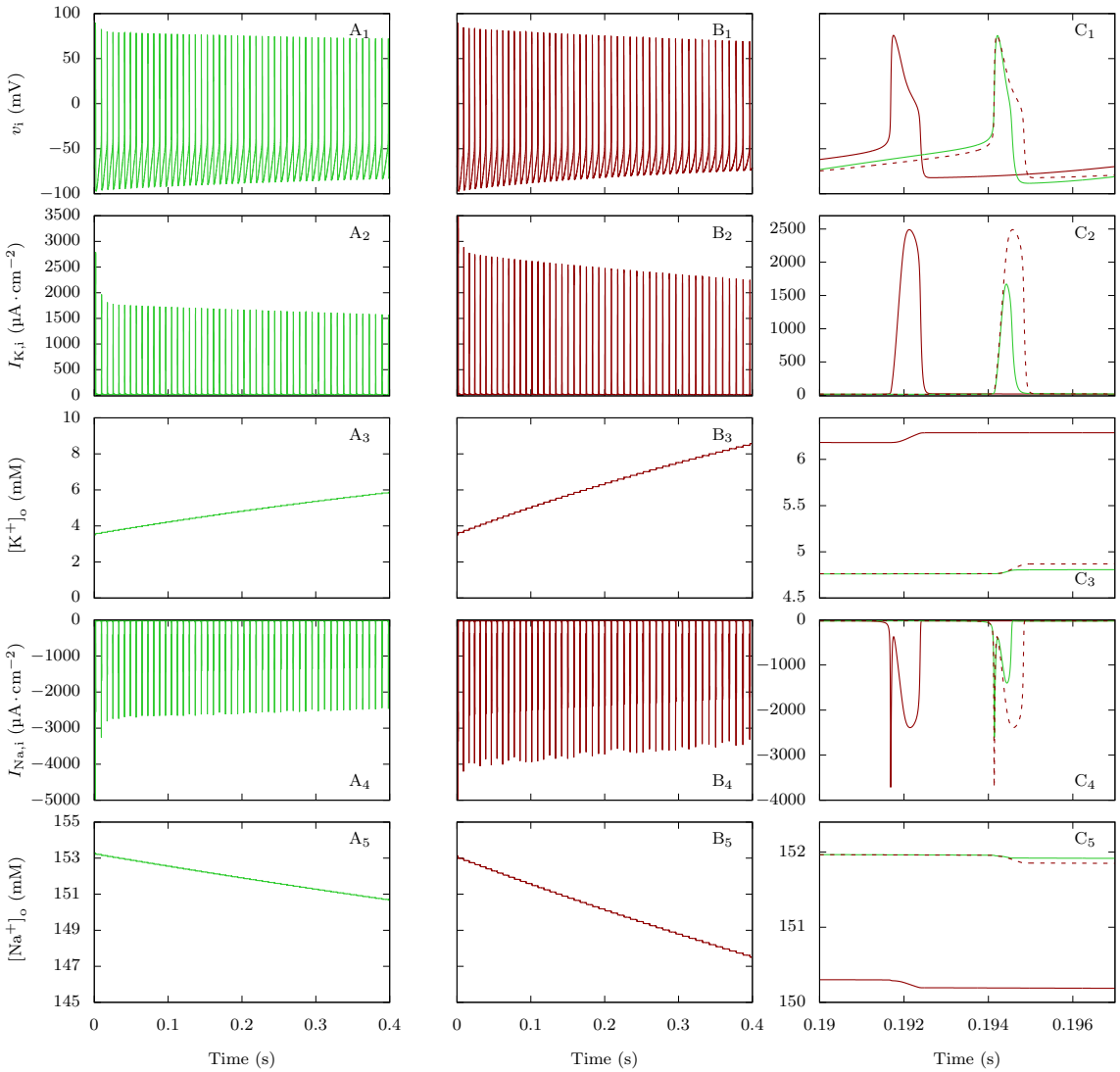


**Figure 3.3: Effect of FHM3 mutations on the firing and action currents of the GABAergic neuron, and correlation with the dynamics of $[K^+]_o$ and $[Na^+]_o$.** Plots of the voltage (action potentials; upper row), total potassium current (second row), extracellular potassium concentration (third row), total sodium current (fourth row) and extracellular sodium concentration (bottom row) corresponding to simulations displayed in Fig. 3.2, for the condition in which $g_{D,i} = 0.3\,mS \cdot cm^{-2}$. **A.** No persistent sodium current: $p_{Na,P} = 0\,\%$. **B.** $p_{Na,P} = 20\,\%$. **C.** Zoom showing the $25^{th}$ action potential of A (in green) and B (in red). The dashed lines are the curves obtained with $p_{Na,P} = 20\,\%$ shifted to allow a better comparison with the curves obtained with $p_{Na,P} = 0\,\%$.

both neurons, while extracellular potassium continues to grow. Notably, sodium overload during the depolarization block (Fig. 3.4 D) can contribute to silencing of firing.

In order to study experimentally the dynamics of the firing of both GABAergic interneurons and pyramidal neurons at the site of CSD initiation, we performed pairs of juxtacellular-loose patch voltage recordings, inducing CSD by spatial optogenetic activation of GABAergic neurons as in Chapter 2. Although this method of induction does not completely reproduce the condition of the simulation, it mimics hyperexcitability of the GABAergic neurons and allows recordings at the pre-determined site of CSD initiation, which cannot be performed with other experimental models of CSD. Notably, the firing dynamics was similar to that obtained with the simulation. We found that GABAergic

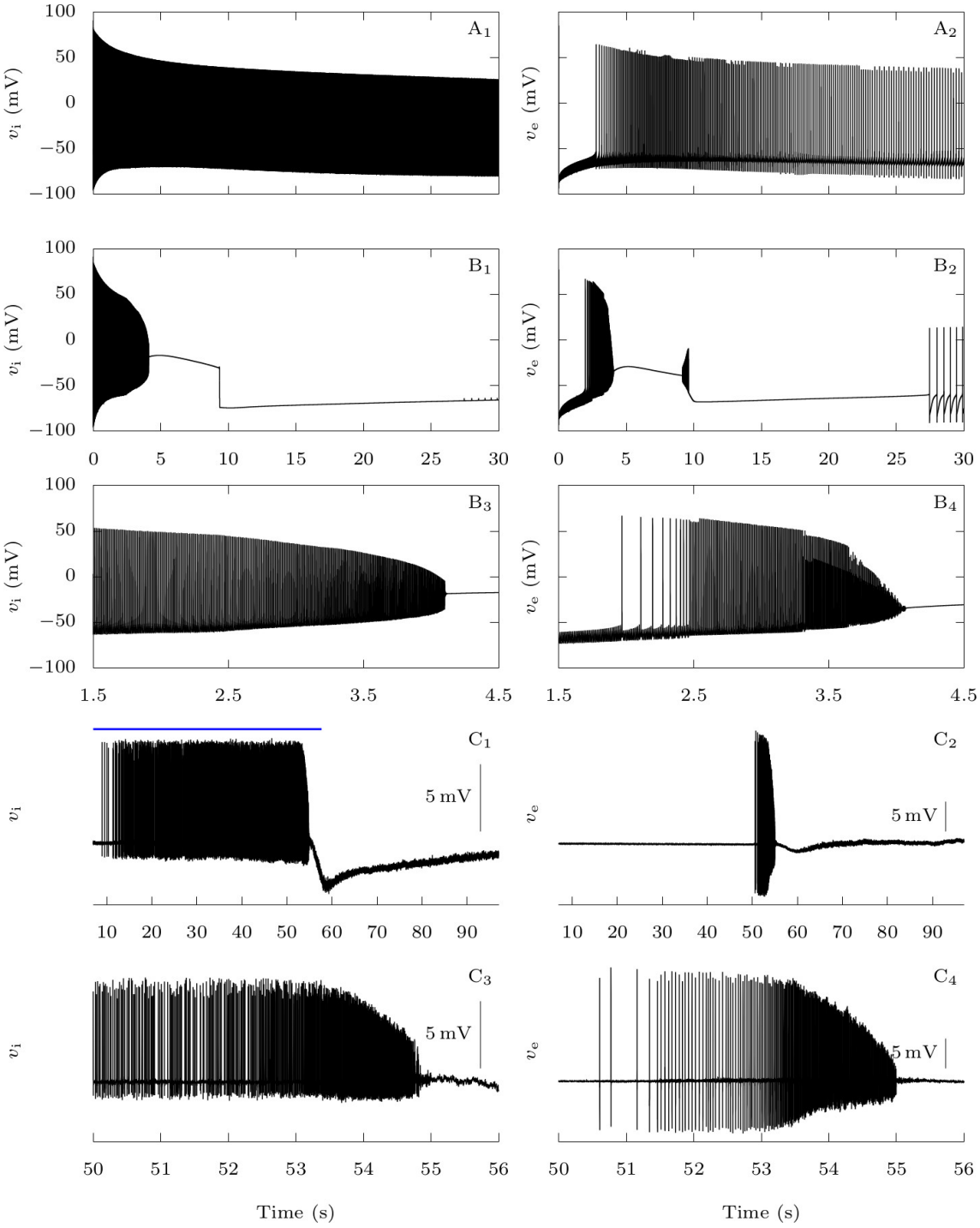


**Figure 3.4: Effect of the FHM3 mutation on CSD initiation: representative time traces. A-B**: Model simulations. Starting from neurons at rest, similarly to Fig. 3.2, we stimulated them with constant excitatory conductances $g_{D,i} = g_{D,e} = 0.3\,\mathrm{mS \cdot cm^{-2}}$ for 30 s. **A.** No persistent sodium current for the GABAergic neuron ($p_{Na,P} = 0\,\%$). **B.** Pathological condition ($p_{Na,P} = 15\,\%$). **C.** Experimental data. Representative dual juxtacellular-loose patch voltage recordings of a GABAergic interneuron (**$C_1$ and $C_3$**) and a pyramidal neuron (**$C_2$ and $C_4$**) showing the dynamics of the firing at the site of CSD initiation; CSD was induced by spatial optogenetic activation of GABAergic neurons and is the slow negative deflection observable in $C_1$ and $C_2$. The blue bar in $C_1$ shows the optogenetic stimulation with blue light.

neurons began to fire at the beginning of the illumination, whereas pyramidal neurons

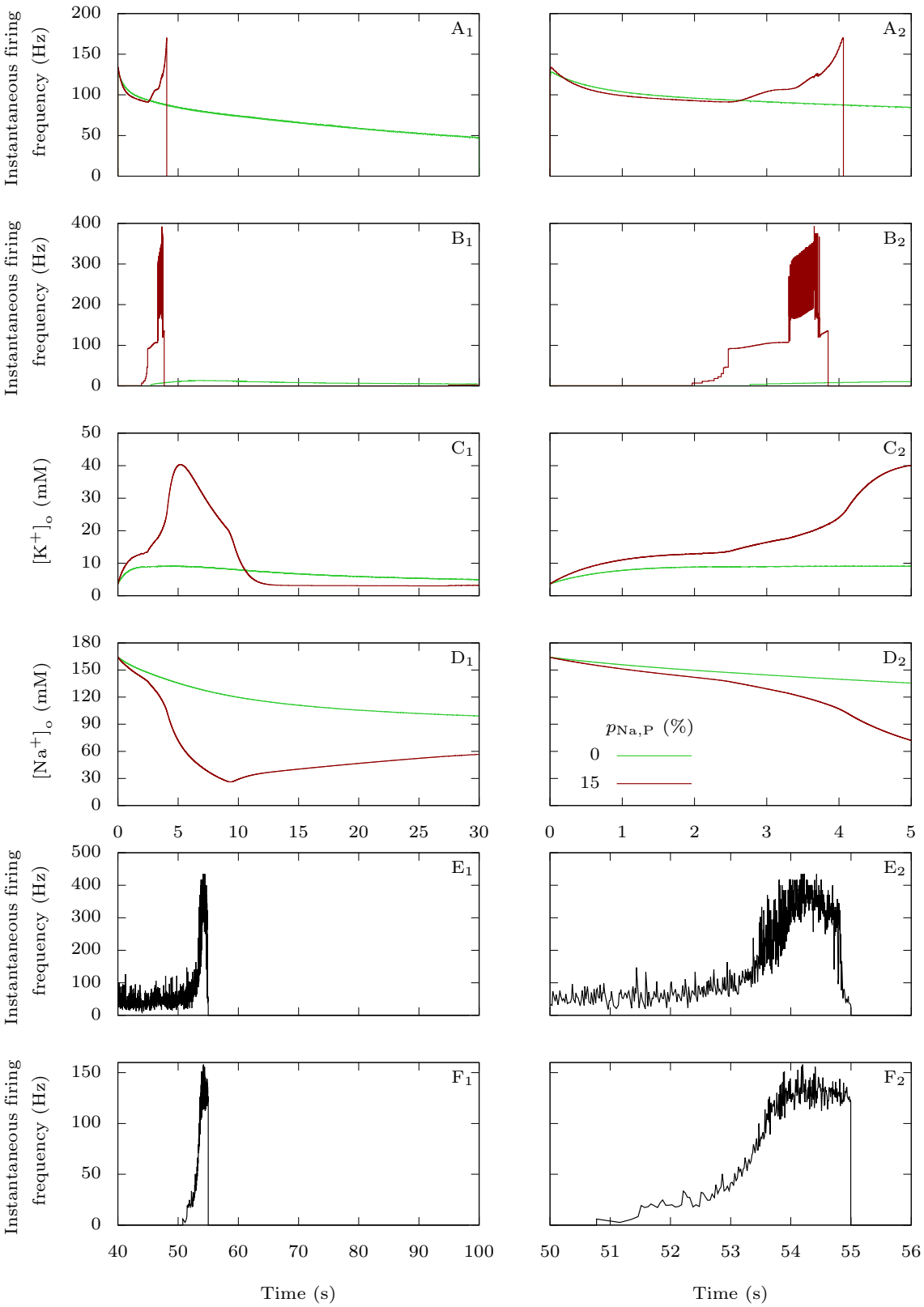


**Figure 3.5: Behavior of the firing frequency and of the extracellular ion concentrations before the onset of CSD. A - D.** Model simulations. For the first 5 s of the simulations presented in Fig. 3.4, we compared the pathological situation ($p_{\mathrm{Na,P}} = 15\,\%$) with the physiological one ($p_{\mathrm{Na,P}} = 0\,\%$). **A.** Instantaneous firing frequency, i.e. inverse of the *(continued next page)*

**Figure 3.5** ***(previous page)*****:** interspike interval, for the GABAergic neuron. **B.** Instantaneous firing frequency for the pyramidal neuron. **C.** Extracellular potassium concentration. **D.** Extracellular sodium concentration. **E - F.** Experimental data. **E.** Instantaneous firing frequency of the loose patch recording of the GABAergic neuron shown in Fig. 3.4 $C_1, C_3$. **F.** Instantaneous firing frequency of the loose patch recording of the pyramidal neuron shown in Fig. 3.4 $C_2, C_4$. CSD was induced by the optogenetic stimulation of the GABAergic neuron; the two phases in the firing dynamics, with lower and higher frequency respectively, are evident and similar to those observed in the simulation. Although the first phase was longer for GABAergic neurons ($55.3 \pm 4.5$ s, $n = 7$) than for pyramidal neurons ($1.6 \pm 0.2$ s, $n = 5$; $p = 0.006$ Mann-Whitney test), the second phase had similar duration ($2.0 \pm 0.2$ s for GABAergic neurons; $1.7 \pm 0.3$ s for pyramidal neurons; $p = 0.28$, Mann-Whitney test) and firing frequency was not significantly different (mean instantaneous firing frequency in the first phase was $48.4 \pm 6.8$ Hz for GABAergic neurons and $32.4 \pm 8.5$ Hz for pyramidal neurons, $p = 0.19$ Mann-Whitney test; in the second phase it was $349 \pm 36$ Hz for GABAergic neurons and $214 \pm 57$ Hz for pyramidal neurons, $p = 0.06$ Mann-Whitney test).

began to fire later during the illumination, just for few seconds before CSD initiation (Figs. 3.4 C and 3.5 E, F). As in the simulation, the firing dynamics of both GABAergic and pyramidal neurons showed two phases, a first phase with lower firing frequency (which was on average 34.6-fold longer for the GABAergic neurons) and a second phase of similar duration (few seconds) for the two types of neurons, in which firing frequency increased on average 8.3±1.8-fold for GABAergic neurons and 8.1±2.5-fold for pyramidal neurons, leading to depolarization block. Although few GABAergic neurons fired at very high frequency, instantaneous frequency was on average not different between GABAergic and pyramidal neurons.

#### 3.3.1.3 Persistent sodium current in GABAergic neurons reduces the threshold for CSD initiation

More generally, we studied whether those findings are robust to modifications of the value of parameter $p_{\mathrm{Na,P}}$ in the pathological case. This is important since we do not know precisely which level of persistent sodium current best models the effects of FHM3 mutations. Migraine is an episodic disorder, which means that patients exhibit symptoms only during attacks: a trigger factor causes the shift from a physiological state to a pathological state [12]. In our model, FHM3 mutations reduce the threshold for this transition. Indeed, the more persistent sodium current in the GABAergic neuron, the smaller the minimal external input necessary to initiate CSD (Fig. 3.6 A). This is consistent with experimental results from Chapter 2 where it was shown that bath application of Hm1a, a toxin which mimics the effects of FHM3 mutations by increasing persistent sodium current, can lead to spontaneous CSD initiation in mouse brain slices. Moreover, we found that, for a given large external input, persistent sodium current decreases the latency to CSD (Fig. 3.6 B). Here also, our simulations agree qualitatively with experimental data. Indeed, optogenetic activation of GABAergic neurons induces CSD earlier in slices perfused with Hm1a than in control slices (Chapter 2). Those two points are also supported by experiments on the knock-in mouse model of the L1649Q FHM3 mutation: the threshold for eliciting CSD by electrical stimulation was substantially lowered in heterozygous mice, and the latency from KCL application to the onset of CSD was significantly reduced [39].

Very close to the threshold that is approximated in Fig. 3.6 A, the response oscillates between non-CSD and CSD solutions, when gradually increasing the external input. This shows great sensitivity of the model at the transition between physiological and pathological behaviors. We cannot assert whether this is a numerical effect or a property inherent to the model. In any case, such a phenomenon is not surprising given the dimensionality of the model and its multiple timescales. Similar issues already arise in much simpler

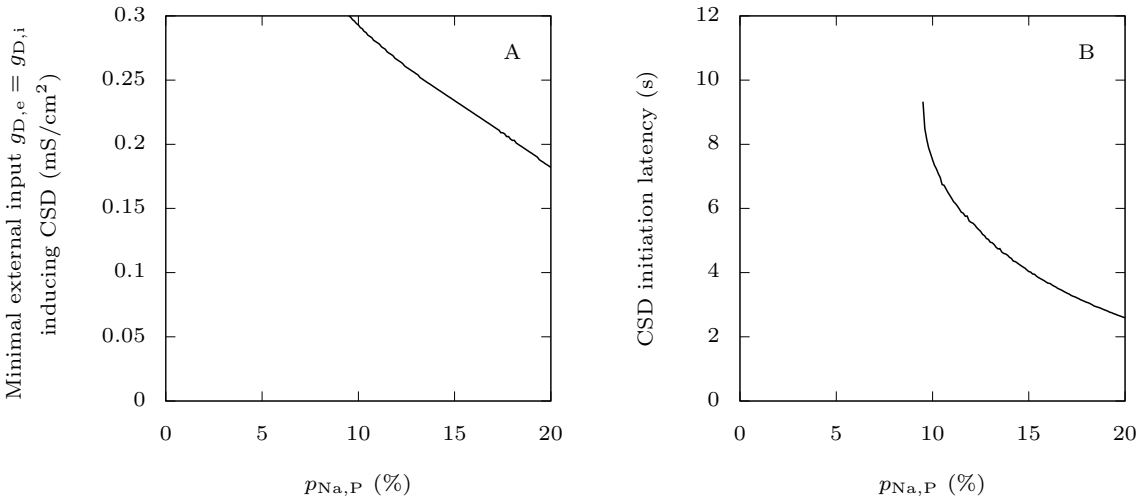


**Figure 3.6: Effect of FHM3 mutations on CSD initiation. A.** We show here how increasing the GABAergic neuron's persistent sodium current influences the minimal external input necessary to induce a depolarization block in the pyramidal neuron, varying $p_{Na,P}$ from 0 to 20 %. We used as external inputs constant excitatory conductances, equal for both neurons, taking values up to $g_{D,i} = g_{D,e} = 0.3\,\mathrm{mS \cdot cm^{-2}}$. We considered that beyond these values, inputs would be unrealistically strong, leading to a response of the model that would not be interpretable. Again, we chose as initial condition the steady state when the neurons are not stimulated. We defined a depolarization block by the absence of oscillations of amplitude larger than 5 mV of the voltage for at least half a second, with the additional condition that it must be between −55 mV and −20 mV at the end of this interval. For each $p_{Na,P}$, we estimated the smaller external input for which this criterion is met for the pyramidal neuron with a bisection method. **B.** Starting from neurons at rest, for given large external inputs $g_{D,e} = g_{D,i} = 0.3\,\mathrm{mS \cdot cm^{-2}}$, we computed the time it takes for a CSD to be initiated, if it is initiated at all.

conductance-based models, e.g. FitzHugh-Nagumo, Morris-Lecar or a 2D reduction of Hodgkin-Huxley, which are type-2 neuron models for which the firing threshold may not be well defined [89]. The approximation of the threshold for CSD initiation that we have obtained is nevertheless sufficient to study the roles of persistent sodium current and extracellular ion concentrations. Computing the exact threshold, if it exists, is challenging, and we do not consider it relevant for the purpose of the present study. This is an interesting question for future work, where we will focus on reducing our current model while keeping its most salient features.

#### 3.3.1.4 The accumulation of extracellular potassium is crucial for CSD initiation

In our model, the two neurons are coupled through synaptic connections and through variations in extracellular ion concentrations. The synaptic connection from the GABAergic neuron to the pyramidal one is inhibitory in all the tested conditions (see Section 3.3.3). Modifications of extracellular ion concentrations can thus be the cause of the large increase of firing frequency that precedes the depolarization block observed in the pathological case (Fig. 3.4 B). In the first seconds of the simulation, both extracellular potassium and sodium concentrations are substantially modified (Fig. 3.4 C, D, but the relative change is much more important for potassium, consistent with the simulations with the isolated GABAergic neuron (Fig. 3.2). A rise in extracellular potassium increases the reversal potential for this ion, which is a depolarizing effect, while a decay of the extracellular sodium has the opposite effect. This suggests that potassium plays a major role in promoting CSD initiation. To confirm it, we implemented unrealistically strong buffering of

either extracellular potassium or sodium, to keep their concentration constant (Fig. 3.7 A, B). In the same pathological setting as in Fig. 3.4 B, we applied strong external inputs $g_{D,i} = g_{D,e} = 0.3\,\mathrm{mS}\cdot\mathrm{cm}^{-2}$ to the neurons. We observe that only the strong buffering of extracellular potassium prevents CSD initiation (Fig. 3.7 B). More generally, similarly to (Fig. 3.6), we computed the thresholds for CSD initiation and the latencies to CSD for strong external inputs (Fig. 3.8 A). Remarkably, keeping the extracellular potassium concentration low completely prevents CSD initiation over the examined ranges of persistent current and external inputs. This is not the case with sodium; in fact the strong buffering of its extracellular concentration even facilitates CSD initiation, and leads to a larger increase of extracellular potassium concentration.

We also tested smaller values of the extracellular potassium diffusion rate. This can model, in a simplistic way, the contribution of other GABAergic neurons to the accumulation of extracellular potassium, or a less efficient buffering by the glial network. As expected, it reduces the threshold for CSD initiation and CSD is ignited earlier for a given stimulus (Fig. 3.8 B).

### 3.3.2 $Na_V1.1$ epileptogenic mutations strongly decrease the inhibitory role of GABAergic neurons

#### 3.3.2.1 Reduced sodium current in GABAergic neurons makes them more susceptible to depolarization block

As with the FHM3 mutations (Section 3.3.1.1), we first investigated the effects of epileptogenic mutations on the GABAergic neuron itself, when it does not interact with the pyramidal neuron. To model epileptogenic mutations of $Na_V1.1$, we reduced the GABAergic neuron's fast-inactivating sodium maximal conductance, as explained in Section 3.2.2.6.

The simulations show that in this condition the rheobase is slightly increased, action potential amplitude is decreased and depolarization block is induced by smaller depolarizing external inputs (Figs. 3.9 A, B and 3.10 A). Notably, action potential firing frequency shows just very small modifications in the input-output relationship (Fig. 3.10 $A_1$), in which a slight increase is surprisingly observed for the epileptic condition between $g_{D,i} = 0.2$ and $g_{D,i} = 0.4\,\mathrm{mS}\cdot\mathrm{cm}^{-2}$. We observed similar modifications in experimental traces, comparing cortical layer 2-3 fast spiking GABAergic neurons recorded in heterozygous *Scn1a* knock-out mice ($Scn1a^{+/-}$), model of the developmental and epileptic encephalopathy Dravet syndrome [1, 22], and wild type littermates as control (Figs. 3.9 C, D and 3.10 B). Notably, the comparison of single representative neurons with similar input-output relationships showed that, although firing frequency could be slightly larger for the $Scn1a^{+/-}$ neuron, depolarization block was induced by a smaller depolarizing current (Figs. 3.9 C, D and 3.10 $B_1$) and action potential amplitude was reduced (Fig. 3.10 $B_2$). The comparison of average features did not disclose modifications of firing frequency before the induction of depolarization block in $Scn1a^{+/-}$ (Fig. 3.10 $B_3$), but depolarization block was consistently induced with smaller depolarizing currents. Of note, for obtaining these average input-output curves, we excluded for each cell the traces in which there was depolarization block, to avoid the influence of depolarization block in the evaluation of firing frequency with larger depolarizing currents. To statistically compare action potential amplitude, we quantified the mean amplitude of the first suprathreshold action potential, which was reduced in $Scn1a^{+/-}$ mice (Fig. 3.10 $B_4$).

To better understand the enhanced transition from the firing regime to depolarization block of the GABAergic neuron when $Na_V1.1$ carries an epileptogenic loss of function mutation, which we observed in Fig. 3.10 $A_1$, we studied it as a *dynamic bifurcation* phenomenon [90]. Even though System (3.1) is not explicitly slow-fast, it is clear from its time traces that it has different timescales. We considered the sodium concentration in the

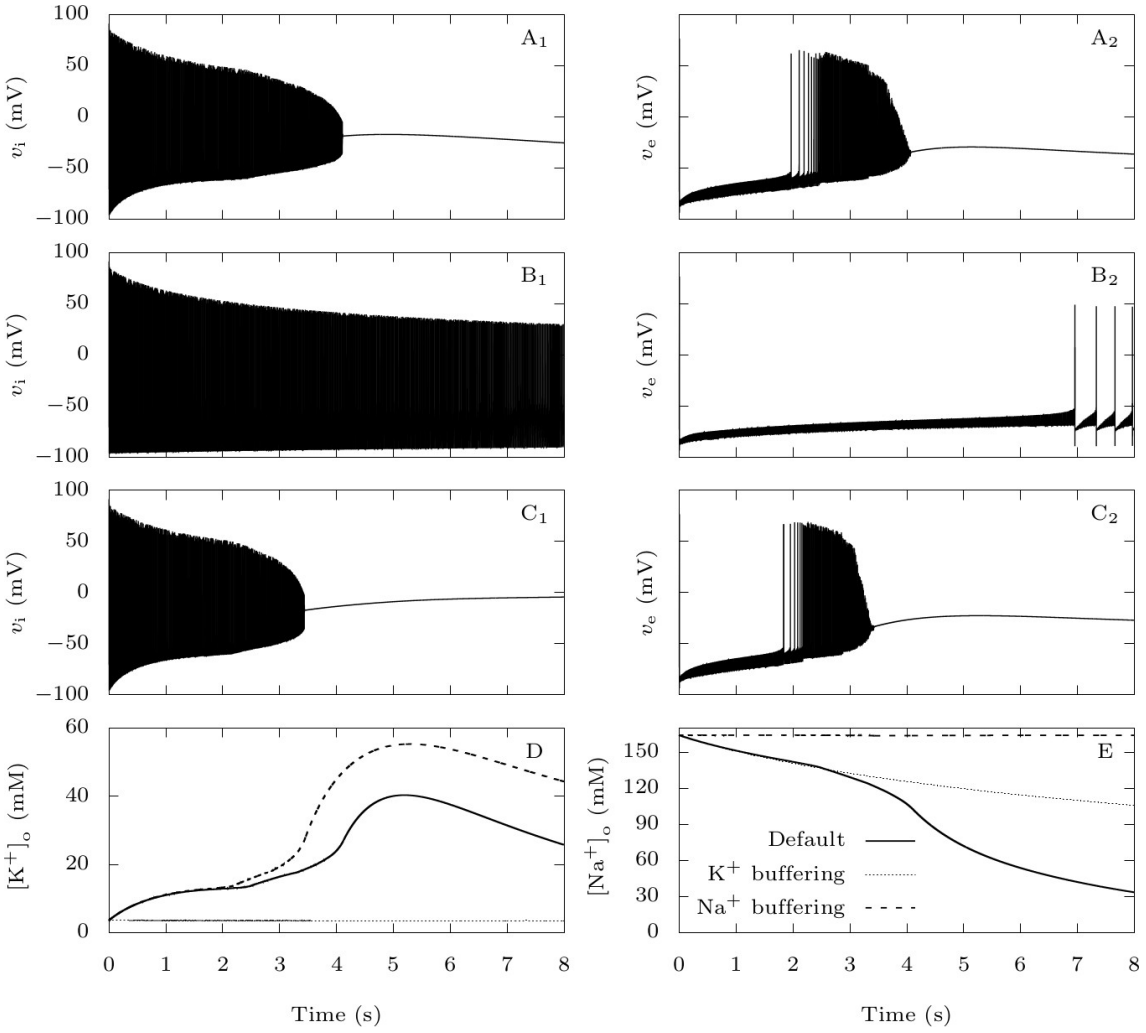


**Figure 3.7: The roles of extracellular ions in CSD initiation: representative time traces.** When $Na_V1.1$ carries a FHM3 mutation, modeled by $p_{Na,P} = 15\,\%$, we tested the effect of keeping either extracellular potassium or sodium constant using unrealistically high diffusion rates. We depolarized the neurons at rest with constant excitatory conductances $g_{D,i} = g_{D,e} = 0.3\,\mathrm{mS \cdot cm^{-2}}$ for 30 s. **A.** Voltage traces for the default parameters. **B.** Voltage traces when $\varepsilon = 0.1\,\mathrm{ms^{-1}}$ to simulate a strong buffering of extracellular potassium. **C.** Voltage traces when there is a strong buffering of extracellular sodium. To implement it, we introduced the diffusion term $I_{diff,Na} = \varepsilon_{Na}\left([Na^+]_o - Na_{bath}\right)$ in the equation for extracellular sodium, with $\varepsilon_{Na} = 0.1\,\mathrm{ms^{-1}}$ and $Na_{bath}$ equal to the steady-state extracellular sodium in the absence of external input. **D.** $[K^+]_o$ traces in the cases described in A-C. **E.** $[Na^+]_o$ traces in the cases described in A-C.

GABAergic neuron $[Na^+]_i$ as a slow variable, and analyzed the corresponding *fast subsystem* where $[Na^+]_i$ is a parameter, with or without epileptogenic mutation. In Fig. 3.11 A, we show the voltage traces of the complete system when applying an excitatory conductance $g_{D,i} = 0.3\,\mathrm{mS \cdot cm^{-2}}$ to the GABAergic neurons at rest. In Fig. 3.11 B, we projected the same solutions onto the $([Na^+]_i, v_i)$ plane, superimposed onto the bifurcation diagram of the fast subsystem with respect to $[Na^+]_i$, what is called a *slow-fast dissection* [91]. In the wild-type case, the solution first follows limit cycles of large amplitude, which corresponds to repetitive firing, while the sodium slowly increases (Fig. 3.11 $B_1$). For $[Na^+]_i$ approximately 28 mM there is a fold of limit cycle bifurcation, which causes the solution to jump to a stable steady state. This is the beginning of a quiescent phase, where the

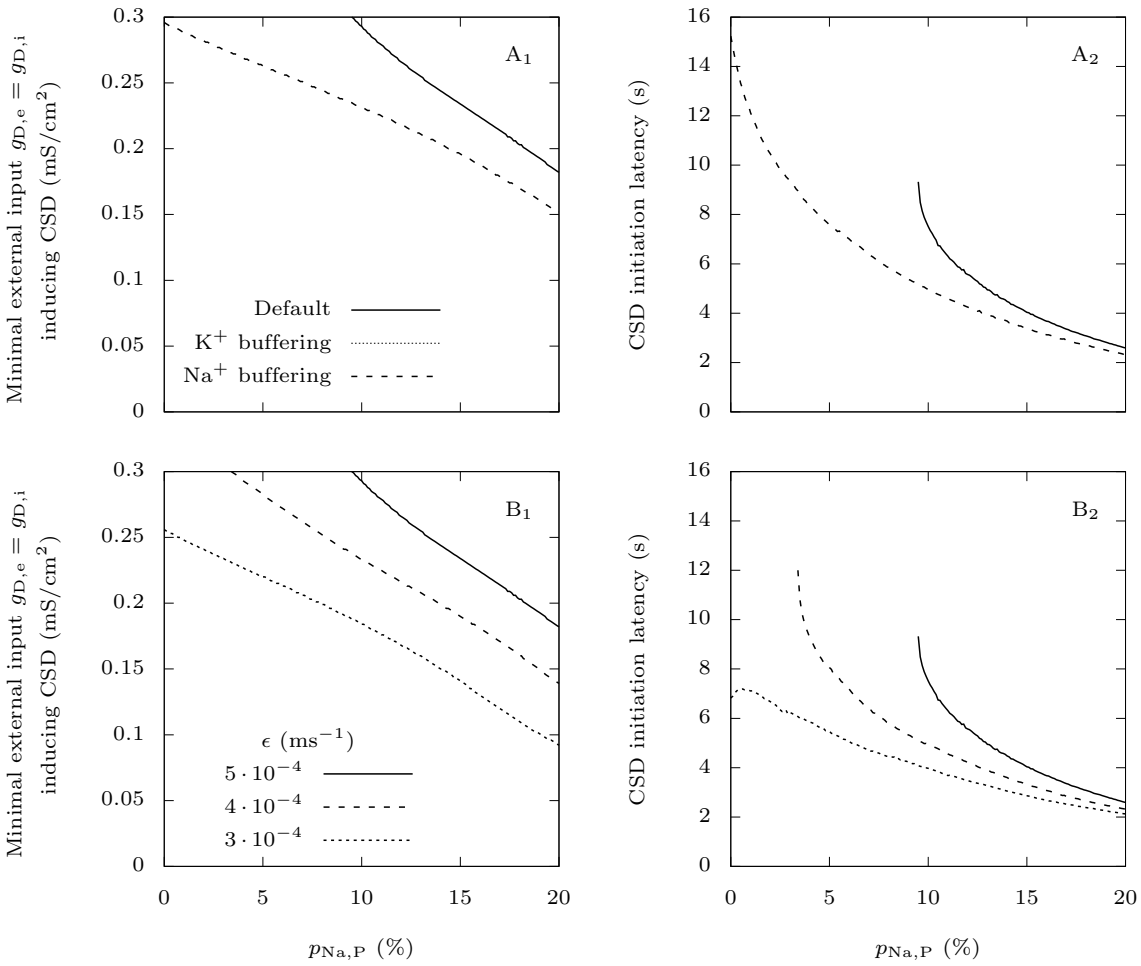


**Figure 3.8: The roles of extracellular ions in CSD initiation.** Similarly to Fig. 3.6, we show in the left panel the minimal external input necessary to induce a depolarization block in the pyramidal neuron, and in the right panel the latency to CSD. **A.** We tested the effect of keeping either extracellular potassium or sodium approximately constant using the same method as for Fig. 3.7. **B.** We tested the effect of reducing the extracellular potassium diffusion rate. The default value of this parameter is $\varepsilon = 5 \cdot 10^{-4}\,\mathrm{ms}^{-1}$.

neuron does not spike while $[Na^+]_i$ decreases slowly until a Hopf bifurcation is encountered, where the steady state becomes unstable. This causes the solution to return to the large-amplitude limit cycles. In this way, the solution alternates between active and quiescent phases (Fig. 3.11 $A_1$), a neuronal behavior typically referred to as *bursting*. It is not surprising since bursting is a possible behavior of the model we have used to describe the gating dynamics of the GABAergic neuron's voltage-gated channels [40]. The subHopf/fold-cycle hysteresis loop which enables this bursting is not preserved for the reduced value of fast-inactivating sodium maximal conductance which we use to model $Na_V1.1$'s epileptogenic mutations (Fig. 3.11 $B_2$). In this case, the solution of the complete system also first follows large-amplitude limit cycles while $[Na^+]_i$ slowly increases. However, once it reaches the fold of limit cycle bifurcation and jumps to the stable steady state, it does not leave it anymore: the GABAergic neuron completely stops producing action potentials (Fig. 3.11 $A_2$).

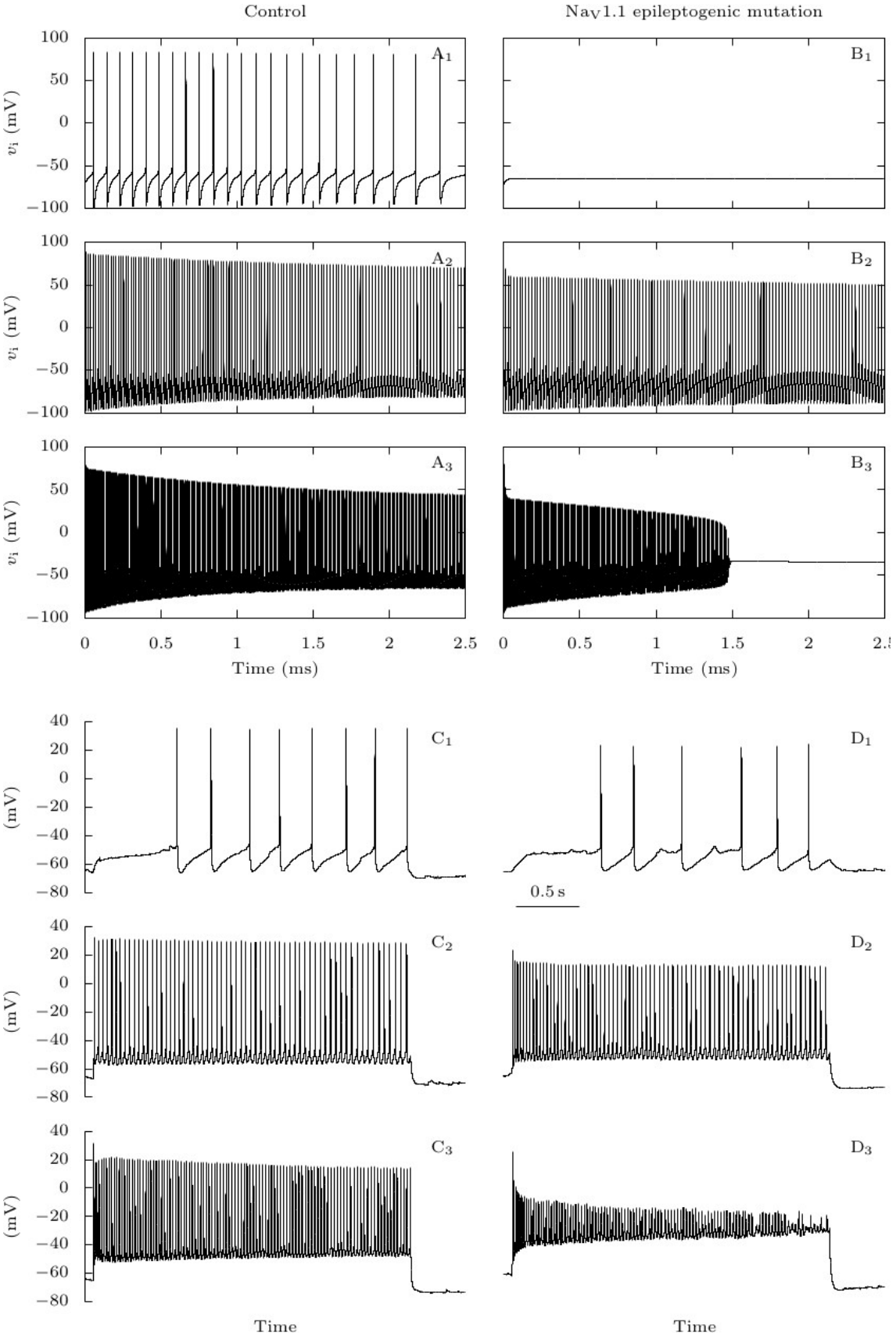


**Figure 3.9: Effect of Na$_V$1.1 epileptogenic mutations on the firing of GABAergic neurons: representative traces. A - B.** Model simulations. We *(continued next page)*

**Figure 3.9** ***(previous page)*****:** depolarized the GABAergic neuron at rest with constant excitatory conductances $g_{D,i} = 0.0075$ (**$A_1$**, **$B_1$**), $g_{D,i} = 0.05$ (**$A_2$**, **$B_2$**) or $g_{D,i} = 0.5\,mS \cdot cm^{-2}$ (**$A_3$**, **$B_3$**), for the default parameters (**A**: control condition), or when the sodium fast-inactivating maximal conductance is reduced to 40 % of its default value (**B**: $Na_V1.1$ epileptogenic mutation). **C - D.** Experimental data. Action potential discharges elicited in a fast spiking GABAergic layer 2-3 cortical neuron from a wild type mouse (**C**) or a *Scn1a*$^{+/-}$ mouse (**D**), injecting depolarizing current steps of 10 pA (**$C_1$**,**$D_1$**), 100 pA (**$C_2$**,**$D_2$**) or 260 pA (**$C_3$**,**$D_3$**).

#### 3.3.2.2 Pyramidal neurons firing frequency suddenly increases when GABAergic neurons enter depolarization block

We saw in the previous section that $Na_V1.1$'s epileptogenic loss of function mutations make GABAergic neurons more susceptible to depolarization block. We now focus on the consequences on the firing of the pyramidal neuron in our computational model, when the two neurons are coupled. We stimulated them with strong depolarizing external inputs ($g_{D,i} = g_{D,e} = 0.3\,mS \cdot cm^{-2}$), with or without $Na_V1.1$'s epileptogenic loss of function mutations mutation (Fig. 3.12). In the pathological condition, after firing for about ten seconds (Fig. 3.12 $B_1, C_1$), the GABAergic neuron enters depolarization block. Simultaneously, we observe a sharp increase of the firing frequency of the pyramidal neuron (Fig. 3.12 $B_2, C_2$). This behavior is easily understood: when the GABAergic neuron stops to generate action potentials, the synaptic inhibitory restraint that it exerts on the pyramidal neuron is suddenly removed, allowing the pyramidal neuron to fire at a greater pace. Although this effect cannot be considered epileptiform activity, it may model early hyperexcitability that has been observed in mouse models of Dravet syndrome before the appearance of spontaneous seizures [1, 68].

### 3.3.3 Comparison of migraine and epilepsy scenarios

Fig. 3.13 illustrates the differences, in our model, between the migraine and the epilepsy pathological scenarios. For the representative simulations displayed in Fig. 3.4 and in Fig. 3.12, we compared the evolution of the extracellular potassium concentration, of the inhibitory synaptic current received by the pyramidal neuron, and their effect on the pyramidal neuron's firing frequency. In the case of the migraine condition (Fig. 3.13 B), following an initial accumulation of extracellular potassium a few millimolars larger than in the wild-type condition (Fig. 3.13 A), the firing frequency of the pyramidal neuron rises significantly, causing the extracellular potassium to build-up even faster. This happens despite the inhibition from the GABAergic neuron, and it leads to a depolarization block of the pyramidal neuron shortly before four seconds. On the contrary, with the epileptogenic mutation (Fig. 3.13 C), the removal of the GABAergic neuron's inhibitory input on the pyramidal neuron after approximately 11.5 s is responsible for the increase of firing frequency of the pyramidal neuron. The simultaneous increase of extracellular potassium concentration is negligible. Notably, the GABAergic synaptic current never becomes depolarizing (Fig. 3.13 $A_2, B_2, C_2$).

## 3.4 Discussion

We have developed a two-neuron model with one pyramidal neuron and one GABAergic neuron, building upon our previous modeling framework [35]. It captures electrochemical activity leading to either CSD initiation or pro-epileptic hyperexcitability, caused by mutations of the sodium channel $Na_V1.1$. It is important to highlight again that our model has been developed to investigate these early events and not fully developed CSD

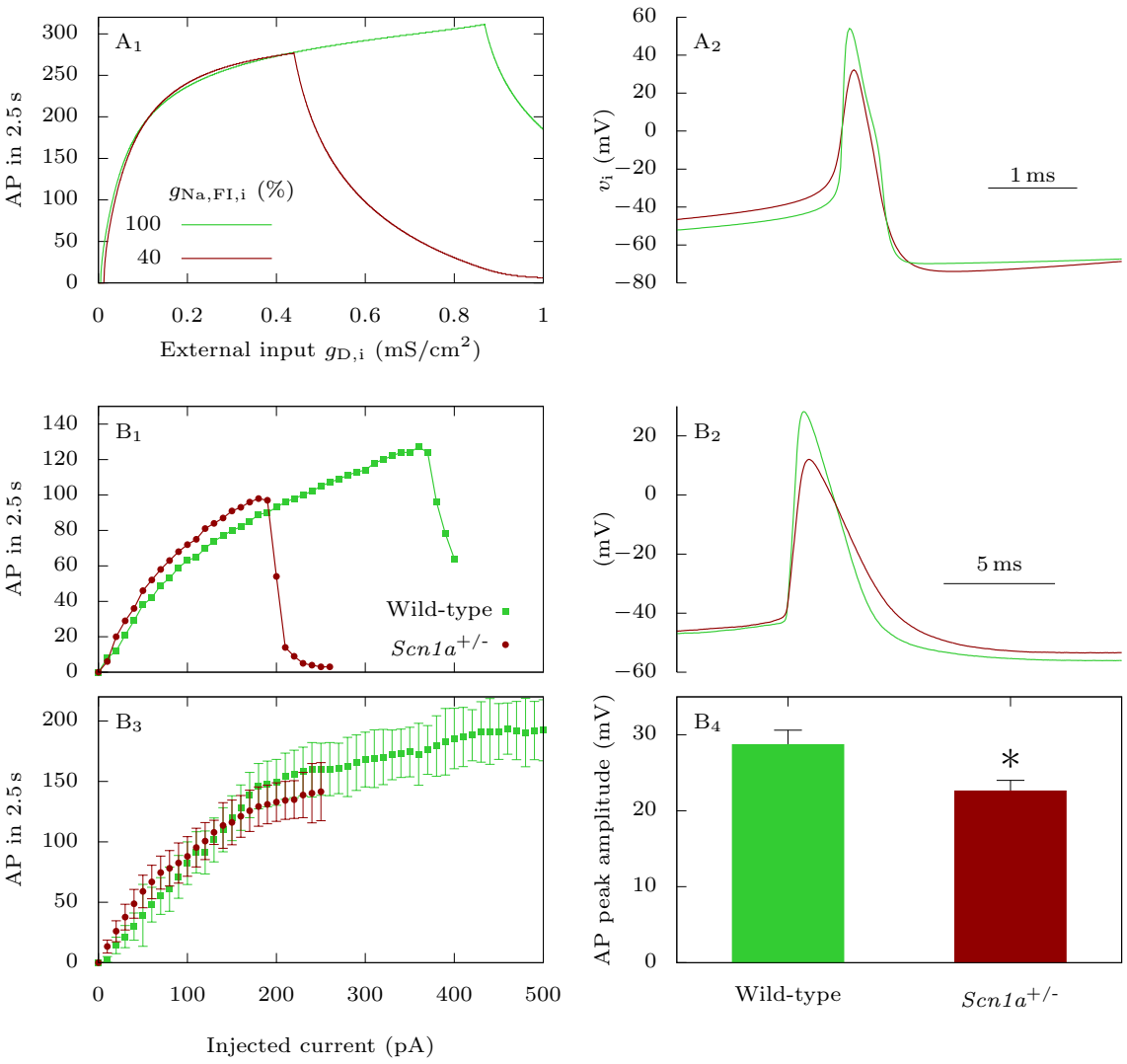


**Figure 3.10: Effect of $Na_V1.1$ epileptogenic mutations on the firing of GABAergic neurons: input-output relationship and action potential amplitude. A.** Model simulations. We applied to the GABAergic neuron at rest 2.5 s long excitatory external inputs of conductances $g_{D,i}$, for the default parameters (wild-type), or for a reduced sodium fast-inactivating maximal conductance $g_{Na,FI,i}$ (epileptogenic mutations). **$A_1$.** Number of action potentials. **$A_2$.** Representative action potentials, for $g_{D,i} = 0.3\,mS \cdot cm^{-2}$. **B.** Experimental data. **$B_1$.** Representative fast spiking neurons recorded in cortical slices from *Scn1a*$^{+/-}$ mice and wild type littermates, selected for having similar input-output curves with lower injected current, showing that the *Scn1a*$^{+/-}$ neuron was more prone to depolarization block (sharp decrease of action potential number). **$B_2$.** Comparison of the first suprathreshold action potential recorded in the neurons selected for panel B1. **$B_3$.** Mean input-output relationships for fast spiking neurons recorded from *Scn1a*$^{+/-}$ ($n = 7$) and wild type littermates ($n = 7$), the number of elicited action potentials was not different, but depolarization block was induced with lower depolarizing current (the traces in which there was depolarization block were excluded, to avoid the influence of depolarization block in the evaluation of the number of action potentials elicited with larger depolarizing currents). **$B_4$.** Mean peak amplitude (absolute value) of the first suprathreshold action potential for fast spiking neurons recorded from *Scn1a*$^{+/-}$ ($22.6 \pm 1.5$ mV, $n = 7$) and wild type littermates ($28.7 \pm 2.0$ mV, $n = 7$); $p = 0.044$ Mann-Whitney test. * $p < 0.05$.

or seizures. For instance, we have not modeled CSD propagation, cell swelling induced by breakdown of ion homeostasis, nor the long lasting depression of activity that can outlasts the neuronal depolarization and may be induced and maintained by other mechanisms

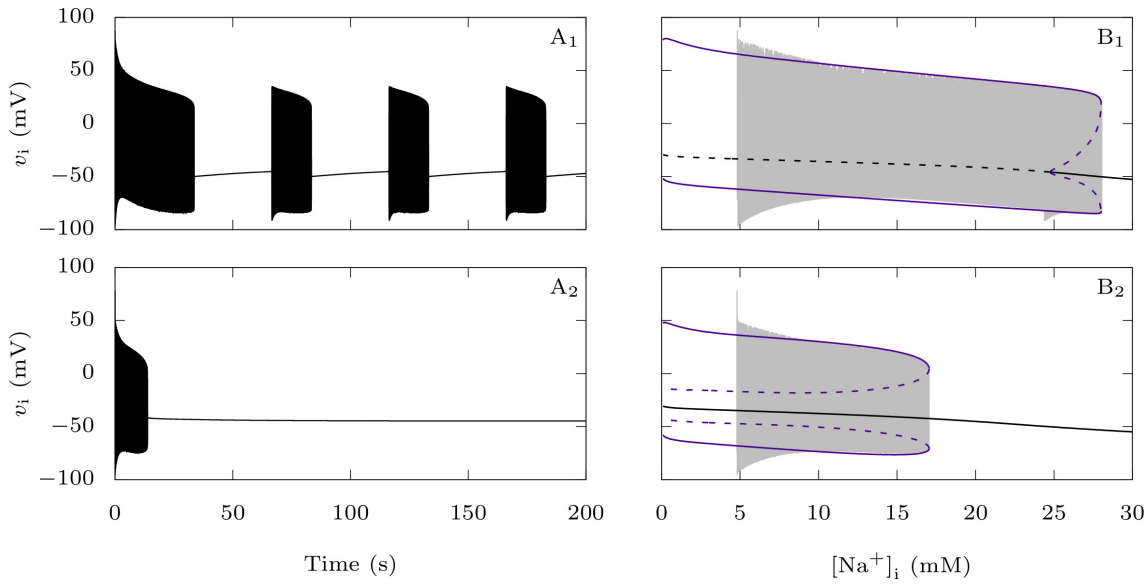


**Figure 3.11: Effect of $Na_V1.1$ epileptogenic mutations on the GABAergic neuron bifurcation structure.** We considered the intracellular sodium concentration as a slow variable and we studied the corresponding fast subsystem where this concentration is a parameter. We focused here on the case where $g_{D,i} = 0.3\,\mathrm{mS \cdot cm^{-2}}$. **A.** Voltage trace of the full system starting from a neuron at rest, for the default parameter values (**$A_1$**) or when the fast-inactivating sodium maximal conductance is reduced to 40 % of its default value (**$A_2$**). **B.** Trajectory of $A_1$ (**$B_1$**) or $A_2$ (**$B_2$**), projected onto the $([Na^+]_i, v_i)$ plane and bifurcation diagram of the fast subsystem with respect to the intracellular sodium concentration. We represented steady-states with black lines and limit cycles with purple lines.

[92, 93]. Similarly, we have not modeled the activity of neuronal networks observed during seizures, nor the propagation of seizures [12].

### 3.4.1 FHM3 mutations

Interestingly, our model did not display a clear-cut increase in firing frequency of the GABAergic neuron implementing a common effect of $Na_V1.1$ FHM3 mutations, although these mutations cause a clear gain of function of the channel. Notably, in a study where FHM3 mutations were implemented in an extended Hodgkin–Huxley model with dynamic ion concentrations [94], Dahlem et al. reported prolonged action potentials in the mutant model resulting in reduced spiking frequency.

Experimentally, the effect of FHM3 mutations on firing features is not completely clear yet. An increase of firing frequency has been observed in GABAergic neurons transfected with the FHM3 mutant L1649Q [6]. Likewise, the application of the toxin Hm1a, which mimics the effect of FHM3 mutations by enhancing the persistent sodium current, induced an increase of firing frequency in fast spiking cortical GABAergic neurons (Chapter 2). However, the same toxin did not modify the firing frequency of CA1 hippocampal GABAergic neurons in [47]. Moreover, comparing heterozygous L1649Q knock-in mice with wild-type littermates, a significant increase of firing frequency has been observed in cortical and hippocampal fast spiking GABAergic neurons, but not in regular spiking cortical and hippocampal GABAergic neurons [39]. The variety of GABAergic neuron subtypes and the great variability of their properties [95, 96] is a possible cause of these discrepancies.

Overall, a noteworthy outcome of the present work is that, in our model, an increase of the firing frequency of the GABAergic neuron is not necessary for FHM3 mutations to

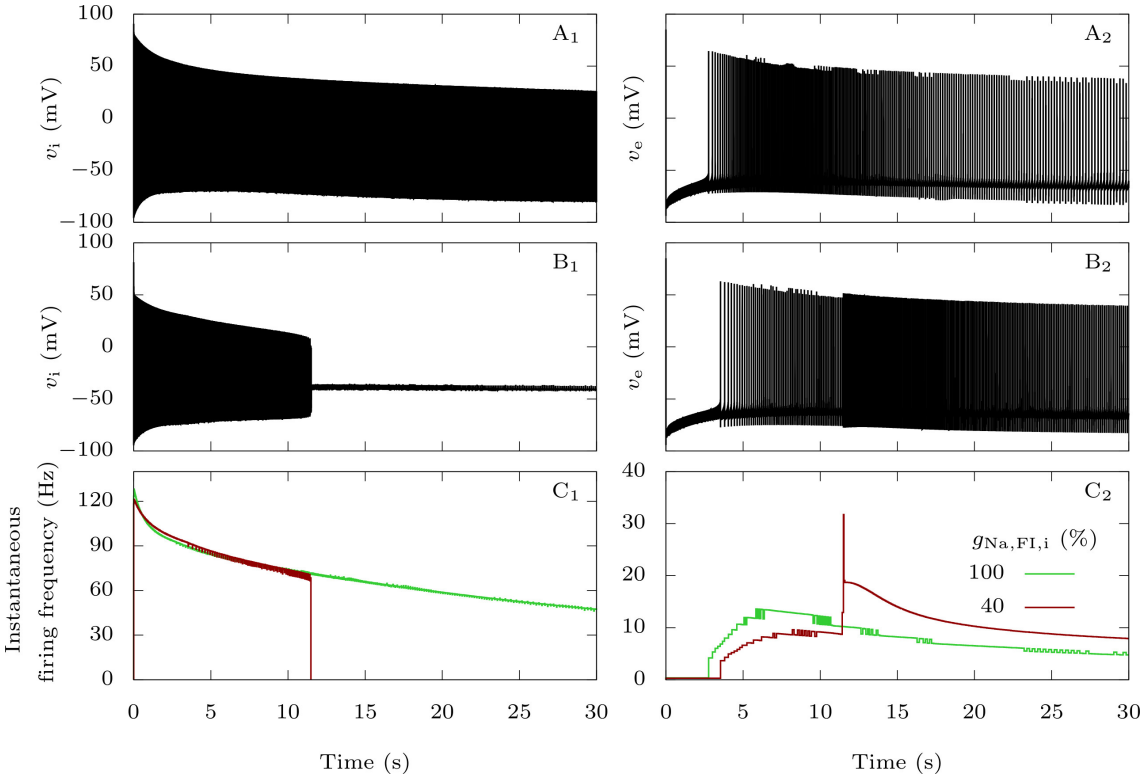


**Figure 3.12: Effect of $Na_V1.1$ epileptogenic mutations on the firing frequency of the pyramidal neuron.** When both neurons are coupled, taking as initial condition the steady-state when there is no external input, we applied external inputs $g_{D,i} = g_{D,e} = 0.3\,mS \cdot cm^{-2}$. We tested both the default parameters, which represent a wild-type GABAergic neuron, and a sodium fast-inactivating maximal conductance $g_{Na,FI,i}$ reduced to 40 % of its default value, to model epileptogenic mutations of $Na_V1.1$. **A.** Voltage of the GABAergic (**$A_1$**) and pyramidal (**$A_2$**) neurons in the wild-type condition. **B.** Voltage of the GABAergic (**$B_1$**) and pyramidal (**$B_2$**) neurons with the epileptogenic mutation. **C.** Instantaneous firing frequency of the GABAergic (**$C_1$**) and pyramidal (**$C_2$**) neurons in the two conditions.

promote network hyperexcitability that leads to CSD initiation. We observed an alternative mechanism in the simulations: although in our model the FHM3 condition induced just small modifications of the GABAergic neuron's firing frequency, the ion fluxes at each action potential were increased, leading to a build-up of extracellular potassium. This is possible because each action potential generates larger and more sustained sodium currents that induce increased activation of potassium currents, causing higher net translocation of ions, including potassium, across the membrane, which is consistent with modeling results from Barbieri et al. [34]. This reduces the threshold for CSD initiation and shortens its latency, even in conditions in which the firing frequency of the GABAergic neuron is reduced.

In our previous work [35], we did not directly model $Na_V1.1$ FHM3 mutations. For simplicity, we instead assumed that these gain of function mutations cause hyperactivity of GABAergic neurons. We therefore focused on the effect of an intense firing of the GABAergic neuron on CSD initiation, obtained by increasing the value of the parameter representing a baseline excitatory drive of the GABAergic neuron. Within this framework, we concluded that a high firing frequency of GABAergic neurons can lead to CSD, through extracellular potassium build-up. Here, we improved the model and explicitly modeled FHM3 mutations with persistent sodium current. We found that the initial accumulation of extracellular potassium leading to the onset of CSD can occur without increase of the

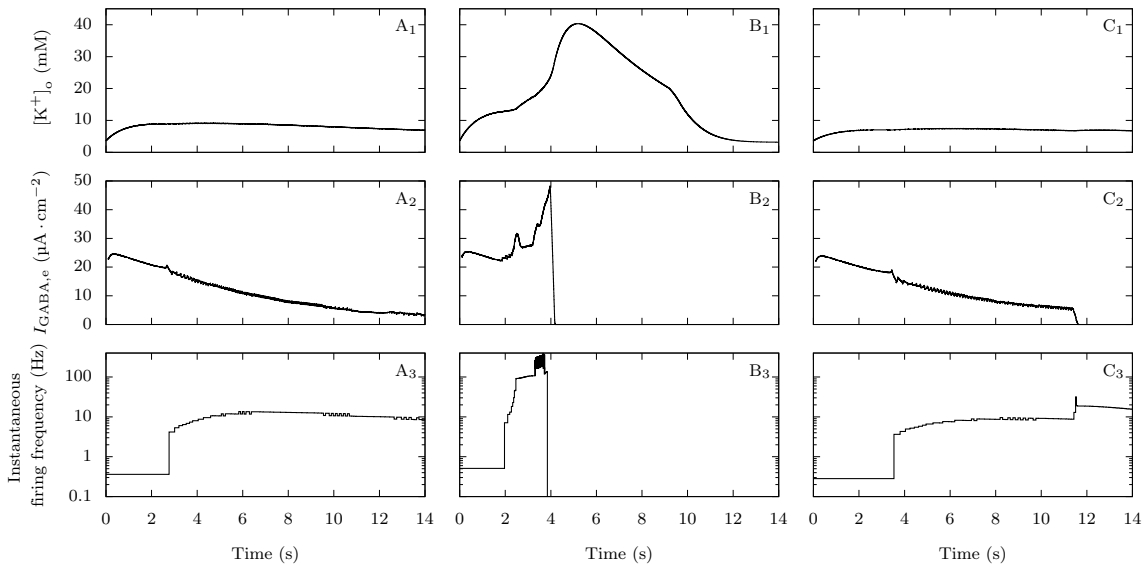


**Figure 3.13: Comparison of migraine and epilepsy scenarios regarding extracellular potassium and GABAergic inhibition.** Plots of the extracellular potassium concentration (upper row), GABAergic neuron's inhibitory current on the pyramidal neuron (second row) and pyramidal neuron's firing frequency (bottom row) corresponding to the simulations displayed in Figs. 3.4 and 3.12. For better readability, we averaged the GABAergic currents on a running window of 200 ms. We show the pyramidal neuron's firing frequency with a logarithmic scale. **A.** Control condition: default parameter values. **B.** Migraine condition: percentage of sodium voltage-gated conductance corresponding to persistent current $p_{Na,P} = 15\,\%$. **C.** Epilepsy condition: sodium fast-inactivating maximal conductance reduced to 40 % of its default value.

GABAergic neuron's firing frequency (Fig. 3.5), since in our model FHM3 mutations affect more the ion fluxes at each action potential than the number of action potentials. Our improved model allows us to simulate also the effect of mutations that cause epilepsy.

### 3.4.2 Epileptogenic mutations

In our model, loss of function of $Na_V1.1$, typical of mutations causing epilepsy (including the developmental and epileptic encephalopathy Dravet syndrome), makes GABAergic neurons more susceptible to depolarization block. The action potential frequency during repetitive firing appears unchanged prior to the depolarization block. Simultaneous to the suppression of spike generation by the GABAergic neuron, we observed the transition to a phase of hyperactivity of the pyramidal neuron. This firing pattern cannot be considered as a seizure-like epileptiform activity, but can be interpreted as an earlier stage of hyperexcitability. A limitation of our model is that it only takes into account two neurons, without including any network dynamics. This allowed us to keep its size manageable, but network effects may be necessary for observing seizure-like activity in simulations. Nevertheless, our work suggests the potentially important role of the depolarization block of GABAergic neurons in epilepsies caused by $Na_V1.1$ loss of function. In particular, our model could reproduce conditions of the pre-epileptic period identified in mouse models, in which there is network hyperexcitability but not spontaneous seizures [68, 97].

There is experimental evidence in favor of facilitated depolarization block of GABAergic neurons as a mechanism of pro-epileptic network hyperexcitability, for both $Na_V1.1$-related and other models.

Our experimental data show that depolarization block is induced by smaller injected currents in fast spiking GABAergic neurons from cortical brain slices of *Scn1a*$^{+/-}$ mice, whereas firing frequency before depolarization block is not significantly modified. There

are several papers in which modifications of the initial part of the input-output curve have not been observed in GABAergic neurons of mouse models carrying $Na_V1.1$ loss of function mutations. This was the case for instance with dissociated hippocampal neurons [22] and with cortical parvalbumin-positive interneurons in brain slices [41] of *Scn1a*$^{+/-}$ mice, as well as with cortical and hippocampal fast spiking GABAergic neurons of *Scn1a*$^{RH/+}$ mice, which carry the $Na_V1.1$ R1648H missense mutation [24]. Notably, the reduced firing frequency observed by numerous studies in the final part of mean input-output relationships, obtained injecting larger depolarizing currents, is likely caused by the earlier depolarization block, which reduces the number of action potentials elicited by large depolarizations in neurons expressing $Na_V1.1$ loss of function mutants. In fact, the most consistent effect observed in the representative fast spiking discharges displayed by most of the papers is earlier depolarization block. It should be highlighted again that these traces have not been included in the mean input-output curves that we have presented here.

In an experimental model in which seizure-like events were induced in rat hippocampal slices from wild type mice using the potassium channel blocker 4-aminopyridine together with decreased magnesium, a sequence of events similar to what we obtained in our simulations was reported: seizure generation correlated with long-lasting depolarization blocks in GABAergic neurons and the simultaneous increase of firing frequency in pyramidal cells [98]. Another study, which used 4-aminopyridine together with decreased magnesium and local applications of NMDA to focally induce epileptiform ictal activity in wild type cortical rodent brain slices, suggested that depolarization block of fast spiking GABAergic neurons allows the recruitment of clusters of pyramidal cells into propagating epileptiform discharges [99]. Consistently, a computational modeling study found that seizure-like activity can arise as the result of depolarization block of inhibitory neurons and investigated possible bifurcation structures for this transition [100].

Interestingly, a neuronal mass computational model of Dravet syndrome generated, when abnormal depolarizing $GABA_A$ currents were implemented (which would make GABAergic synaptic connections excitatory), seizure-like activity that was similar to some EEG patterns observed in Dravet syndrome patients [101]. The rationale for implementing this effect was a hypothetical remodeling in which the initial $Na_V1.1$-induced hyperexcitability leads to the cleavage of KCC2 co-transporters, resulting in intracellular accumulation of chloride in pyramidal neurons. Our model takes into account KCC2 co-transporters and dynamic chloride concentrations, but we did not implement remodeling that leads to reduced KCC2 function. In fact, although depolarizing GABA has been reported in a mouse model of Dravet syndrome, it was not found to be significantly involved in seizure activity [102]. Conversely, it would be interesting to include depolarization block of GABAergic neurons in the neuronal mass computational model of Dravet syndrome [101], for example by adapting the corresponding wave-to-pulse function for taking it into account.

### 3.4.3 Conclusion

Overall, our results suggest that depolarization block can be involved in the mechanism of both gain of function migraine mutations and loss of function epilepsy mutations of $Na_V1.1$, but with different features. In the migraine condition spiking-induced increased extracellular potassium leads to depolarization block of both GABAergic and glutamatergic neurons, whereas in the epilepsy condition depolarization block of GABAergic neurons leads to hyperexcitability of glutamatergic neurons. Notably, modifications of firing frequency of the GABAergic neurons are not necessary for inducing these effects.

Our results that disclose different pathological mechanisms leading to CSD and epileptic activity are consistent with the finding that often epileptic networks are resistant to

CSD induction: In several models, the propensity to CSD generation seems to decline during the course of epileptogenesis, whereas the propensity to spontaneous epileptic seizures increases. For instance, the threshold for high potassium-induced CSD was increased in neocortical slices both from patients who had undergone surgery for intractable epilepsy and from chronic epilepsy rats following pilocarpine-induced status epilepticus, whereas brain slices from age-matched healthy control rats that showed a lower threshold [48]. Similarly, the propensity to spreading depolarization was reduced during the epileptogenesis induced by blood-brain barrier disruption and pentylenetetrazol kindling in rats [49, 103]. Thus, the dissociation between propensity to spreading depolarization on the one hand and epileptic seizures on the other hand could be a general feature beyond FHM3 and *SCN1A*-linked epilepsies.

## Acknowledgments

We thank Tobias Freilinger (Department of Neurology and Epileptology, Hertie Institute for Clinical Brain Research, University of Tübingen, Tübingen, Germany) for sharing unpublished results as personal communication. Our laboratories are members of the Interdisciplinary Institute for Modeling in Neuroscience and Cognition (NeuroMod) of the Université Côte d'Azur (France) and of the "Fédération Hospitalo-Universitaire" InovPain (FHU-InovPain, France).

# Chapter 4

# Idealized multiple-timescale model of CSD initiation and pre-epileptic hyperactivity

## 4.1 Introduction

In this chapter, we investigate dynamic bifurcation scenarios associated with the onset of CSD or epileptiform activity caused by $Na_V1.1$ mutations in a multiple-timescale idealized model. Slow-fast dissection [91, 104] is indeed a powerful tool to study the spectrum of activity regimes in the neuronal context. We initiated this approach in Chapter 3 (see Fig. 3.11), however the size of the model made it prohibitive to perform a thorough analysis. For this reason, we build here a 6-dimensional minimal version of the detailed biophysical model. To keep it as simple as possible, we mainly use polynomial terms, except for the modeling of the aspects which we assume to play an essential role in the pathological mechanisms of $Na_V1.1$ mutations: spiking-induced release of potassium in the case of migraine and synaptic inhibition in the case of epilepsy.

We design the idealized system in such a way to have three explicit timescales. Neuronal dynamics is the fastest, each neuron being modeled by a two-dimensional oscillator. The extracellular potassium concentration is then an obvious choice of slow variable to drive the system to pathological regimes. Based on Hübel et al., we introduce a third timescale which is even slower than the potassium [105], an approach also used in [106, 107]. This choice is motivated by the characteristic potassium dynamics at the site of CSD initiation shown in Fig. 4.1. The initial progressive accumulation is followed by an abrupt increase, which hints at an additional timescale underlying potassium dynamics.

We first study the slow dynamics of the potassium concentration with tools from dynamical systems theory such as phase-plane analysis and invariant manifolds. To unravel the complicated bifurcation structure of the fast layer problem, we then perform numerical continuation with the software package AUTO [108]. Finally, we gather information obtained from the slow and fast components to interpret the dynamics of the full system, namely transitions from physiological firing to CSD and epileptiform hyperactivity.

## 4.2 The model

We consider a pair of neurons: a pyramidal neuron ($x_e$, $y_e$) and a GABAergic interneuron ($x_i$, $y_i$). Each neuron is modeled using a modified Hindmarsh–Rose system (see Section 4.2.2). They can be stimulated by an external current $I_{ext}$. We implemented an inhibitory synapse from the GABAergic neuron to the pyramidal one, with the current $I_{GABA}$ (see Section 4.2.3). We also modeled the dynamics of the extracellular potassium, using a two-dimensional system ($[K]_o^+$, $w$) (see Section 4.2.4). The firing of the neurons

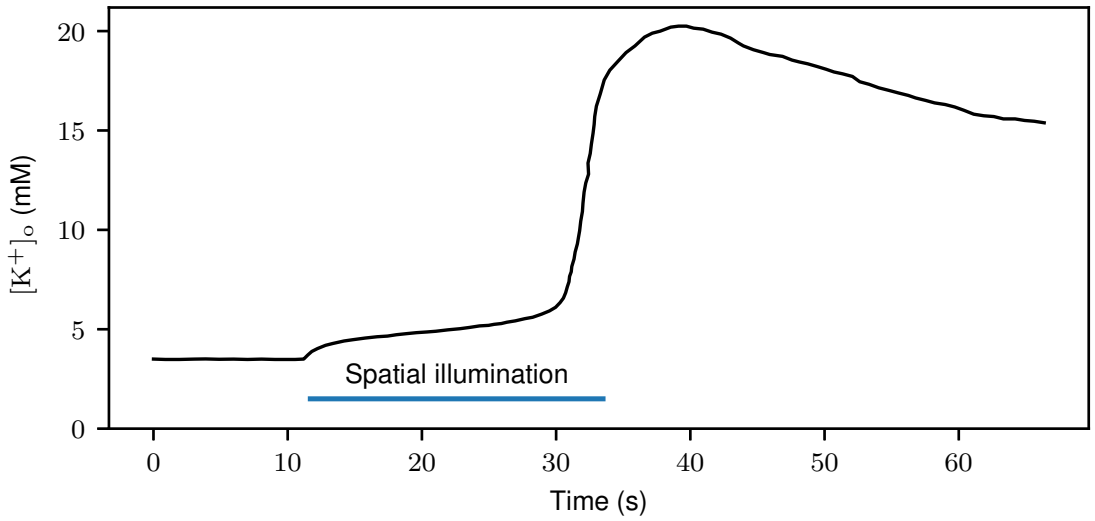


**Figure 4.1: Extracellular potassium dynamics at the site of CSD initiation.** We reproduce here the potassium trace shown in Fig. 2.8 B, which was recorded at the site of CSD initiation. Spatial optogenetic illumination was used to specifically control the area of induction.

releases potassium in the extracellular space, which we account for with the terms $pg(x_\mathrm{i})$ and $g(x_\mathrm{e})$ (see Sections 4.2.5 and 4.2.6). Conversely, we take into account the depolarizing effect of extracellular potassium on the neurons. The overall system has three main timescales, see Section 4.2.1.

The dynamics of the full system is given in (4.1). Fig. 4.2 shows a schematic representation of the system. The state variables are listed in Table 4.1 and the model parameters in Table 4.2.

$$\frac{\mathrm{d}x_\mathrm{e}}{\mathrm{d}t} = c_\mathrm{e}\left(x_\mathrm{e} - \frac{x_\mathrm{e}^3}{3} - y_\mathrm{e} + [\mathrm{K}]_\mathrm{o}^+ + I_\mathrm{ext} - I_\mathrm{GABA}(x_\mathrm{e}, x_\mathrm{i})\right) \tag{4.1a}$$

$$\frac{\mathrm{d}y_\mathrm{e}}{\mathrm{d}t} = \frac{x_\mathrm{e}^2 + dx_\mathrm{e} - by_\mathrm{e} + a}{c_\mathrm{e}} \tag{4.1b}$$

$$\frac{\mathrm{d}x_\mathrm{i}}{\mathrm{d}t} = c_\mathrm{i}\left(x_\mathrm{i} - \frac{x_\mathrm{i}^3}{3} - y_\mathrm{i} + [\mathrm{K}]_\mathrm{o}^+ + I_\mathrm{ext}\right) \tag{4.1c}$$

$$\frac{\mathrm{d}y_\mathrm{i}}{\mathrm{d}t} = \frac{x_\mathrm{i}^2 + dx_\mathrm{i} - by_\mathrm{i} + a}{c_\mathrm{i}} \tag{4.1d}$$

$$\frac{\mathrm{d}[\mathrm{K}]_\mathrm{o}^+}{\mathrm{d}t} = \varepsilon\left(w - f([\mathrm{K}]_\mathrm{o}^+) + pg(x_\mathrm{i}) + g(x_\mathrm{e})\right) \tag{4.1e}$$

$$\frac{\mathrm{d}w}{\mathrm{d}t} = \varepsilon\delta(-z - \alpha + \beta w) \tag{4.1f}$$

### 4.2.1 Slow-fast structure

By construction, there are three main timescales in the six-dimensional model defined by System (4.1):

- The neuron variables ($x_\mathrm{e}$, $y_\mathrm{e}$, $x_\mathrm{i}$, $y_\mathrm{i}$) are faster than the potassium ones ($[\mathrm{K}]_\mathrm{o}^+$, $w$), through the presence of the small parameter $0 < \varepsilon \ll 1$, which we set to be of order $10^{-3}$ in simulations (Table 4.2). We call the four-dimensional subsystem

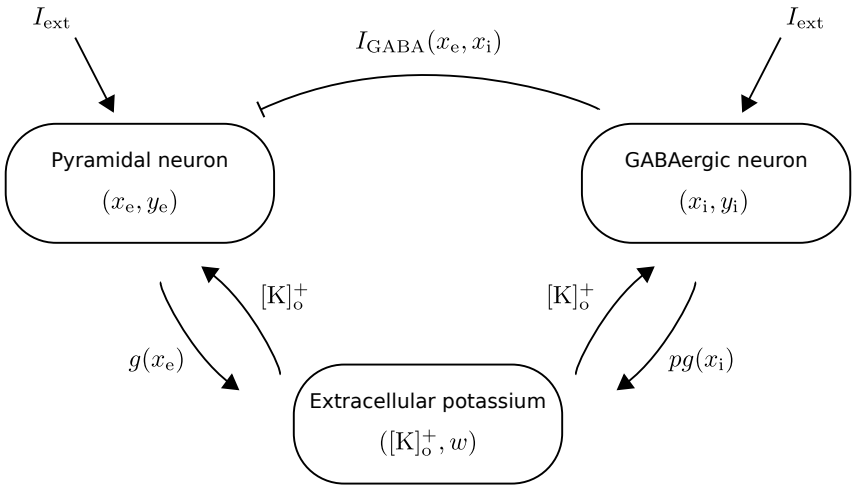


**Figure 4.2: Schematic representation of the model.**

**Table 4.1:** State variables.

| Symbol | Description | Timescale |
|---|---|---|
| $x_{\text{e}}$ | Membrane potential of the pyramidal neuron | Fast |
| $y_{\text{e}}$ | Gating variable for the pyramidal neuron | Fast |
| $x_{\text{i}}$ | Membrane potential of the GABAergic neuron | Fast |
| $y_{\text{i}}$ | Gating variable for the GABAergic neuron | Fast |
| $[\text{K}]_{\text{o}}^{+}$ | Extracellular potassium concentration | Slow |
| $w$ | Additional variable for the dynamics of $[\text{K}]_{\text{o}}^{+}$ | Superslow |

($x_{\text{e}}$, $y_{\text{e}}$, $x_{\text{i}}$, $y_{\text{i}}$) the fast block and the two-dimensional subsystem ($[\text{K}]_{\text{o}}^{+}$, $w$) the slow block or potassium block.

- Inside this slow block, there are also two separated timescales, $[\text{K}]_{\text{o}}^{+}$ being faster than $w$ due to the small parameter $0 < \delta \ll 1$. See Section 4.3 for a detailed study of the potassium block.

System (4.1) is therefore a slow-fast system with four fast, one slow and one superslow variable.

Note that $w$ does not enter the equations of the fast block. By definition, letting $\varepsilon \to 0$ in System (4.1) yields the *fast layer problem* [110]. It corresponds to freezing the dynamics of $[\text{K}]_{\text{o}}^{+}$ and considering it as a parameter of the fast block ($x_{\text{e}}$, $y_{\text{e}}$, $x_{\text{i}}$, $y_{\text{i}}$). In Section 4.4, we will study the bifurcation structure of the fast layer problem to better understand the dynamic transitions in the full system (4.1).

Inside each neuron model, the membrane potential $x_{\text{e,i}}$ is faster than the variable $y_{\text{e,i}}$ which models ion channels dynamics. This timescale separation, which we do not analyze as such in this work, is organized by the parameters $c_{\text{e,i}}$. However we exploit it to obtain the transition to epileptiform hyperactivity (see Section 4.2.6.2).

**Table 4.2:** Model parameters.

| | Symbol | Description | Value |
|---|---|---|---|
| | $I_{\text{ext}}$ | External input | 0.35 |
| **Slow-fast structure** | | | |
| | $\varepsilon$ | $([\text{K}]_{\text{o}}^{+}, w)$ *vs.* neurons | 0.002 |
| | $\delta$ | $w$ *vs.* $[\text{K}]_{\text{o}}^{+}$ | 0.005 |
| **Neuronal dynamics** | | | |
| | $a$ | | 0.56 [109] |
| | $b$ | | 1.2 |
| | $c_{\text{e}}$ | $c$ for the pyramidal neuron | 3 [109] |
| | $c_{\text{i}}$ | $c$ for the GAGAbergic neuron | Wild-type: 3 [109]<br>Epilepsy: 1.2 |
| | $d$ | | 1.8 |
| **Inhibitory synapse** | | | |
| | $g_{\text{GABA}}$ | Maximal conductance | 15 |
| | $E_{\text{GABA}}$ | Reversal potential | -2.5 |
| | $k_{\text{GABA}}$ | Sigmoids slope parameter | 20 |
| | $\theta_{\text{GABA},1}$ | Increasing sigmoid midpoint | -1 |
| | $\theta_{\text{GABA},2}$ | Decreasing sigmoid midpoint | 0.1 |
| **$[\text{K}^+]_{\text{o}}$ dynamics** | | | |
| | $z_{\text{l}}$ | $[\text{K}]_{\text{o}}^{+}$-nullcline local maximum[1] | 0.5 |
| | $z_{\text{r}}$ | $[\text{K}]_{\text{o}}^{+}$-nullcline local minimum[1] | 1.5 |
| | $\beta$ | Controls $w$-nullcline slope[1] | -13 |
| | $\alpha$ | Controls $w$-nullcline intercept[1] | -2.6 |
| **$\text{K}^+$ release** | | | |
| | $g_{\text{K}}$ | Maximal neuronal contribution | 0.015 |
| | $k_{\text{K}}$ | Sigmoid slope parameter | 10 |
| | $\theta_{\text{K}}$ | Sigmoid midpoint | 0.6 |
| | $p$ | $\text{K}^+$ release scaling factor | Wild-type: 1<br>Migraine: 4 |

[1] For the slow block, see Section 4.2.4.

### 4.2.2 Neuronal dynamics

We model each neuron with a two-dimensional system inspired from Hindmarsh and Rose:

$$\begin{aligned} \frac{\mathrm{d}x}{\mathrm{d}t} &= c\left(x - \frac{x^3}{3} - y + I\right) \\ \frac{\mathrm{d}y}{\mathrm{d}t} &= \frac{x^2 + dx - by + a}{c} \end{aligned} \tag{4.2}$$

We took most parameter values from [109], except for $b$ which we increased to shift the fold bifurcation of limit cycles responsible for the transition to depolarization block to larger values of $I$ (Table 4.2). Compared to the original model [111], System (4.2) has been modified [112] so that spike generation is mediated by a saddle-node on invariant circle (SNIC) instead of a saddle homoclinic bifurcation (Fig. 4.3). It exhibits thus class 1 excitability.

This is consistent with the experimental input-output relationships in Fig. 2.2 B, E. They were recorded in neocortical pyramidal and fast-spiking GABAergic neurons of mice, before or during the application of the toxin Hm1a which mimics the effect of $Na_V1.1$ migraine mutations. It is also consistent with Figure 4 and Supplementary Figure 4 of [39], for cortical fast-spiking and regular spiking GABAergic neurons of wild-type or heterozygous *Scn1a*$^{+/-\ \mathrm{L1649Q}}$ knock-in mice.

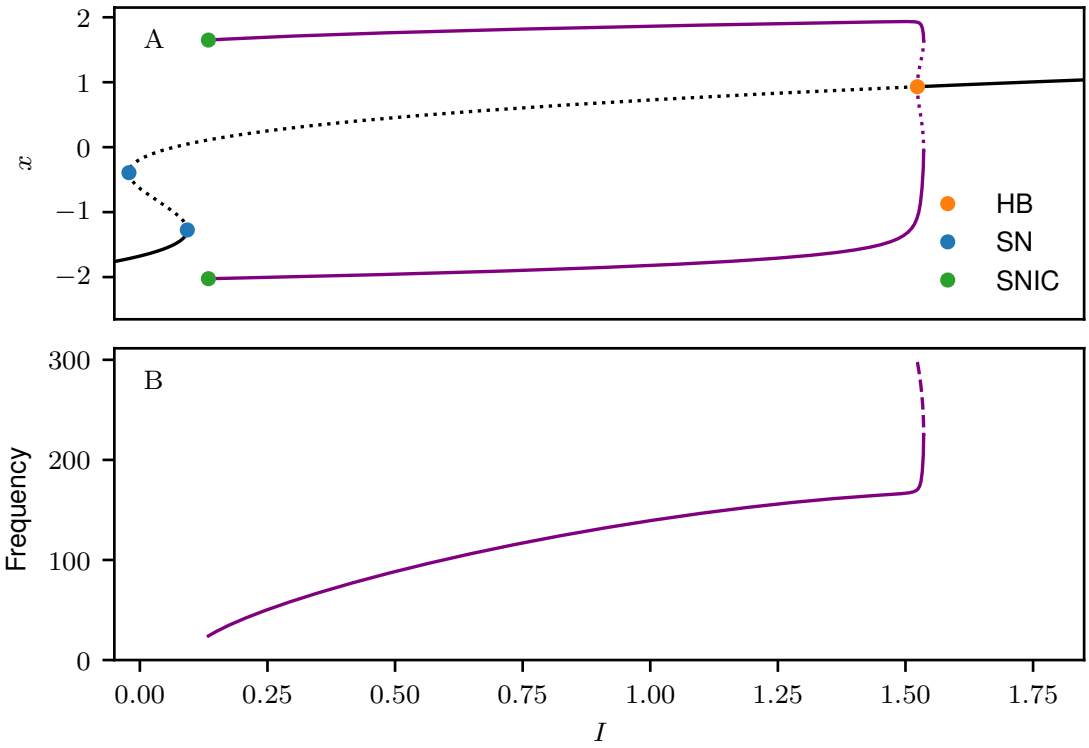


**Figure 4.3: Dynamics of a single neuron. A.** Bifurcation diagram $x$ *vs.* $I$ of System (4.2). The black curves show families of stable (solid line) or unstable (dashed line) steady states. The purple lines show families of stable or unstable limit cycles. HB: Hopf bifurcation, here subcritical. SN: Saddle-node bifurcation of steady states. SNIC: saddle-node on invariant circle bifurcation. **B.** Frequency of the limit cycles.

### 4.2.3 Inhibitory synapse

Although this model is very simplified with respect to the one developed and studied in Chapter 3, we did not remove the GABAergic synapse from the GABAergic neuron to the pyramidal one. This inhibitory connection is especially important in the case of the epileptogenic mutations of $Na_V1.1$ (see Section 4.5.2).

To keep the model as simple as possible, we decided not to use any additional synaptic variable or resetting rule. Instead, we scale the maximal conductance $g_{\mathrm{GABA}}$ of the

inhibitory synaptic current $I_{\mathrm{GABA}}$ by a function $s$ of the voltage:

$$I_{\mathrm{GABA}} = g_{\mathrm{GABA}} s(x_{\mathrm{i}}) \left(x_{\mathrm{e}} - E_{\mathrm{GABA}}\right).$$

The function $s$ is inspired from [113]. However, to prevent inhibition during depolarization block of the GABAergic neuron, we multiply the increasing sigmoid by a decreasing sigmoid of larger midpoint:

$$s(x_{\mathrm{i}}) = \frac{1}{1 + e^{-k_{\mathrm{GABA}}(x_{\mathrm{i}} - \theta_{\mathrm{GABA},1})}} \frac{1}{1 + e^{-k_{\mathrm{GABA}}(-x_{\mathrm{i}} + \theta_{\mathrm{GABA},2})}}.$$

### 4.2.4 $[\mathrm{K}^+]_{\mathrm{o}}$ dynamics

To model the dynamics of the extracellular potassium, we use a two-dimensional slow-fast block, $w$ being slower than $[\mathrm{K}]_{\mathrm{o}}^+$:

$$\begin{aligned} \frac{\mathrm{d}[\mathrm{K}]_{\mathrm{o}}^+}{\mathrm{d}t} &= w - f([\mathrm{K}]_{\mathrm{o}}^+) + g_{\mathrm{tot}} \\ \frac{\mathrm{d}w}{\mathrm{d}t} &= \delta(-z - \alpha + \beta w) \end{aligned} \tag{4.3}$$

where

$$f([\mathrm{K}]_{\mathrm{o}}^+) = \frac{([\mathrm{K}]_{\mathrm{o}}^+)^3}{3} - \frac{1}{2}(z_l + z_r)([\mathrm{K}]_{\mathrm{o}}^+)^2 + z_l z_r [\mathrm{K}]_{\mathrm{o}}^+.$$

This approach is based on [105], where Hübel et al. model potassium dynamics during SDs. They proposed to take into account buffering mechanisms taking place at even slower timescales than the usual slow ion concentration *vs.* fast membrane potential separation. See for example Figure 11 of [105].

System (4.3) is inspired by the FitzHugh–Nagumo (FHN) model [114, 115]. We wanted to have both a low (physiological) and a high (pathological) stable steady states for $[\mathrm{K}]_{\mathrm{o}}^+$, with a region of bistability and a threshold effect for the transition to the high state. System (4.3) allows us to obtain those elements (see Section 4.3) with only polynomial terms. The idea is to reproduce the initially slow increase of $[\mathrm{K}]_{\mathrm{o}}^+$ followed by a sharp rise, which is observed experimentally at the site of CSD initiation Fig. 4.1.

### 4.2.5 Potassium release

In addition to synaptic inhibition (see Section 4.2.3), another key aspect we retain from the biophysical model of Chapter 3 is the release of potassium by the neurons. Indeed, we concluded from our experimental (Fig. 2.6) and simulation (Figs. 3.7 and 3.8) results that activity-dependent accumulation of potassium plays a key role in CSD initiation.

We model the contribution of each neuron with a sigmoid function $g$ of the voltage, which appears in Eq. (4.1e):

$$g(x) = g_{\mathrm{K}} \frac{1}{1 + e^{-k_{\mathrm{K}}(x - \theta_{\mathrm{K}})}}.$$

The intended effect is that each action potential increments $[\mathrm{K}]_{\mathrm{o}}^+$, similarly to what we obtained with the detailed model in Fig. 3.3 $\mathrm{C}_1$ - $\mathrm{C}_3$, to model the generated fluxes of $\mathrm{K}^+$ ions through voltage-gated channels. It allows us to model $\mathrm{Na_V}1.1$ migraine mutations, see Section 4.2.6.

### 4.2.6 $Na_V1.1$ mutations

#### 4.2.6.1 Migraine

In our simulations of the detailed model in Chapter 3, $Na_V1.1$ migraine mutations amplify the net potassium efflux at each action potential of the GABAergic neuron (Fig. 3.3 $C_1$ - $C_3$). Based on this, we scale the term $g(x_i)$ described above by $p = 4$ in Eq. (4.1e) for the migraine condition.

#### 4.2.6.2 Epilepsy

In Chapter 3, both model simulations and experimental recordings on cortical slices from *Scn1a*$^{+/-}$ mice suggest the same: $Na_V1.1$ loss of function renders GABAergic neurons more susceptible to depolarization block (Fig. 3.10). This hypothesis is consistent with other recordings on *Scn1a*$^{+/-}$ mice, see for example Figure 5 of [22].

To obtain this effect in our phenomenological model, we reduce the value of the parameter $c$ for the GABAergic neuron (parameter $c_i$ in the full system). For the default parameter values ($c = 3$), the switch from repetitive firing to depolarization block occurs through a fold of limit cycle bifurcation at $I \approx 1.52$ (Fig. 4.4 $A_1$). When we decrease the value of $c$ to 1.2 (Fig. 4.4 $A_2$), this transition happens via a supercritical Hopf bifurcation. Compared to the subcritical Hopf in Fig. 4.4 $A_1$, this Hopf bifurcation has been shifted to a much lower input value: $I \approx 0.43$, see the 2-parameter bifurcation diagram in the $(I, c)$ parameter plane in Fig. 4.4 B. Note that the saddle-node bifurcations are unaffected, since $c$ does not influence the shape of the equilibrium branch. Reducing the value of $c_i$ in the full system is thus a convenient way to model $Na_V1.1$ epileptogenic mutations.

## 4.3 Slow block

In this section, we analyze the flow of the slow and superslow variables, $[K]_o^+$ and $w$, respectively. However, we do not constrain it on the critical manifold of the system, i.e. the intersection of the nullsurfaces for $x_{e,i}$ and $y_{e,i}$, since it is not required for the understanding of the transition from physiological firing activity to depolarization block. Indeed, instead of introducing the complete *slow subsystem* associated with the full system Eq. (4.1), studying the slow block defined by System (4.3) is enough for this, as we will see in Section 4.5.1. For convenience, we show again here its equations:

$$\begin{aligned} \frac{d[K]_o^+}{dt} &= w - f([K]_o^+) + g_{tot} \\ \frac{dw}{dt} &= \delta(-z - \alpha + \beta w) \end{aligned} \tag{4.3}$$

We computed the bifurcation diagram of (4.3) with respect to the parameter $g_{tot}$ (Fig. 4.5), which represents the contribution of neuronal firing. The lower branch of stable equilibria in Fig. 4.5 corresponds to physiological levels of extracellular potassium while the upper one corresponds to pathological states. There is a range of positive values of $g_{tot}$ for which the system is bistable. Fig. 4.6 depicts the phase portrait of System (4.3) for two nearby values of $g_{tot}$ (solid and dashed) in this zone of bistability. At the intersection of the nullclines, we can see the two stable equilibria and a saddle point between them, much closer to the lower equilibria. The stable invariant manifold of this saddle acts as a threshold: it defines the boundary between the bassins of attractions of the two attractors. This threshold is sensitive to variations of $g_{tot}$. To illustrate this effect, we plotted in purple two trajectories from the same initial condition for the two values of $g_{tot}$. Even though they are very close, the outcome is completely different. When $g_{tot} = 0.0074$, the system

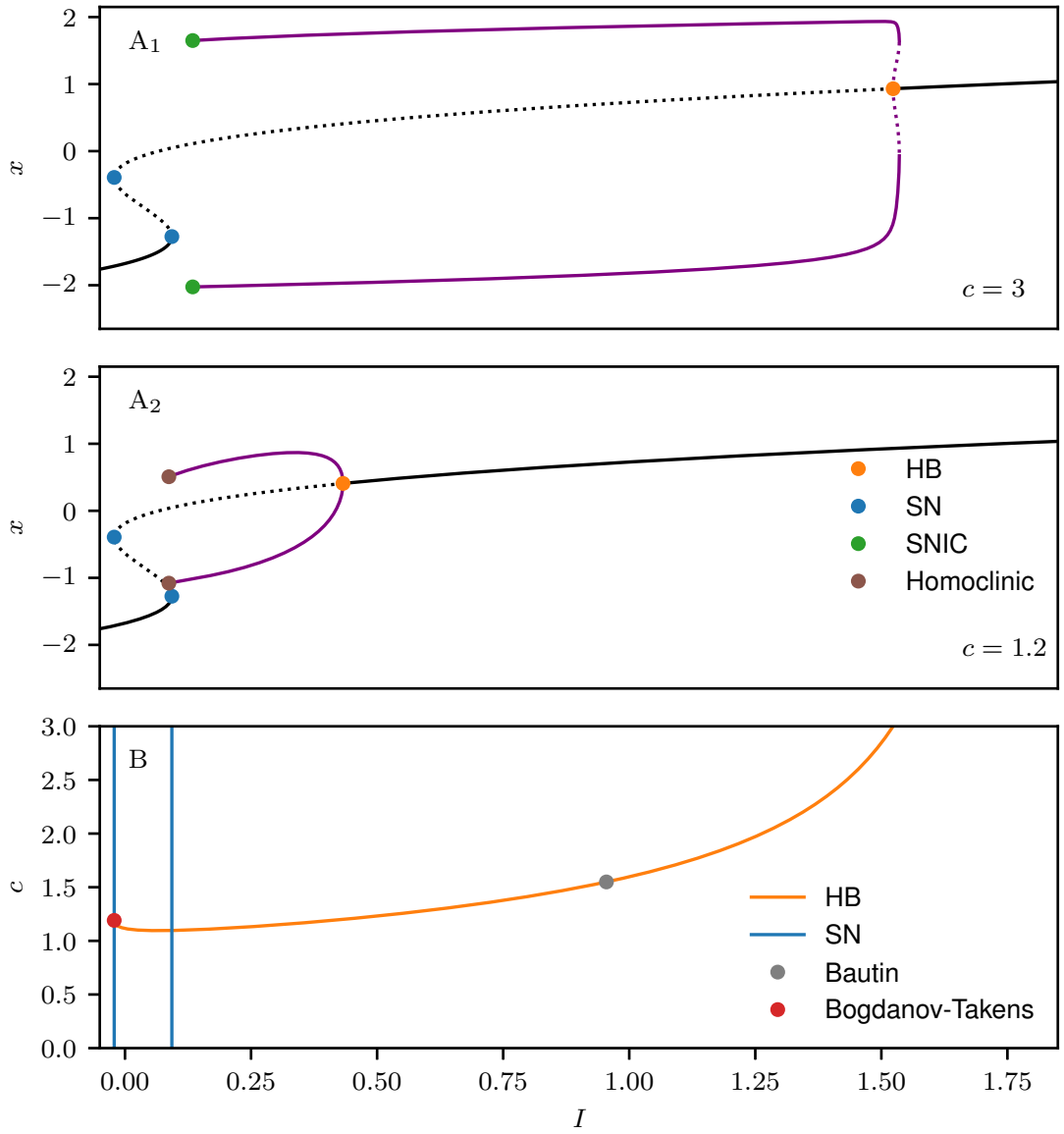


**Figure 4.4: Modeling $Na_V1.1$ epileptogenic mutations. $A_1$.** Bifurcation diagram $x$ *vs.* $I$ of System (4.2) for the default parameter values ($c = 3$: wild-type condition). **$A_2$.** Bifurcation diagram when $c$ is reduced to 1.2 to model $Na_V1.1$ epilepsy mutations. The bifurcation corresponding to the transition to depolarization block (here supercritical Hopf) occurs at a much smaller value of $I$ than in $A_1$. **B.** 2-parameter bifurcation diagram in the $(I, c)$ plane. At the Bautin bifurcation, the criticality of the Hopf changes, from subcritical (like in A1) to supercritical (like in A2).

converges to the physiological equilibrium while when $g_{tot} = 0.0075$ it converges to the pathological one.

It is important to note that the term $g_{tot} = pg(x_i) + g(x_e)$ in the full system (4.1) is not slow, since it depends on the membrane potentials $x_e$ and $x_i$. In the time traces of the full system shown in Fig. 4.9, we can see it oscillating rapidly compared to $[K]_o^+$ and $w$. Furthermore, the amplitude of the oscillations is large enough to move substantially across the bifurcation diagram in Fig. 4.5. It can thus seem surprising to treat it as a bifurcation parameter. However, as we will see in Section 4.5.1, we can still relate the behavior of the full system to the analysis of the System (4.3) where $g_{tot}$ is a parameter, looking at the evolution of $pg(x_i) + g(x_e)$ averaged on a sliding window (blue curves in Fig. 4.9 $A_5, B_5$,

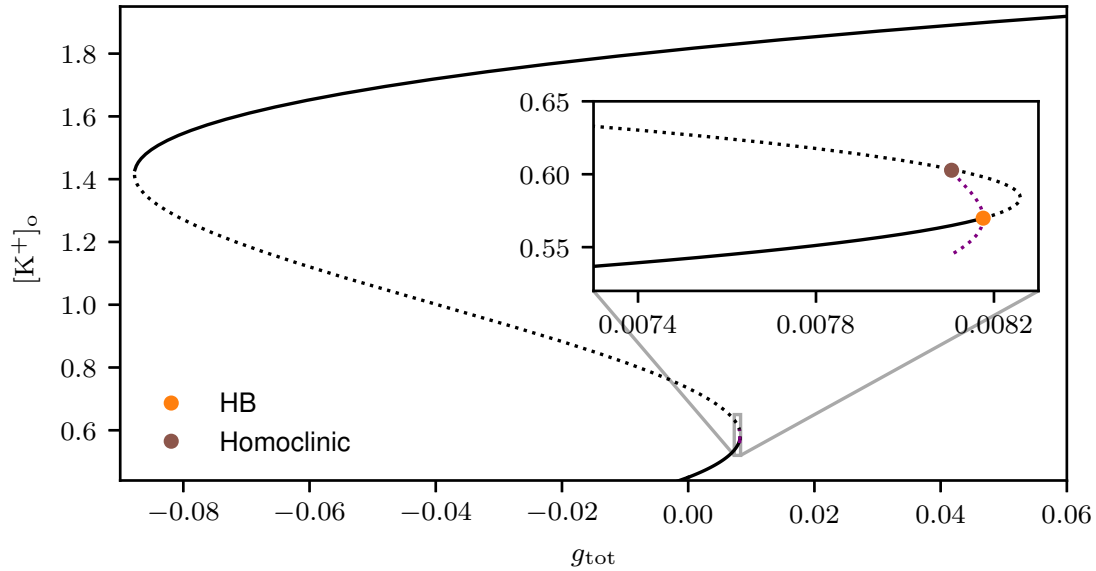


**Figure 4.5: Bistability of the potassium block.** Bifurcation diagram $[K]_o^+$ *vs.* $g_{tot}$ of System (4.3).

$C_5$ and Fig. 4.12 B).

The potassium block is itself a slow-fast system; its timescale separation is organized by parameter $\delta$. When $\delta$ is at its default value ($\delta = 0.005$), $[K]_o^+$ is faster than $w$. The sensitivity of the stable manifold of the saddle is preserved even when increasing $\delta$ beyond the point where the roles of the two variables are exchanged, $w$ becoming faster than $[K]_o^+$. This is for example the case for $\delta = 1$. Regarding this aspect, having three timescales (superslow, slow and fast) in the full system is not crucial for modeling the jump to the high potassium state. However, we noticed that a small value of $\delta$ is necessary to obtain an overshoot in the trace of $[K]_o^+$ before convergence to the upper equilibrium. Such an overshoot is consistent with the experimental trace of Fig. 4.1. When $[K]_o^+$ is the fast variable of the potassium block, the trajectory is almost horizontal until the cubic nullcline, before moving down slowly along it (solid purple line in Fig. 4.6 A). This shapes the overshoot. On the other hand, when $w$ is the fast variable, the trajectory converges to the upper equilibrium along the $w$-nullcline, which does not produce any overshoot (not shown).

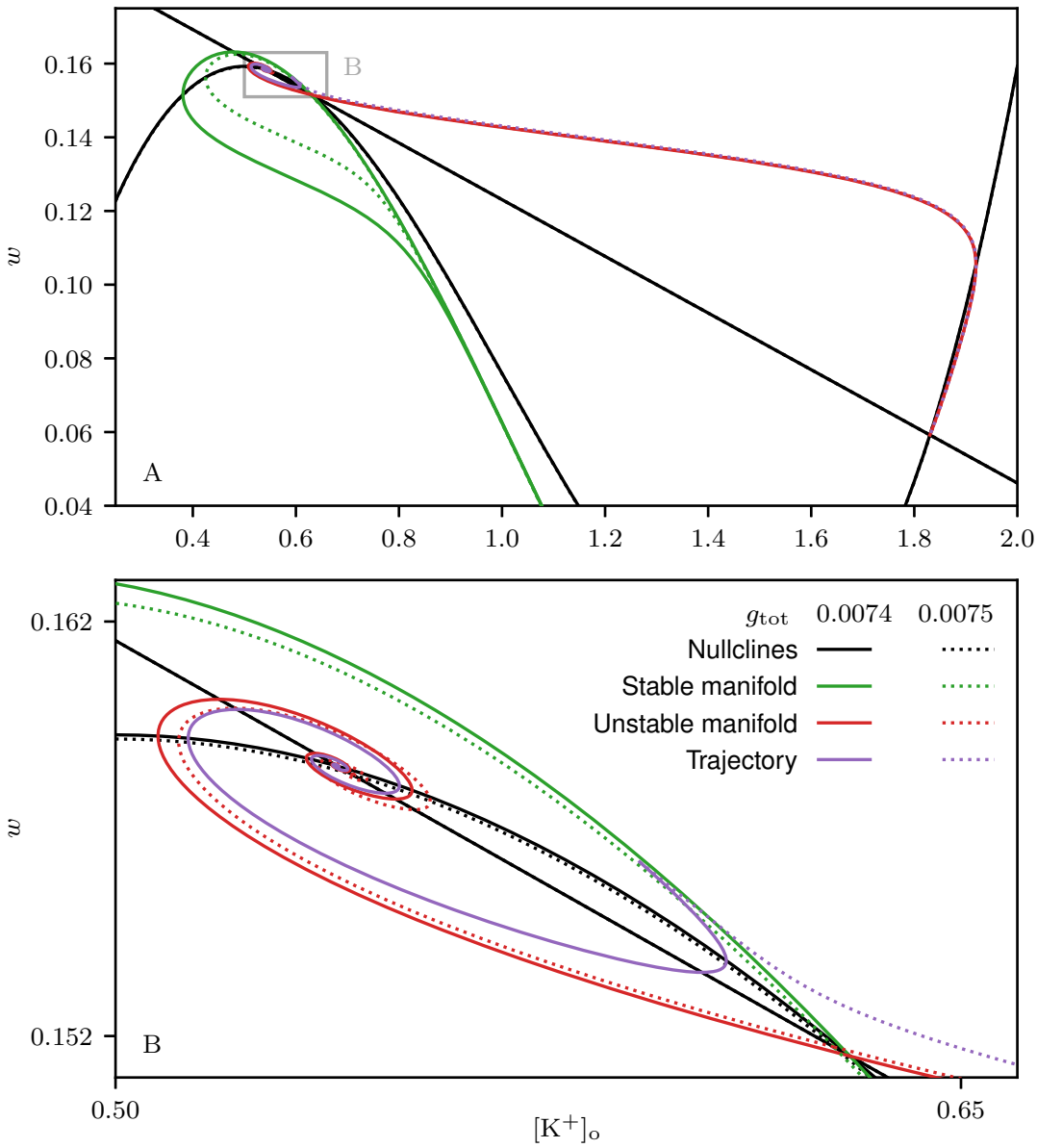


**Figure 4.6: Potassium dynamics in the phase plane.** Phase portrait of the slow block System (4.3) for two very close value $g_{tot}$ in the zone of bistability.

## 4.4 Fast layer problem

We consider now the fast layer problem, which is derived by taking the limit $\varepsilon \to 0$ in System (4.1):

$$\begin{aligned}
\frac{\mathrm{d}x_\mathrm{e}}{\mathrm{d}t} &= c_\mathrm{e}\left(x_\mathrm{e} - \frac{x_\mathrm{e}^3}{3} - y_\mathrm{e} + [\mathrm{K}]_\mathrm{o}^+ + I_\mathrm{ext} - I_\mathrm{GABA}(x_\mathrm{e}, x_\mathrm{i})\right) \\
\frac{\mathrm{d}y_\mathrm{e}}{\mathrm{d}t} &= \frac{x_\mathrm{e}^2 + dx_\mathrm{e} - by_\mathrm{e} + a}{c_\mathrm{e}} \\
\frac{\mathrm{d}x_\mathrm{i}}{\mathrm{d}t} &= c_\mathrm{i}\left(x_\mathrm{i} - \frac{x_\mathrm{i}^3}{3} - y_\mathrm{i} + [\mathrm{K}]_\mathrm{o}^+ + I_\mathrm{ext}\right) \\
\frac{\mathrm{d}y_\mathrm{i}}{\mathrm{d}t} &= \frac{x_\mathrm{i}^2 + dx_\mathrm{i} - by_\mathrm{i} + a}{c_\mathrm{i}}
\end{aligned} \tag{4.4}$$

We are interested in the dynamics of the two neurons, which are coupled through the inhibitory current $I_\mathrm{GABA}$, when the slow extracellular potassium $[\mathrm{K}]_\mathrm{o}^+$ is treated as a bifurcation parameter. We focus on the case where $I_\mathrm{ext} = 0.35$, which is the value of external input we use in the simulations of the full system in Section 4.5. We computed the bifurcation diagram with respect to $[\mathrm{K}]_\mathrm{o}^+$ for $c_\mathrm{i} = 3$, which correspond to the wild-type and migraine conditions (Fig. 4.7), and when $c_\mathrm{i}$ is reduced to 1.2, to model the epilepsy mutation (Fig. 4.8).

In both cases, the bifurcation structure of the 4-dimensional system is much richer than that of a single neuron (Section 4.2.2 and Section 4.2.6). We find additional limit cycle bifurcations, such as a torus bifurcation (Fig. 4.8 $\mathrm{A}_2$) and cascades of period-doubling bifurcations (Fig. 4.7 $\mathrm{A}_2$ - $\mathrm{A}_5$ and Fig. 4.8 $\mathrm{A}_2$) which suggest regions of chaos. There are also isolas of limit cycles (Fig. 4.8 $\mathrm{A}_2$), which often arise in multi-timescale systems displaying complex oscillations [116–118]. It is not possible to give a direct biological interpretation for each of those. The essential point is that the key features which we need to model $\mathrm{Na_V}1.1$ mutations are preserved from Fig. 4.4 $\mathrm{A}_1$ and Fig. 4.4 $\mathrm{A}_2$.

Note that the coupling between the two neurons is unidirectional: the pyramidal neuron has no influence on the GABAergic neuron (Fig. 4.2). The dynamics of $(x_\mathrm{i}, y_\mathrm{i})$ in the fast layer problem is thus exactly the same as in the two-dimensional case of Eq. (4.2).

### 4.4.1 Migraine *vs.* wild-type condition

In Fig. 4.7, for physiological concentrations of extracellular potassium (lower branch of equilibria in Fig. 4.5), the only stable objects are limit cycles of large amplitude, which correspond to tonic firing of the neurons. However, a too large rise of $[\mathrm{K}]_\mathrm{o}^+$ would provoke the transition to depolarization block of both neurons, the only attractor left being a stable equilibrium with high $x_{e,i}$ values. Compared to Fig. 4.4 $\mathrm{A}_1$, the inhibitory current $I_\mathrm{GABA}$ causes subthreshold oscillations of the pyramidal neuron, between the resting potential and tonic firing regimes. Interestingly, the period-doubling bifurcations allow for more complex spiking patterns, with subthreshold oscillations and varied spike shapes along a train of action potentials. This is consistent with simulations of the detailed model, see for example the voltage traces in Fig. 3.4 (Chapter 3).

### 4.4.2 Epilepsy condition

In the wild-type case (Fig. 4.7), the Hopf bifurcation which occurs at a high value of $[\mathrm{K}]_\mathrm{o}^+$ is in fact a double Hopf [119]: the two pairs of complex conjugated eigenvalues cross the imaginary axes of the complex plane at the same time. To model the epilepsy mutations,

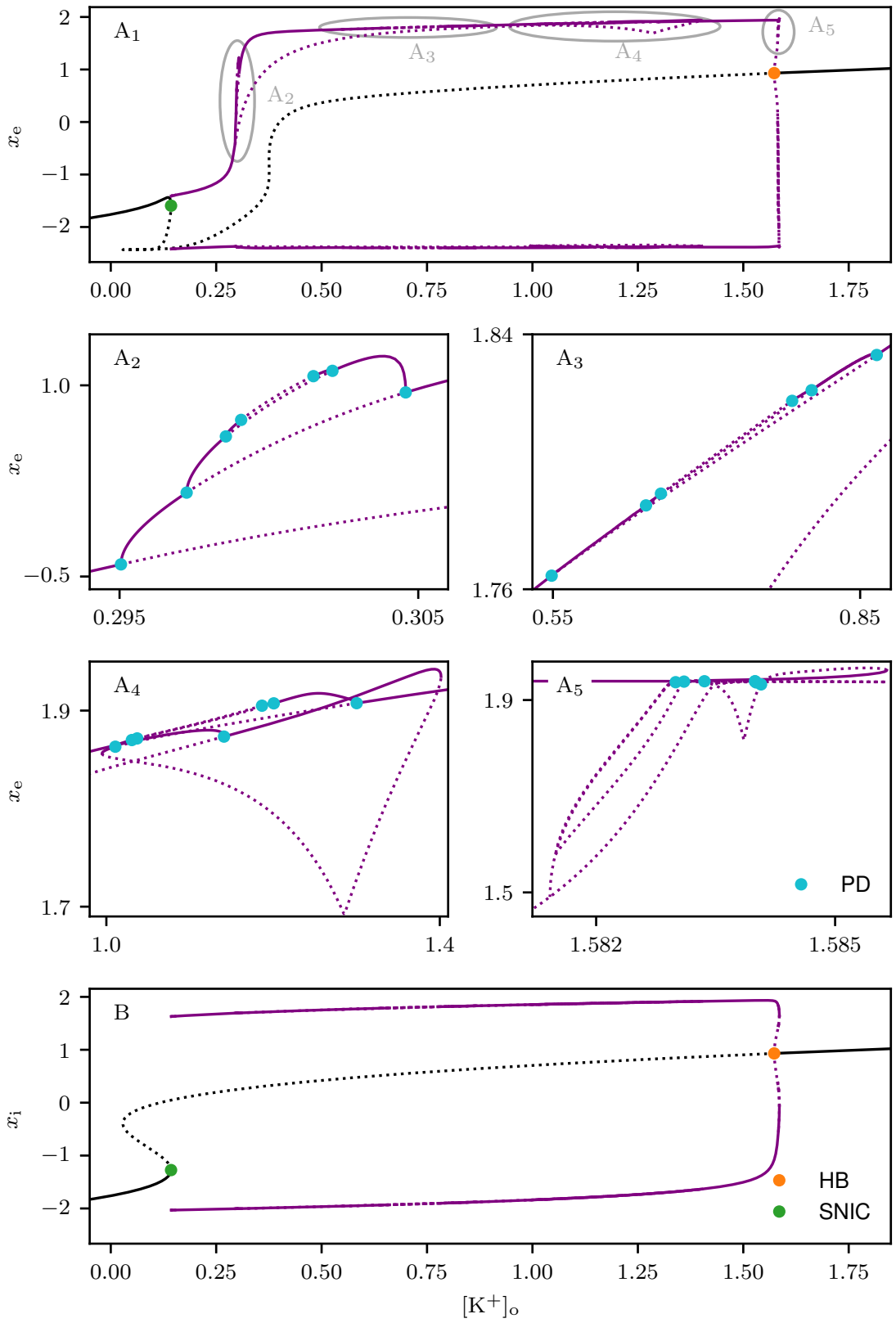


**Figure 4.7: Dynamics of the fast layer problem in the wild-type and migraine conditions.** Bifurcation diagram $x_e$ *vs.* $[K]_o^+$ (**A**) and $x_i$ *vs.* $[K]_o^+$ (**B**) of System (4.4) when $c_i = 3$, which corresponds to the wild-type and migraine conditions, for an external input $I_{ext} = 0.35$. **$A_2$ - $A_5$.** Zoom on the period-doubling (PD) bifurcations.

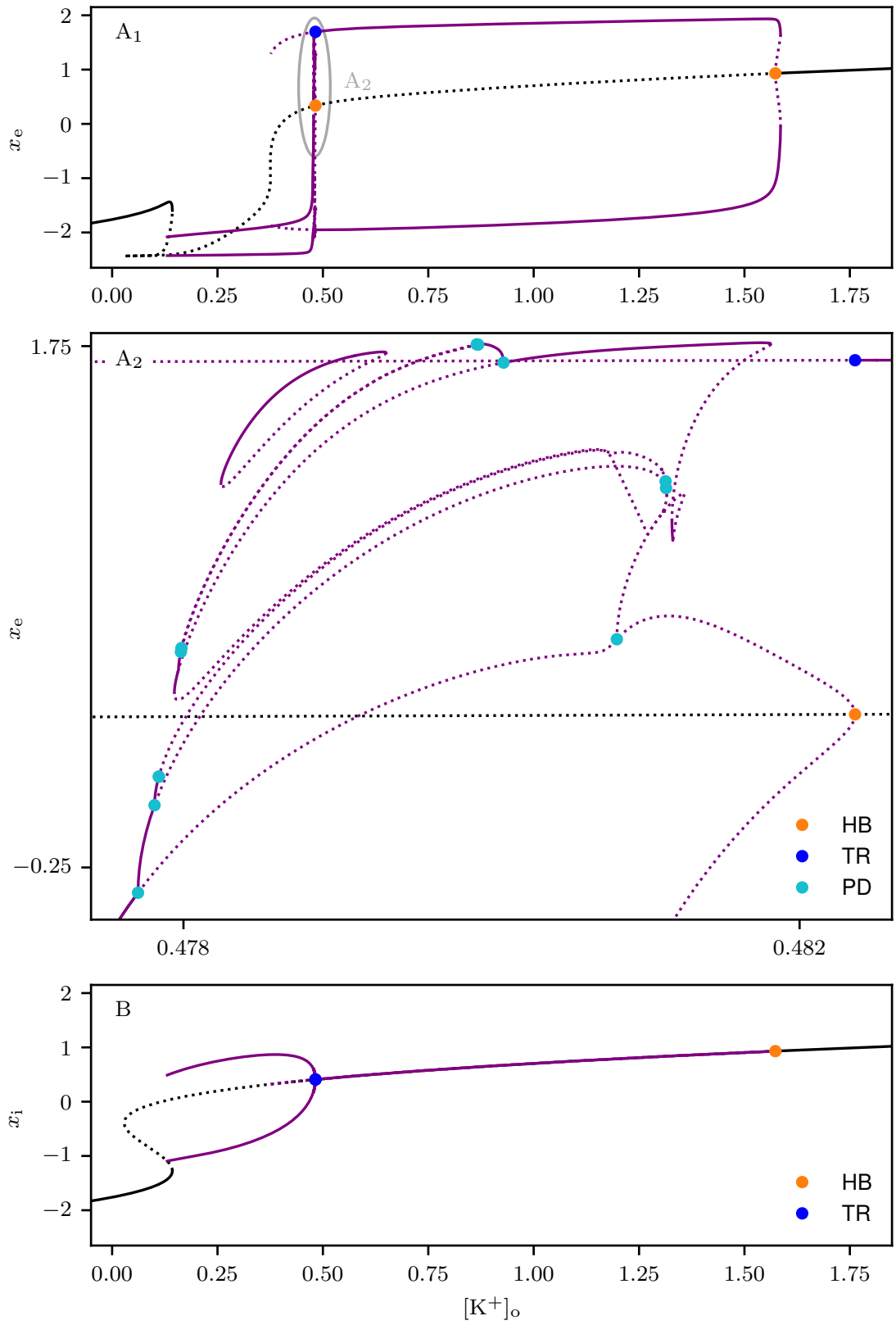


**Figure 4.8: Dynamics of the fast layer problem in the epilepsy condition.** Bifurcation diagram $x_e$ *vs.* $[K]_o^+$ (**A**) and $x_i$ *vs.* $[K]_o^+$ (**B**) of System (4.4) when $c_i = 1.2$, which corresponds to the epilepsy condition, for an external input $I_{ext} = 0.35$. TR: Torus bifurcation.

we decreased $c_i$ to 1.2 for the GABAergic neuron while keeping $c_i = 3$ for the pyramidal neuron. As a consequence, the double Hopf splits into two: $H_L$ at $[K]_o^+ = K_L \approx 0.482$ and $H_U$ at $[K]_o^+ = K_U \approx 1.573$ (Fig. 4.8). When crossing $H_L$ from $[K]_o^+ < K_L$ to $[K]_o^+ > K_L$, the real part of one of the pairs of eigenvalue becomes negative: the branch of unstable foci remains unstable but gains two stable directions. At $H_U$, the branch of equilibria stabilizes as the real part of the two other eigenvalues also becomes negative.

The bifurcation structure in the narrow region ($0.477 < [K]_o^+ < 0.483$) near $H_L$ is complicated (Fig. 4.8 $A_2$). $H_L$ gives rise to a branch of limit cycles and we found isolas, which we computed by continuation starting from stable complex solutions obtained by direct simulation. Both undergo cascades of period-doubling bifurcations. Before this narrow region ($[K]_o^+ < 0.477$), there is a branch of limit cycles which corresponds to subthreshold oscillations of the pyramidal neuron and firing of the GABAergic neuron. On the other side ($[K]_o^+ > 0.483$), there is a branch of stable limit cycles for which the pyramidal neuron spikes but the GABAergic neuron is at steady state.

In fact, we suspect that the torus bifurcation which stabilizes this branch of limit cycles occurs at the same value of $[K]_o^+$ as the Hopf bifurcation $H_L$. Without providing a rigorous proof, an important element appears to be the unilateral forcing from the GABAergic neuron to the pyramidal one. For $[K]_o^+ > K_L$, the $(x_i, y_i)$ component of the stable limit cycles is stationary, because the dynamics of the GABAergic neuron cannot be different than in the two-dimensional case. At $H_L$, limit cycles of small amplitude emerge, which are stable for $(x_i, y_i)$. When the forcing $I_{GABA}$ onto the pyramidal neuron becomes periodic, it must cause a qualitative change to the relaxation cycles of $(x_e, y_e)$, which is compatible with a torus bifurcation.

What interests us in this bifurcation structure is the possibility of depolarization block of the GABAergic neuron for low concentrations of potassium, when the external input is strong enough (here $I_{ext} = 0.35$). It was not the case in the wild-type condition (Fig. 4.7). As we mentioned before, the dynamics of $(x_i, y_i)$ in the fast layer problem is unchanged compared to Eq. (4.2). The enhanced susceptibility of the GABAergic neuron to depolarization block is thus achieved here in exactly the same way as in the two-dimensional system (Fig. 4.4), namely by shifting the Hopf bifurcation for the GABAergic neuron to lower values of potassium or external inputs (Fig. 4.4).

## 4.5 Full system

Finally, we examine the dynamics of the full system (4.1). We compare the configurations: wild-type, migraine and epileptogenic mutation of $Na_V1.1$ (see Section 4.2.6). Fig. 4.9 shows trajectories of the system in the three cases, when the neurons are stimulated with an external input $I_{ext} = 0.35$. To understand how the different responses are produced, we look at the superimposition of the full system's trajectories onto the bifurcation diagram of the fast layer problem with respect to $[K]_o^+$. This procedure of slow-fast dissection is a classical tool to study multiple-timescale systems and was introduced by J. Rinzel, see for instance [91].

### 4.5.1 The route to CSD initiation

In the absence of mutation, extracellular potassium remains at low concentrations, for which the neurons are in a firing regime (Fig. 4.9 A, Fig. 4.10).

With the migraine mutations, neuronal activity releases by construction more potassium (Fig. 4.9 $B_5$ *vs.* Fig. 4.9 $A_5$). It accumulates progressively, until a "tipping point" is reached, resulting in an abrupt transition to the high state (Fig. 4.9 $B_3$) with a slight overshoot. This progression is consistent with what is measured experimentally (Fig. 4.1). As

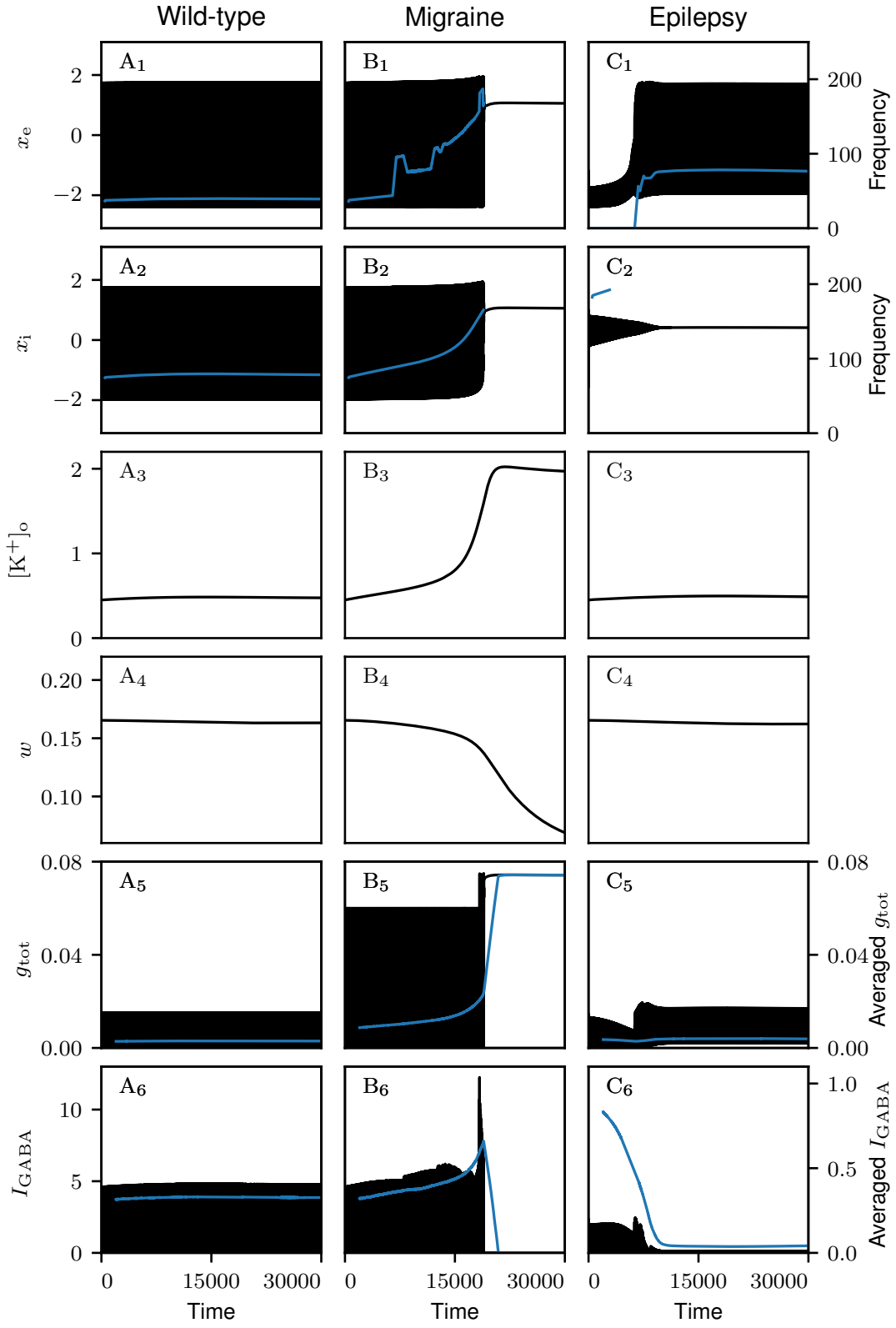


**Figure 4.9: Trajectories of the full system (4.1).** Time traces for an external input $I_{\text{ext}} = 0.35$, taking as initial condition the steady state when $I_{\text{ext}} = 0$. We represented in blue the firing frequency of the neurons averaged on a sliding window of 500 time units. In the last two rows, we plotted the contribution $g_{\text{tot}}$ of neuronal spiking to the extracellular potassium and the inhibitory current $I_{\text{GABA}}$ (black curves), together with their average on a sliding window of 2000 time units (blue curves). **A.** Wild type condition: default parameter values. **B.** Migraine condition: $p = 4$. **C.** Epilepsy condition: $c_i = 1.2$.

$[K]_o^+$ increases, the voltage traces show a good agreement with the bifurcation diagram of the fast layer problem (Fig. 4.11). Meanwhile, the firing frequency of the neurons increases considerably (Fig. 4.9 $B_1, B_2$), similarly to simulations of the detailed model (Fig. 3.5 E, F) and experiments (Fig. 3.5 A, B). Note that the frequency of the limit cycles in Fig. 4.10 is not necessarily the firing frequency: there can be more that one full blown action potential per period, due to period-doubling bifurcations. The switch from the spiking regime to depolarization block of the two neurons, which indicates CSD initiation, is achieved via a *dynamic bifurcation* of limit cycles. It is unclear which is the precise bifurcation responsible for this transition, since there are several branches of limit cycles in this region (Fig. 4.7 $A_5$) and $[K]_o^+$ is undergoing a relatively fast increase. The key point is that $[K]_o^+$ reaches values for which the depolarized steady state is the only attractor.

We took a closer look at the threshold between the physiological and pathological responses. In Fig. 4.12, two very close values of $p$ lead to either regular spiking or depolarization block of the neurons. We can see in the inset of Fig. 4.12 A the critical moment where the two potassium traces separate (blue and orange curves). While $[K]_o^+$ builds up, the contribution $g_{\text{tot}}$ of neuronal firing to $[K]_o^+$ increases as well, which creates a positive feedback loop. In the slow block $g_{\text{tot}}$ is a parameter, but in the full system $g_{\text{tot}}$ is equal to $pg(x_i) + g(x_e)$, which is not a slow varying quantity. However, remarkably, when projected onto the $([K]_o^+, w)$ plane, the trajectories of the full system resemble the ones of the slow block shown in Fig. 4.6 B (purple curves). Even though $g_{\text{tot}}$ oscillates rapidly, our numerical results suggest that its mean can be regarded as a slow quantity (Fig. 4.12 B), which can bring the system on the other side of some excitability threshold for the potassium block. In the case where $g_{\text{tot}}$ is a parameter, this threshold is the stable manifold of the saddle.

### 4.5.2 The route to pre-epileptic hyperactivity

With the epileptogenic mutations, the system first follows the branch of limit cycles for which the pyramidal neuron produces subthreshold oscillations while the amplitude of the GABAergic neuron's action potentials diminishes (Fig. 4.13). Shortly after surpassing the low Hopf bifurcation $H_L$, the GABAergic neuron enters depolarization block, with a delay due to the speed of $[K]_o^+$. This causes a drop of the inhibitory current (Fig. 4.9 $C_2, C_6$). Consequently, the pyramidal neuron starts spiking at high frequency compared to the wild-type case (Fig. 4.13 $C_1$ *vs.* Fig. 4.13 $A_1$), which we interpret as pre-epileptic hyperactivity. The limit firing frequency is almost twice as high as for the wild-type case (Fig. 4.10 B *vs.* Fig. 4.13 B). In those particular cases, the frequency of the limit cycles corresponds to the firing frequency, since only one action potential is emitted per period.

What exactly happens at the transition between the two phases for the pyramidal neuron is not straightforward, as the bifurcation landscape is very intricate (Fig. 4.8 $A_2$). One way to address this would be to study the dynamics closer to the singular limit by reducing $\varepsilon$ and observing which branches play a role for the full dynamics.

## 4.6 Discussion

In this chapter, we have designed and analyzed a reduced version of our biophysical model (Chapter 3) of CSD initiation and epileptiform hyperactivity. We constructed this six-dimensional system to mirror the microcircuit structure of the detailed model. Namely, we considered two coupled idealized neurons, a pyramidal cell and a GABAergic neuron that inhibits it, and additional variables to model the dynamics of extracellular potassium, which is the most relevant ion concentration in this context. Albeit phenomenological in spirit, with mostly polynomial terms and mathematical excitable models for its

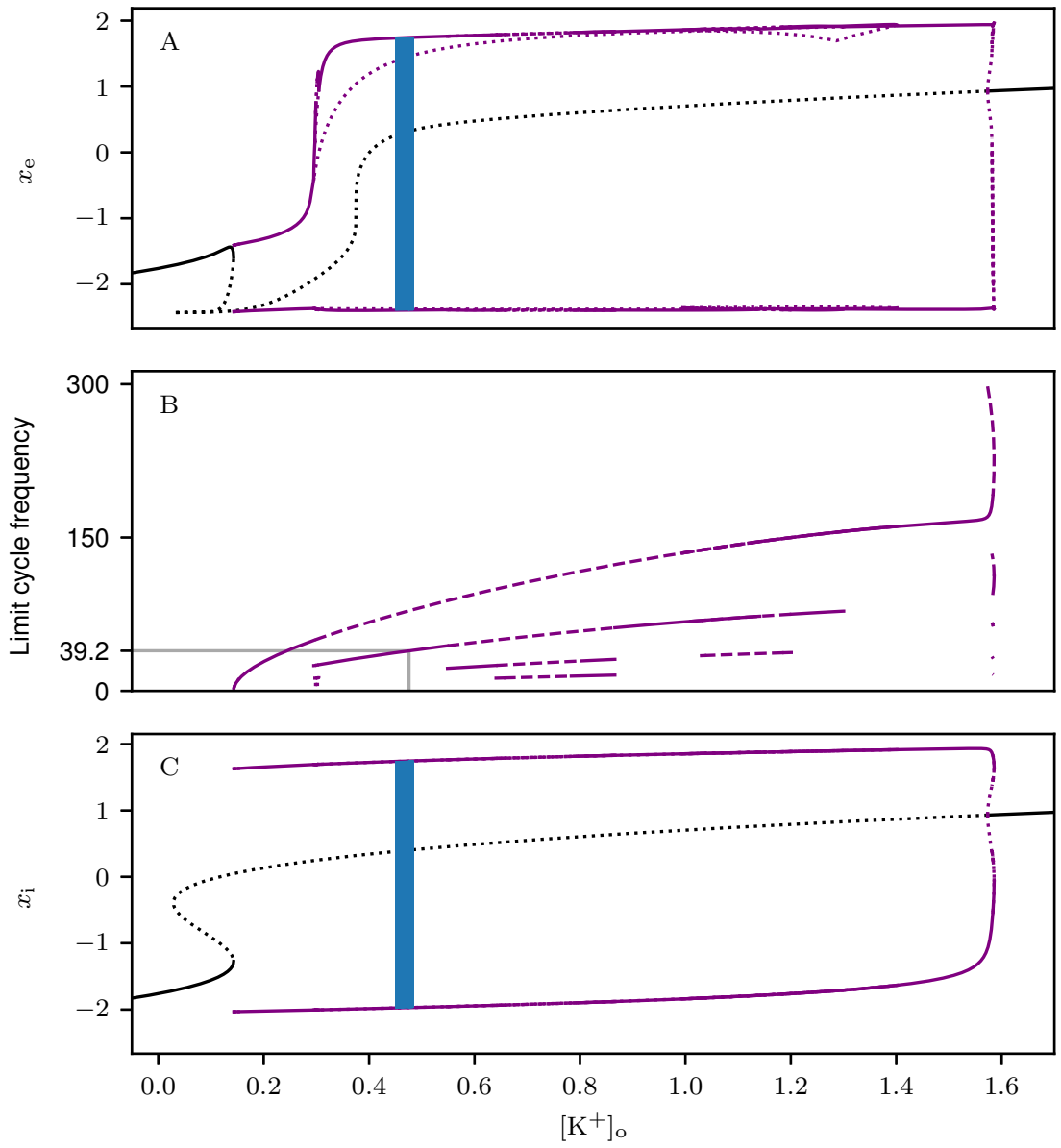


**Figure 4.10: Wild-type condition: tonic firing of the neurons.** We superimposed the trajectories of the full system shown in Fig. 4.9 A onto the bifurcation diagram of the fast layer problem (4.4) for $c_i = 3$. **A.** Voltage of the pyramidal neuron $x_e$ *vs.* $[K]_o^+$. **B.** Voltage of the GABAergic neuron $x_i$ *vs.* $[K]_o^+$. **C.** Frequency of the limit cycles. We marked in gray the final $[K]_o^+$ value of the full system trajectory.

three blocks — 2D Hindmarsh-Rose (HR) type model for each neuron, FitzHugh–Nagumo (FHN) type model for the potassium —, this reduced model still retains salient features of the biophysical model, in the form of the inhibitory synaptic current and the function governing potassium release. In this simpler setting, we managed to reproduce both pathological transitions upon minimal parameter variation: one parameter for each scenario. We exploited the minimal structure of the model, as well as its explicit timescales, to identify dynamical mechanisms underpinning the two pathological transitions.

One important novelty of our model is the possibility to capture the abrupt increase of extracellular potassium in the CSD scenario, with an overshoot at the beginning of the depolarization block (DB) phase. To this end, we introduced a third timescale and

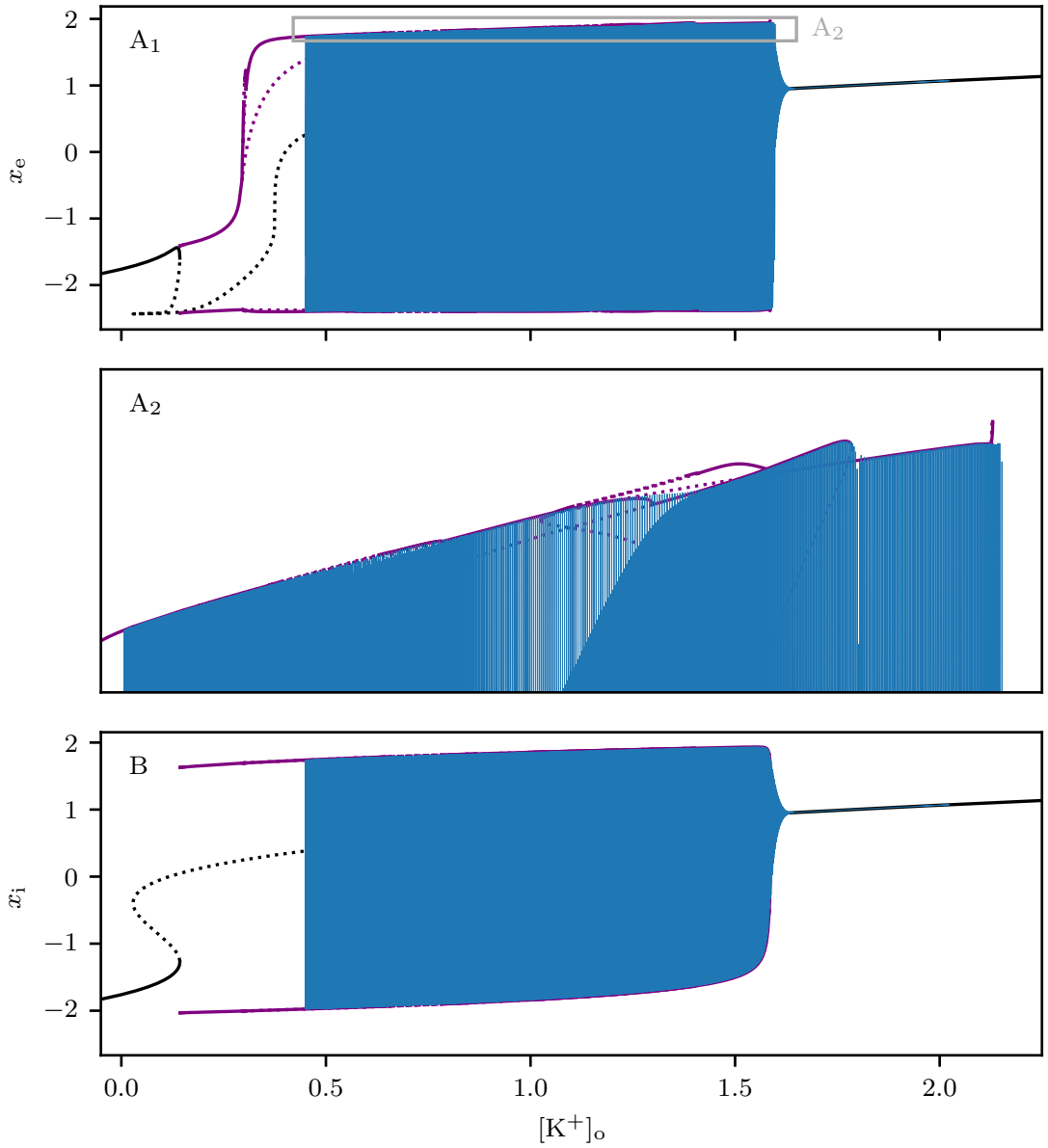


**Figure 4.11: Migraine condition: depolarization block of the two neurons.** We superimposed the trajectories of the full system shown in Fig. 4.9 B onto the bifurcation diagram of the fast layer problem (4.4) for $c_i = 3$. **A.** Voltage of the pyramidal neuron $x_e$ *vs.* $[K]_o^+$. **B.** Voltage of the GABAergic neuron $x_i$ *vs.* $[K]_o^+$.

hence modeled the potassium dynamics with two variables, inspiring from [105]. With this approach the potassium block is a bistable slow-fast system, whose unstable (saddle) equilibrium organizes the transition to DB via its stable manifold. As we indicated in Section 4.3, getting rid of the third timescale maintains the sharp transition to the high potassium state, but without the overshoot observed in the experimental data acquired by our partner lab. We showed that analyzing the planar potassium system, in particular the dependence of the stable separatrix of the saddle upon constant forcing (instead of feedback from the neurons), is enough to grasp the mechanism of CSD initiation in the full system. We did not provide a mathematical justification for this procedure, which is based on the averaging of the neuronal feedback terms; it could be the subject of future work.

In the case of $Na_V1.1$ epileptogenic mutations, we have shown that the main ingredient is a shift in the position of a Hopf bifurcation in the fast layer problem, obtained by continuing in two parametric dimensions the corresponding Hopf in the GABAergic neuron model. By varying one parameter in the full system, we reproduce the hypothesized biophysical mechanism: the GABAergic neuron enters DB at low potassium level when the stimulation is strong enough, hence ceasing to inhibit, which induces an increase of the pyramidal neuron's firing frequency.

Overall, this model is very similar in terms of its dynamical behavior to the much larger and nonlinear biophysical model developed and studied in Chapter 3. An interesting avenue for future work would be to exploit the results reported in this chapter to better understand the biophysical model and possibly improve it.

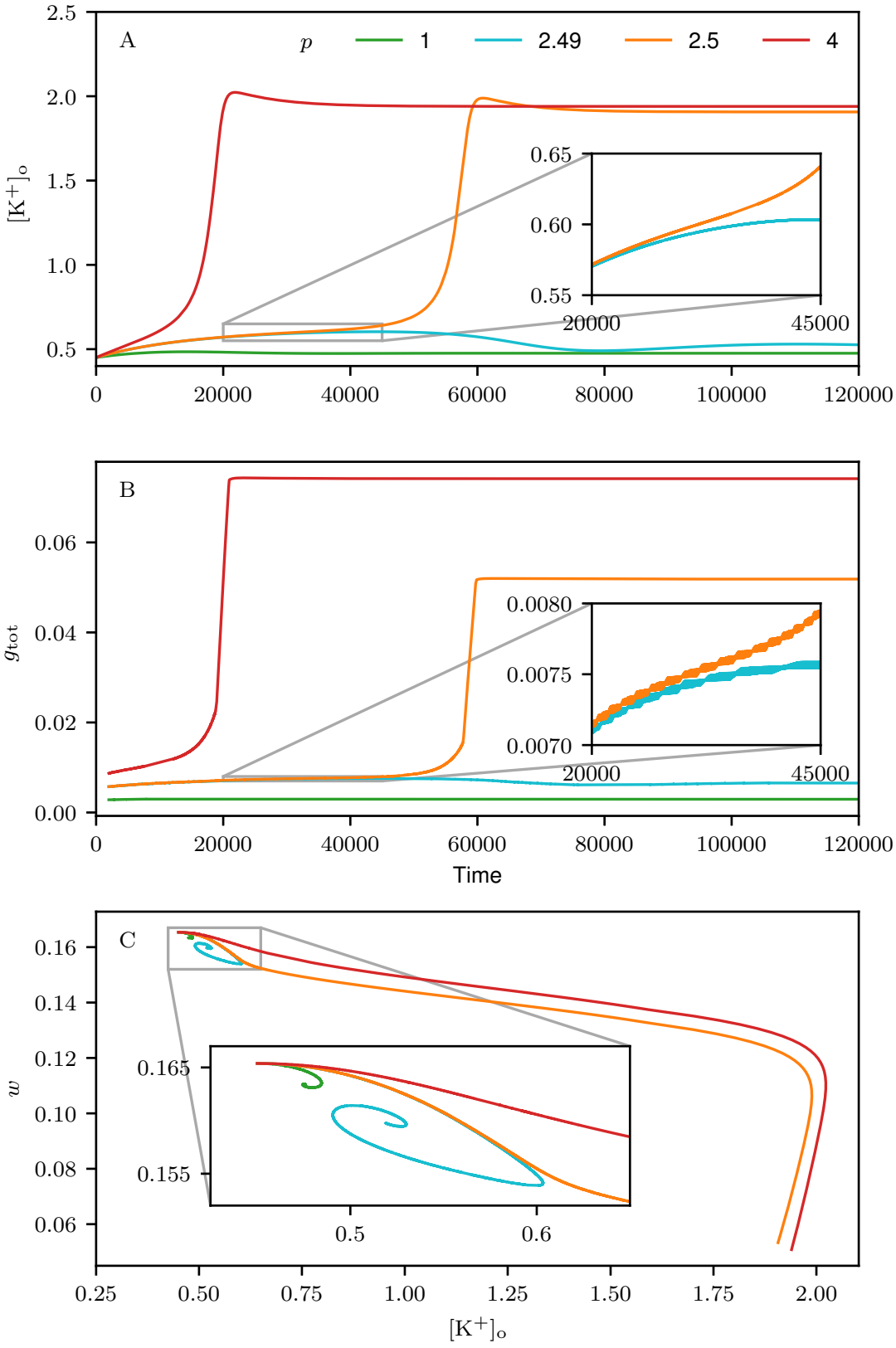


**Figure 4.12: Activity-mediated jump of the extracellular potassium to the pathological elevated concentration.** Simulations of the full system (4.1) for an external input $I_{ext} = 0.35$ and for different values of the parameter $p$, which controls the release of potassium by the GABAergic neuron. **A.** Extracellular potassium. **B.** Total contribution of neuronal firing to the extracellular potassium, averaged on a sliding window of 2000 time units. **C.** Projection onto the $([K]_o^+, w)$ plane.

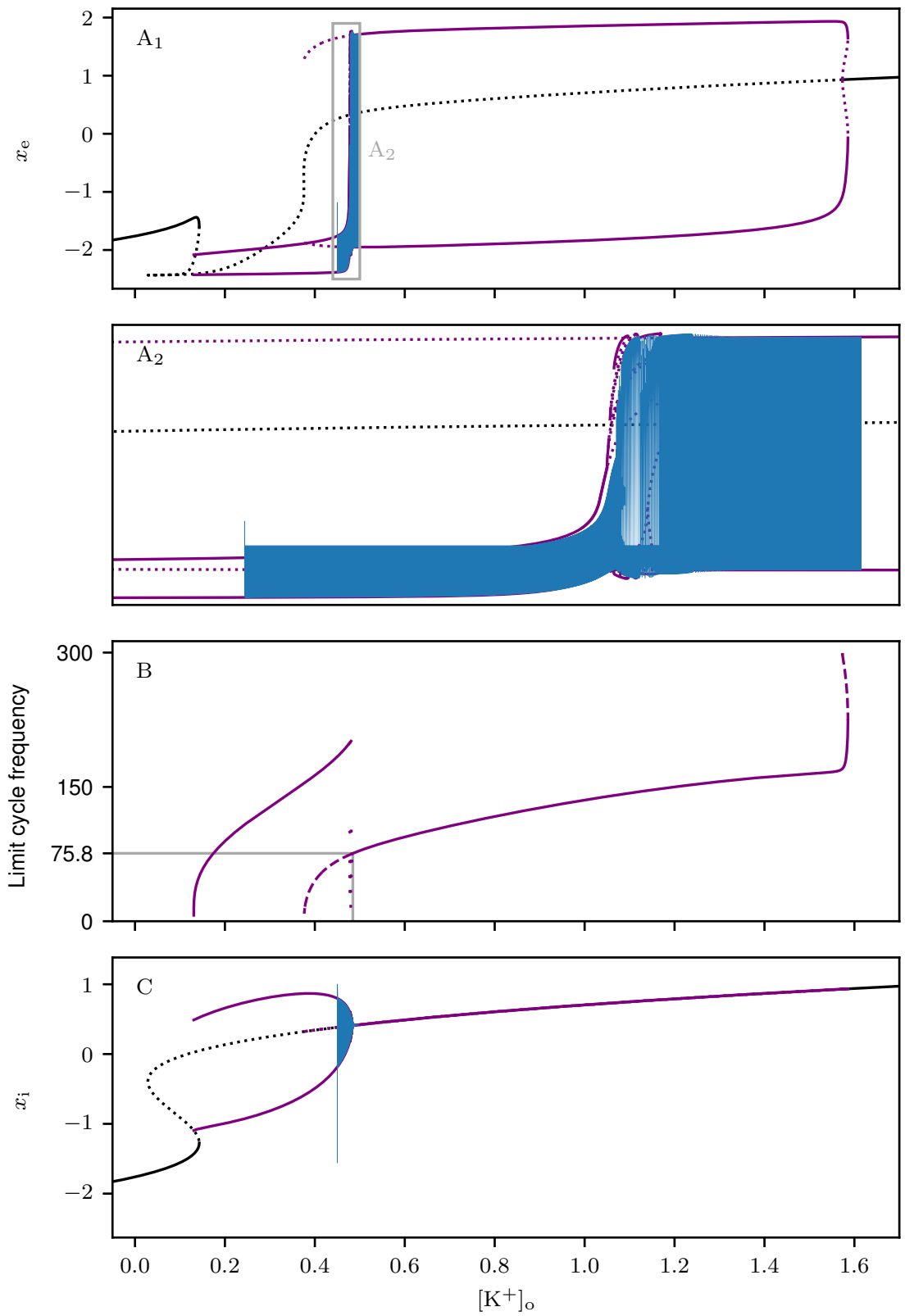


**Figure 4.13: Epilepsy condition: depolarization block of the GABAergic neuron and high firing frequency of the pyramidal neuron.** We superimposed the trajectories of the full system shown in Fig. 4.9 C onto the bifurcation diagram of the fast layer problem (4.4) for $c_i = 1.2$. **A.** Voltage of the pyramidal neuron $x_e$ *vs.* $[K]_o^+$. **B.** Frequency of the limit cycles. We marked in gray the final $[K]_o^+$ value of the full system trajectory. **C.** Voltage of the GABAergic neuron $x_i$ *vs.* $[K]_o^+$.

# Chapter 5

# Conclusion

For both hemiplegic migraine and epileptogenic mutations of $Na_V1.1$, our results suggest the involvement of mechanisms of network hyperexcitability other than the modification of the firing frequency of GABAergic neurons. This is noteworthy, because modifications of firing frequency is one of the principal features investigated in pathologies of neuronal excitability.

## 5.1 $Na_V1.1$ migraine mutations

In Chapter 2, using experimental evidence based on the acute activation of $Na_V1.1$ channels with a toxin and on the optogenetic hyperactivation of GABAergic neurons, we disclosed a mechanism of CSD initiation caused by FHM3 mutations. Notably, this mechanism seems to be specific to the neocortex. Contrary to what has been reported for the other types of familial hemiplegic migraine (FHM1 and FHM2), it does not involve synaptic transmission. Instead, our data show that the **key factor for CSD initiation** in this case is a **spiking-generated build-up of extracellular potassium**. Those results are consistent with the recent paper by Auffenberg et al. [39], where the authors developed and studied a knock-in mouse model of FHM3. Migraine etiology is multifactorial, with probably numerous different mechanisms [16]; the mechanism of CSD initiation that we described may be implicated in other types of migraine and possibly in other pathologies in which SDs are involved (e.g. stroke, traumatic brain injury, and subarachnoid hemorrhage) [13], because it could be associated not only to $Na_V1.1$ mutations, but also to other dysfunctions that lead to GABAergic neurons' hyperactivity.

According to our modeling results from Chapters 2 and 3, it is not clear whether or not the spiking-induced accumulation of extracellular potassium which causes CSD is due to an increased firing frequency of the GABAergic neurons.

In Chapter 2, the model was still in a preliminary state and covered only the migraine mutations of $Na_V1.1$. Based on the experimental input-output relationship in Fig. 2.2 B, we expected persistent sodium current to cause an increase of the firing frequency of the GABAergic neuron. It was at first not the case, and this behavior is not specific to our model: Dahlem et al. reported reduced firing frequency when implementing FHM3 in an Hodgkin-Huxley model with dynamic ion concentrations [94]. To obtain an effect similar to the one in Fig. 2.2 B in our model, we introduced a shift of the voltage dependence of the activation when modeling persistent sodium current (see Section 3.2.2). This can be justified, see e.g. [87, 88].

In Chapter 3, to obtain both migraine and epilepsy scenarios within the same framework, we adapted the set of parameter values, see Table 3.3. We realized that, in this model, even when the shift of the activation $v_{\text{shift,P}}$ was such that persistent sodium current barely affects the firing frequency of the GABAergic neuron (Fig. 3.2 A), CSD initiation is still facilitated (see Figs. 3.4 to 3.6) due to the accumulation of extracellular potassium.

We found it interesting and decided to explore this route. Moreover, as discussed in Section 3.4.1, there are many types of GABAergic neurons and it appears that not all of them react to persistent sodium current in the same manner: in some cases the firing frequency is unchanged [39, 47]. To conclude, we can say that, **at least in our model, the initial progressive accumulation of extracellular potassium leading to CSD initiation does not require an increased firing frequency of the GABAergic neuron.**

## 5.2 $Na_V1.1$ epileptogenic mutations

In simulations of the detailed biophysical model in Chapter 3, **reduced sodium conductance results in an enhanced susceptibility of GABAergic neurons to depolarization block**, i.e. it is induced by smaller inputs. This prediction is confirmed experimentally by recordings on *Scn1a*$^{+/-}$ mice. Based on those results, we propose that depolarization block of GABAergic neurons is a pro-epileptic mechanism involved in the triggering of seizures in carriers of $Na_V1.1$ loss of function mutations, because it causes the dysfunction of network inhibition, which is an ideal background for the genesis of seizures. To determine whether this hypothesis is reasonable, at least two points need to be examined: (1) In which regions of the neurons is $Na_V1.1$ expressed? (2) Can DB of GABAergic neurons be responsible for a collapse of the inhibition?

The consequences of the first aspect cannot be investigated within the modeling framework presented here, since we only consider point neurons. It is however a relevant question: in the case of a mostly somatic expression for example, the effect of $Na_V1.1$ loss of function on GABAergic inhibition is unclear. $Na_V1.1$ was first described as having a somato-dendritic expression throughout the brain [120–122]. However, since then, $Na_V1.1$ expression was also observed in nodes of Ranvier and axon initial segment (AIS) in multiple brain areas of adult [123] and developing [23] mice. In fact, Ogiwara et al. showed that $Na_V1.1$ is clustered predominantly at the axon initial segments of parvalbumin-positive (PV+) interneurons [23], a subclass of GABAergic neurons which plays a central role in the inhibitory restraint of epileptiform events [99].

Concerning the second aspect, both in Chapter 3 and in Chapter 4 the absence of synaptic inhibition during depolarization block of the GABAegic neuron was an assumption of the model. Experimentally, even though the answer seems rather negative, it is still subject of discussion whether neurons release synaptic vesicles during depolarization block [124]. However, in a recent experimental paper, Călin et al. used an optogenetic strategy to test if depolarization block in PV+ interneurons is a significant factor for the loss of inhibitory restraint [125]. Consistently with our hypothesis, they conclude that **depolarization block is a point of weakness of the synaptic inhibition and represents a target for preventing the initiation and spread of seizure activity**.

## 5.3 Perspectives: accuracy *vs.* simplicity

Further projects could go in two opposite directions. We could improve the biological accuracy of the model, at the cost of making it even more complex. On the contrary, the simplification of the model performed in Chapter 4 could be taken further, facilitating a more advanced mathematical analysis. With a very basic model, we could also consider more than two neurons: this would allow us to take into account network effects involved in the initiation of CSDs and seizures or even to study the propagation of these phenomena.

### 5.3.1 Towards more realistic models

In this work, we omitted aspects which might play an important role in the pathological mechanisms of $Na_V1.1$ mutations. Even though astrocytes are essential in maintaining ion homeostasis [126], our modeling of their buffering function is oversimplified (Section 3.2.2.4). This could be improved, using for example the framework developed in [75]. Another element that we did not consider is cell swelling [127], which is caused by osmotic forces when transmembrane concentration gradients change. For simplicity, we assumed the volume of the neurons to be constant. To include volume dynamics into the model, one could take as a basis the formalism of [128].

One way to increase the level of biological precision while keeping the model tractable would be to focus only on $Na_V1.1$ channels instead of modeling complete neurons with all their transporters. A possible future work could be to model the different states of the channels (open, close, inactivated) as Markov states like in [129], to investigate in detail the effect of $Na_V1.1$ FHM3 mutations on the gating dynamics.

### 5.3.2 Towards simpler models

#### 5.3.2.1 Extracellular potassium dynamics

Extracellular potassium is crucial for CSD initiation. The modeling of its dynamics in Chapter 4 is already phenomenological (Section 4.2.4). To simplify it further, we could choose to use only one equation instead of a two-dimensional system. The minimal set up which we need is two stable steady states separated by a threshold. It could be achieved with an equation such as:

$$\frac{\mathrm{d}[\mathrm{K}]_\mathrm{o}^+}{\mathrm{d}t} = (\mathrm{K}_1 - [\mathrm{K}]_\mathrm{o}^+)([\mathrm{K}]_\mathrm{o}^+ - \mathrm{K}_2)([\mathrm{K}]_\mathrm{o}^+ - \mathrm{K}_3), \quad 0 < \mathrm{K}_1 < \mathrm{K}_2 < \mathrm{K}_3.$$

The stable equilibrium $K_1$ corresponds to a physiological level of potassium. An increase above the unstable equilibrium $K_2$, chosen closer to $K_1$ than to $K_3$, would cause a jump to the pathological stable equilibrium $K_3$. The analogous of $K_2$ in Chapter 4 is the stable manifold of the saddle (Fig. 4.6), which delimits the bassins of attractions of the two stable steady states.

One drawback of this approach is that $[\mathrm{K}]_\mathrm{o}^+$ cannot oscillate, preventing the trajectory to the high state to exhibit an overshoot. With this simplification, we would also lose the biological interpretation related to the slow buffering of extracellular ions of the two-dimensional slow-fast framework [105].

#### 5.3.2.2 Neuronal dynamics

Transition to depolarization block is at the center of the pathophysiology of migraine with aura, and our work suggests that it might also be involved in the onset of seizures. As they are, computationally inexpensive models such as the theta model [130] cannot reproduce this pathological behavior. An interesting project would be to extend one of those simple models such that the neuron enters depolarization block when excessively stimulated. The motivation behind it is to build networks.

In the theta neuron, the transition from quiescence to repetitive firing occurs at a SNIC. For the extension mentioned above, we would need an additional bifurcation to mediate the transition from repetitive firing to depolarization block. The following example illustrates this idea:

$$\frac{\mathrm{d}\theta}{\mathrm{d}t} = (I - \cos\theta)(\cos\theta + I_\mathrm{DB} + 1 - I), \quad \theta \in S^1. \tag{5.1}$$

A branch of stable limit cycles emerges through a SNIC at $I = 1$ and terminates at another SNIC at $I = I_{\mathrm{DB}}$. If we define the voltage $v = \sin(\theta)$, the branch of stable equilibria created by the second SNIC corresponds to higher voltage values than the subthreshold branch (Fig. 5.1).

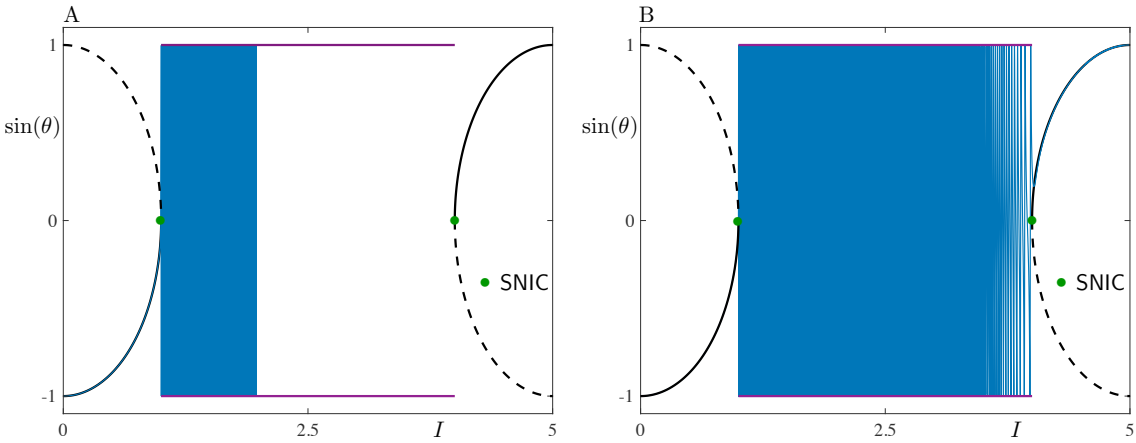


**Figure 5.1: Depolarization block in a phase oscillator model.** Bifurcation diagram $\sin(\theta)$ *vs.* $I$ of Eq. (5.1) and superposition of trajectories when $I$ slowly increases from 0 to 1.97 (**A**) or to 5 (**B**).

In a framework similar to Eq. (5.1), if extracellular potassium participates to the input $I$, a too large accumulation of this ion would cause depolarization block of the neuron (Fig. 5.1 B), reproducing the mechanism of CSD initiation and possibly CSD propagation. To model the epilepsy condition, one could reduce the input value at which the transition to DB occurs (here controlled by the parameter $I_{\mathrm{DB}}$). Having a SNIC as spike-terminating bifurcation is not ideal: it means that the firing frequency tends to zero when converging to it. This is however not too problematic in the case of CSD, since the potassium input would not grow linearly, but instead rise relatively fast across the SNIC.

# Bibliography


[1] M. Mantegazza and V. Broccoli. "SCN1A/NaV1.1 Channelopathies: Mechanisms in Expression Systems, Animal Models, and Human iPSC Models". *Epilepsia* 60.S3 (2019), S25–S38.

[2] M. Mantegazza, S. Cestèle, and W. A. Catterall. "Sodium Channelopathies of Skeletal Muscle and Brain". *Physiological Reviews* 101.4 (Oct. 1, 2021), pp. 1633–1689.

[3] M. Dichgans et al. "Mutation in the Neuronal Voltage-Gated Sodium Channel *SCN1A* in Familial Hemiplegic Migraine". *The Lancet* 366.9483 (July 30, 2005), pp. 371–377.

[4] K. M. Kahlig et al. "Divergent Sodium Channel Defects in Familial Hemiplegic Migraine". *Proceedings of the National Academy of Sciences* 105.28 (2008), pp. 9799–9804.

[5] S. Bertelli et al. "Gain of Function of Sporadic/Familial Hemiplegic Migraine-Causing *SCN1A* Mutations: Use of an Optimized cDNA". *Cephalalgia* 39.4 (Apr. 1, 2019), pp. 477–488.

[6] S. Cestèle et al. "Nonfunctional $Na_V1.1$ Familial Hemiplegic Migraine Mutant Transformed into Gain of Function by Partial Rescue of Folding Defects". *Proceedings of the National Academy of Sciences* 110.43 (Oct. 22, 2013), pp. 17546–17551.

[7] S. Cestèle et al. "Self-Limited Hyperexcitability: Functional Effect of a Familial Hemiplegic Migraine Mutation of the $Na_V1.1$ (*SCN1A*) $Na^+$ Channel". *Journal of Neuroscience* 28.29 (July 16, 2008), pp. 7273–7283.

[8] S. Dhifallah et al. "Gain of Function for the *SCN1A*/$hNa_V1.1$-L1670W Mutation Responsible for Familial Hemiplegic Migraine". *Frontiers in molecular neuroscience* 11 (2018), p. 232.

[9] D. Pietrobon and M. A. Moskowitz. "Chaos and Commotion in the Wake of Cortical Spreading Depression and Spreading Depolarizations". *Nature Reviews Neuroscience* 15.6 (6 June 2014), pp. 379–393.

[10] A. A. P. Leao. "Spreading Depression of Activity in the Cerebral Cortex". *Journal of Neurophysiology* 7.6 (Nov. 1, 1944), pp. 359–390.

[11] M. Lauritzen. "Pathophysiology of the Migraine Aura: The Spreading Depression Theory". *Brain : a journal of neurology* 117.1 (1994), pp. 199–210.

[12] M. Mantegazza and S. Cestèle. "Pathophysiological Mechanisms of Migraine and Epilepsy: Similarities and Differences". *Neuroscience Letters*. Epilepsy: Advances in Genetics and Pathophysiology 667 (Feb. 22, 2018), pp. 92–102.

[13] J. P. Dreier and C. Reiffurth. "The Stroke-Migraine Depolarization Continuum". *Neuron* 86.4 (May 20, 2015), pp. 902–922.

[14] J. P. Dreier et al. "Recording, Analysis, and Interpretation of Spreading Depolarizations in Neurointensive Care: Review and Recommendations of the COSBID Research Group". *Journal of Cerebral Blood Flow & Metabolism* 37.5 (May 2017), pp. 1595–1625.

[15] S. Major et al. "Direct Electrophysiological Evidence That Spreading Depolarization-Induced Spreading Depression Is the Pathophysiological Correlate of the Migraine Aura and a Review of the Spreading Depolarization Continuum of Acute Neuronal Mass Injury". *GeroScience* 42.1 (Feb. 1, 2020), pp. 57–80.

[16] M. D. Ferrari et al. "Migraine Pathophysiology: Lessons from Mouse Models and Human Genetics". *The Lancet Neurology* 14.1 (Jan. 1, 2015), pp. 65–80.

[17] N. A. Jansen et al. "First FHM3 Mouse Model Shows Spontaneous Cortical Spreading Depolarizations". *Annals of Clinical and Translational Neurology* 7.1 (2020), pp. 132–138.

[18] A. M. J. M. van den Maagdenberg et al. "A Cacna1a Knockin Migraine Mouse Model with Increased Susceptibility to Cortical Spreading Depression". *Neuron* 41.5 (Mar. 4, 2004), pp. 701–710.

[19] L. Leo et al. "Increased Susceptibility to Cortical Spreading Depression in the Mouse Model of Familial Hemiplegic Migraine Type 2". *PLOS Genetics* 7.6 (June 23, 2011), e1002129.

[20] L. Claes et al. "De Novo Mutations in the Sodium-Channel Gene *SCN1A* Cause Severe Myoclonic Epilepsy of Infancy". *The American Journal of Human Genetics* 68.6 (2001), pp. 1327–1332.

[21] A. Escayg et al. "Mutations of *SCN1A*, Encoding a Neuronal Sodium Channel, in Two Families with GEFS+ 2". *Nature genetics* 24.4 (2000), pp. 343–345.

[22] F. H. Yu et al. "Reduced Sodium Current in GABAergic Interneurons in a Mouse Model of Severe Myoclonic Epilepsy in Infancy". *Nature Neuroscience* 9.9 (9 Sept. 2006), pp. 1142–1149.

[23] I. Ogiwara et al. "$Na_V1.1$ Localizes to Axons of Parvalbumin-Positive Inhibitory Interneurons: A Circuit Basis for Epileptic Seizures in Mice Carrying an *Scn1a* Gene Mutation". *Journal of Neuroscience* 27.22 (May 30, 2007), pp. 5903–5914.

[24] U. B. S. Hedrich et al. "Impaired Action Potential Initiation in GABAergic Interneurons Causes Hyperexcitable Networks in an Epileptic Mouse Model Carrying a Human $Na_V1.1$ Mutation". *Journal of Neuroscience* 34.45 (Nov. 5, 2014), pp. 14874–14889.

[25] O. Chever et al. "Initiation of Migraine-Related Cortical Spreading Depolarization by Hyperactivity of GABAergic Neurons and $Na_V1.1$ Channels". *The Journal of Clinical Investigation* (Sept. 7, 2021).

[26] L. Lemaire et al. "Modeling $Na_V1.1$/*SCN1A* Sodium Channel Mutations in a Microcircuit with Realistic Ion Concentration Dynamics Suggests Differential GABAergic Mechanisms Leading to Hyperexcitability in Epilepsy and Hemiplegic Migraine". *PLOS Computational Biology* 17.7 (July 27, 2021), e1009239.

[27] R. A. Ophoff et al. "Familial Hemiplegic Migraine and Episodic Ataxia Type-2 Are Caused by Mutations in the Ca2+ Channel Gene CACNL1A4". *Cell* 87.3 (Nov. 1, 1996), pp. 543–552.

[28] M. D. Fusco et al. "Haploinsufficiency of ATP1A2 Encoding the Na+/K+ Pump A2 Subunit Associated with Familial Hemiplegic Migraine Type 2". *Nature Genetics* 33.2 (2 Feb. 2003), pp. 192–196.

[29] "Defective Glutamate and K+ Clearance by Cortical Astrocytes in Familial Hemiplegic Migraine Type 2". *EMBO Molecular Medicine* 8.8 (Aug. 1, 2016), pp. 967–986.

[30] A. Tottene et al. "Enhanced Excitatory Transmission at Cortical Synapses as the Basis for Facilitated Spreading Depression in CaV2.1 Knockin Migraine Mice". *Neuron* 61.5 (Mar. 12, 2009), pp. 762–773.

[31] D. Vecchia et al. "Mechanism Underlying Unaltered Cortical Inhibitory Synaptic Transmission in Contrast with Enhanced Excitatory Transmission in CaV2.1 Knockin Migraine Mice". *Neurobiology of Disease* 69 (Sept. 1, 2014), pp. 225–234.

[32] S. Cestèle et al. "Divergent Effects of the T1174S *SCN1A* Mutation Associated with Seizures and Hemiplegic Migraine". *Epilepsia* 54.5 (2013), pp. 927–935.

[33] C. Fan et al. "Early-Onset Familial Hemiplegic Migraine Due to a Novel *SCN1A* Mutation". *Cephalalgia* 36.13 (Nov. 1, 2016), pp. 1238–1247.

[34] R. Barbieri et al. "Late Sodium Current Blocker GS967 Inhibits Persistent Currents Induced by Familial Hemiplegic Migraine Type 3 Mutations of the *SCN1A* Gene". *The Journal of Headache and Pain* 20.1 (Nov. 15, 2019), p. 107.

[35] M. Desroches et al. "Modeling Cortical Spreading Depression Induced by the Hyperactivity of Interneurons". *Journal of Computational Neuroscience* 47.2 (Dec. 1, 2019), pp. 125–140.

[36] J. Osteen et al. "Selective Spider Toxins Reveal a Role for the $Na_V1.1$ Channel in Mechanical Pain" (2016).

[37] S. Zerimech et al. "Cholinergic Modulation Inhibits Cortical Spreading Depression in Mouse Neocortex through Activation of Muscarinic Receptors and Decreased Excitatory/Inhibitory Drive". *Neuropharmacology* 166 (Apr. 1, 2020), p. 107951.

[38] H.-T. Chao et al. "Dysfunction in GABA Signalling Mediates Autism-like Stereotypies and Rett Syndrome Phenotypes". *Nature* 468.7321 (7321 Nov. 2010), pp. 263–269.

[39] E. Auffenberg et al. "Hyperexcitable Interneurons Trigger Cortical Spreading Depression in an *Scn1a* Migraine Model". *The Journal of Clinical Investigation* (Sept. 21, 2021).

[40] D. Golomb et al. "Mechanisms of Firing Patterns in Fast-Spiking Cortical Interneurons". *PLOS Computational Biology* 3.8 (Aug. 10, 2007), e156.

[41] M. Favero et al. "A Transient Developmental Window of Fast-Spiking Interneuron Dysfunction in a Mouse Model of Dravet Syndrome". *Journal of Neuroscience* 38.36 (Sept. 5, 2018), pp. 7912–7927.

[42] J.-L. Bény and O. Schaad. "An Evaluation of Potassium Ions as Endothelium-Derived Hyperpolarizing Factor in Porcine Coronary Arteries". *British Journal of Pharmacology* 131.5 (2000), pp. 965–973.

[43] G. Perea et al. "Activity-Dependent Switch of GABAergic Inhibition into Glutamatergic Excitation in Astrocyte-Neuron Networks". *eLife* 5 (Dec. 24, 2016). Ed. by M. Bartos, e20362.

[44] K. Kaila et al. "Cation-Chloride Cotransporters in Neuronal Development, Plasticity and Disease". *Nature Reviews Neuroscience* 15.10 (10 Oct. 2014), pp. 637–654.

[45] Z. Shiri et al. "Activation of Specific Neuronal Networks Leads to Different Seizure Onset Types". *Annals of Neurology* 79.3 (2016), pp. 354–365.

[46] K. Kaila et al. "Long-Lasting GABA-Mediated Depolarization Evoked by High-Frequency Stimulation in Pyramidal Neurons of Rat Hippocampal Slice Is Attributable to a Network-Driven, Bicarbonate-Dependent K+ Transient". *Journal of Neuroscience* 17.20 (Oct. 15, 1997), pp. 7662–7672.

[47] K. L. Richards et al. "Selective $Na_V1.1$ Activation Rescues Dravet Syndrome Mice from Seizures and Premature Death". *Proceedings of the National Academy of Sciences* 115.34 (Aug. 21, 2018), E8077–E8085.

[48] A. Maslarova et al. "Chronically Epileptic Human and Rat Neocortex Display a Similar Resistance Against Spreading Depolarization In Vitro". *Stroke* 42.10 (Oct. 1, 2011), pp. 2917–2922.

[49] V. I. Koroleva, L. V. Vinogradova, and J. Bures. "Reduced Incidence of Cortical Spreading Depression in the Course of Pentylenetetrazol Kindling in Rats". *Brain Research* 608.1 (Apr. 9, 1993), pp. 107–114.

[50] R. C. A. Guedes and E. A. Cavalheiro. "Blockade of Spreading Depression in Chronic Epileptic Rats: Reversion by Diazepam". *Epilepsy Research* 27.1 (Apr. 1, 1997), pp. 33–40.

[51] D. R. Kramer et al. "Interplay between Cortical Spreading Depolarization and Seizures". *Stereotactic and Functional Neurosurgery* 95.1 (2017), pp. 1–5.

[52] I. Aiba and J. L. Noebels. "Spreading Depolarization in the Brainstem Mediates Sudden Cardiorespiratory Arrest in Mouse SUDEP Models". *Science Translational Medicine* 7.282 (Apr. 8, 2015), 282ra46–282ra46.

[53] D. Y. Chung et al. "Determinants of Optogenetic Cortical Spreading Depolarizations". *Cerebral Cortex* 29.3 (Mar. 1, 2019), pp. 1150–1161.

[54] D. Vecchia and D. Pietrobon. "Migraine: A Disorder of Brain Excitatory–Inhibitory Balance?" *Trends in Neurosciences* 35.8 (Aug. 1, 2012), pp. 507–520.

[55] A. V. Delgado-Escueta. *Myoclonic Epilepsies*. Lippincott Williams & Wilkins, 2005. 368 pp.

[56] S. M. Zuberi et al. "Genotype–Phenotype Associations in *SCN1A*-Related Epilepsies". *Neurology* 76.7 (Feb. 15, 2011), pp. 594–600.

[57] Y.-H. Zhang et al. "Genetic Epilepsy with Febrile Seizures plus: Refining the Spectrum". *Neurology* 89.12 (Sept. 19, 2017), pp. 1210–1219.

[58] L. Yekhlef et al. "Selective Activation of Parvalbumin- or Somatostatin-Expressing Interneurons Triggers Epileptic Seizurelike Activity in Mouse Medial Entorhinal Cortex". *Journal of Neurophysiology* 113.5 (Mar. 1, 2015), pp. 1616–1630.

[59] M. Ledri et al. "Global Optogenetic Activation of Inhibitory Interneurons during Epileptiform Activity". *Journal of Neuroscience* 34.9 (Feb. 26, 2014), pp. 3364–3377.

[60] L. J. Ptáček. "Episodic Disorders: Channelopathies and Beyond". *Annual Review of Physiology* 77.1 (2015), pp. 475–479.

[61] W. Truccolo et al. "Single-Neuron Dynamics in Human Focal Epilepsy". *Nature Neuroscience* 14.5 (5 May 2011), pp. 635–641.

[62] N. Tamamaki et al. "Green Fluorescent Protein Expression and Colocalization with Calretinin, Parvalbumin, and Somatostatin in the GAD67-GFP Knock-in Mouse". *Journal of Comparative Neurology* 467.1 (2003), pp. 60–79.

[63] L. Madisen et al. "A Toolbox of Cre-Dependent Optogenetic Transgenic Mice for Light-Induced Activation and Silencing". *Nature Neuroscience* 15.5 (5 May 2012), pp. 793–802.

[64] K. Baalman et al. "Axon Initial Segment–Associated Microglia". *Journal of Neuroscience* 35.5 (Feb. 4, 2015), pp. 2283–2292.

[65] Y. Li et al. "Serotonin Neurons in the Dorsal Raphe Nucleus Encode Reward Signals". *Nature Communications* 7.1 (1 Jan. 28, 2016), p. 10503.

[66] J. L. Wagnon et al. "Etiology of a Genetically Complex Seizure Disorder in Celf4 Mutant Mice". *Genes, Brain and Behavior* 10.7 (2011), pp. 765–777.

[67] B. Wang et al. "The Amyloid Precursor Protein Controls Adult Hippocampal Neurogenesis through GABAergic Interneurons". *Journal of Neuroscience* 34.40 (Oct. 1, 2014), pp. 13314–13325.

[68] C. Liautard et al. "Hippocampal Hyperexcitability and Specific Epileptiform Activity in a Mouse Model of Dravet Syndrome". *Epilepsia* 54.7 (2013), pp. 1251–1261.

[69] O. Chever et al. "Implication of Kir4.1 Channel in Excess Potassium Clearance: An In Vivo Study on Anesthetized Glial-Conditional Kir4.1 Knock-Out Mice". *Journal of Neuroscience* 30.47 (Nov. 24, 2010), pp. 15769–15777.

[70] G. Bechi et al. "Pure Haploinsufficiency for Dravet Syndrome $Na_V1.1$ (*SCN1A*) Sodium Channel Truncating Mutations". *Epilepsia* 53.1 (2012), pp. 87–100.

[71] B. Ermentrout. *Simulating, Analyzing, and Animating Dynamical Systems: A Guide to XPPAUT for Researchers and Students*. Vol. 14. Siam, 2002.

[72] R. A. McDougal et al. "Twenty Years of ModelDB and beyond: Building Essential Modeling Tools for the Future of Neuroscience". *Journal of computational neuroscience* 42.1 (2017), pp. 1–10.

[73] G. Florence et al. "The Role of Extracellular Potassium Dynamics in the Different Stages of Ictal Bursting and Spreading Depression: A Computational Study". *Journal of theoretical biology* 258.2 (2009), pp. 219–228.

[74] Y. Wei, G. Ullah, and S. J. Schiff. "Unification of Neuronal Spikes, Seizures, and Spreading Depression". *Journal of Neuroscience* 34.35 (2014), pp. 11733–11743.

[75] G. Huguet et al. "Neuroprotective Role of Gap Junctions in a Neuron Astrocyte Network Model". *Biophysical journal* 111.2 (2016), pp. 452–462.

[76] Y. Bouret, M. Argentina, and L. Counillon. "Capturing Intracellular pH Dynamics by Coupling Its Molecular Mechanisms within a Fully Tractable Mathematical Model". *PloS one* 9.1 (2014), e85449.

[77] M. Rudolph et al. "Characterization of Synaptic Conductances and Integrative Properties during Electrically Induced EEG-Activated States in Neocortical Neurons in Vivo". *Journal of neurophysiology* 94.4 (2005), pp. 2805–2821.

[78] A. Destexhe, Z. F. Mainen, and T. J. Sejnowski. "An Efficient Method for Computing Synaptic Conductances Based on a Kinetic Model of Receptor Binding". *Neural computation* 6.1 (1994), pp. 14–18.

[79] C. Börgers, S. Epstein, and N. J. Kopell. "Background Gamma Rhythmicity and Attention in Cortical Local Circuits: A Computational Study". *Proceedings of the National Academy of Sciences* 102.19 (2005), pp. 7002–7007.

[80] H. Y. Jeong and B. Gutkin. "Synchrony of Neuronal Oscillations Controlled by GABAergic Reversal Potentials". *Neural Computation* 19.3 (2007), pp. 706–729.

[81] X.-J. Wang. "Calcium Coding and Adaptive Temporal Computation in Cortical Pyramidal Neurons". *Journal of Neurophysiology* 79.3 (1998), pp. 1549–1566.

[82] X.-J. Wang and G. Buzsáki. "Gamma Oscillation by Synaptic Inhibition in a Hippocampal Interneuronal Network Model". *Journal of Neuroscience* 16.20 (1996), pp. 6402–6413.

[83] H. Kager, W. J. Wadman, and G. G. Somjen. "Simulated Seizures and Spreading Depression in a Neuron Model Incorporating Interstitial Space and Ion Concentrations". *Journal of neurophysiology* 84.1 (2000), pp. 495–512.

[84] E. Syková and C. Nicholson. "Diffusion in Brain Extracellular Space". *Physiological reviews* 88.4 (2008), pp. 1277–1340.

[85] P. Läuger. *Electrogenic Ion Pumps*. 576.314 LAU. 1991.

[86] R. D. Traub et al. "A Model of a CA3 Hippocampal Pyramidal Neuron Incorporating Voltage-Clamp Data on Intrinsic Conductances". *Journal of Neurophysiology* 66.2 (1991), pp. 635–650.

[87] B. P. Bean. "The Action Potential in Mammalian Central Neurons". *Nature Reviews Neuroscience* 8.6 (2007), pp. 451–465.

[88] J. Magistretti and A. Alonso. "Biophysical Properties and Slow Voltage-Dependent Inactivation of a Sustained Sodium Current in Entorhinal Cortex Layer-II Principal Neurons: A Whole-Cell and Single-Channel Study". *The Journal of general physiology* 114.4 (1999), pp. 491–509.

[89] E. M. Izhikevich. *Dynamical Systems in Neuroscience*. MIT press, 2007.

[90] E. Benoît. *Dynamic Bifurcations: Proceedings of a Conference Held in Luminy, France, March 5-10, 1990*. Vol. 1493. Lecture Notes in Mathematics. Springer, 1991.

[91] J. Rinzel. "A Formal Classification of Bursting Mechanisms in Excitable Systems". *Mathematical Topics in Population Biology, Morphogenesis and Neurosciences: Proceedings of an International Symposium Held in Kyoto, November 10–15, 1985*. Ed. by E. Teramoto and M. Yumaguti. Lecture Notes in Biomathematics. Berlin, Heidelberg: Springer, 1987, pp. 267–281.

[92] R. E. Carter et al. "Intracellular Zn2+ Accumulation Enhances Suppression of Synaptic Activity Following Spreading Depolarization". *Journal of neurochemistry* 125.5 (2013), pp. 673–684.

[93] B. E. Lindquist and C. W. Shuttleworth. "Adenosine Receptor Activation Is Responsible for Prolonged Depression of Synaptic Transmission after Spreading Depolarization in Brain Slices". *Neuroscience* 223 (2012), pp. 365–376.

[94] M. A. Dahlem, J. Schumacher, and N. Hübel. "Linking a Genetic Defect in Migraine to Spreading Depression in a Computational Model". *PeerJ* 2 (2014), e379.

[95] Z. J. Huang and A. Paul. "The Diversity of GABAergic Neurons and Neural Communication Elements". *Nature Reviews Neuroscience* 20.9 (2019), pp. 563–572.

[96] R. Tremblay, S. Lee, and B. Rudy. "GABAergic Interneurons in the Neocortex: From Cellular Properties to Circuits". *Neuron* 91.2 (2016), pp. 260–292.

[97] J. C. Oakley et al. "Temperature-and Age-Dependent Seizures in a Mouse Model of Severe Myoclonic Epilepsy in Infancy". *Proceedings of the National Academy of Sciences* 106.10 (2009), pp. 3994–3999.

[98] J. Ziburkus et al. "Interneuron and Pyramidal Cell Interplay during in Vitro Seizure-like Events". *Journal of neurophysiology* 95.6 (2006), pp. 3948–3954.

[99] M. Cammarota et al. "Fast Spiking Interneuron Control of Seizure Propagation in a Cortical Slice Model of Focal Epilepsy". *The Journal of Physiology* 591.4 (2013), pp. 807–822.

[100] C. M. Kim and D. Q. Nykamp. "The Influence of Depolarization Block on Seizure-like Activity in Networks of Excitatory and Inhibitory Neurons". *Journal of computational neuroscience* 43.1 (2017), pp. 65–79.

[101] P. Kurbatova et al. "Dynamic Changes of Depolarizing GABA in a Computational Model of Epileptogenic Brain: Insight for Dravet Syndrome". *Experimental neurology* 283 (2016), pp. 57–72.

[102] Y. Yuan et al. "Delayed Maturation of GABAergic Signaling in the *Scn1a* and *Scn1b* Mouse Models of Dravet Syndrome". *Scientific reports* 9.1 (2019), pp. 1–16.

[103] O. Tomkins et al. "Blood–Brain Barrier Disruption Results in Delayed Functional and Structural Alterations in the Rat Neocortex". *Neurobiology of disease* 25.2 (2007), pp. 367–377.

[104] J. Rinzel. "Bursting Oscillations in an Excitable Membrane Model". *Ordinary and Partial Differential Equations*. Ed. by B. D. Sleeman and R. J. Jarvis. Lecture Notes in Mathematics. Berlin, Heidelberg: Springer, 1985, pp. 304–316.

[105] N. Hübel and M. A. Dahlem. "Dynamics from Seconds to Hours in Hodgkin-Huxley Model with Time-Dependent Ion Concentrations and Buffer Reservoirs". *PLoS Computational Biology* 10.12 (Dec. 4, 2014). Ed. by B. Ermentrout, e1003941.

[106] G. Ullah et al. "The Role of Cell Volume in the Dynamics of Seizure, Spreading Depression, and Anoxic Depolarization". *PLOS Computational Biology* 11.8 (Aug. 14, 2015), e1004414.

[107] K. Ma, H. Gu, and Z. Zhao. "Fast–Slow Variable Dissection with Two Slow Variables: A Case Study on Bifurcations Underlying Bursting for Seizure and Spreading Depression". *International Journal of Bifurcation and Chaos* (May 26, 2021).

[108] E. Doedel et al. *AUTO-07P: Continuation and Bifurcation Software for Ordinary Differential Equations*. Version 0.8. 2007.

[109] M. Desroches, M. Krupa, and S. Rodrigues. "Spike-Adding in Parabolic Bursters: The Role of Folded-Saddle Canards". *Physica D: Nonlinear Phenomena* 331 (Sept. 2016), pp. 58–70.

[110] M. Desroches and V. Kirk. "Spike-Adding in a Canonical Three-Time-Scale Model: Superslow Explosion and Folded-Saddle Canards". *SIAM Journal on Applied Dynamical Systems* 17.3 (Jan. 1, 2018), pp. 1989–2017.

[111] J. L. Hindmarsh and R. M. Rose. "A Model of the Nerve Impulse Using Two First-Order Differential Equations". *Nature* 296.5853 (5853 Mar. 1982), pp. 162–164.

[112] S. Tsuji et al. "Bifurcations in Two-Dimensional Hindmarsh–Rose Type Model". *International Journal of Bifurcation and Chaos* 17.03 (Mar. 1, 2007), pp. 985–998.

[113] Y. Che et al. "Synchronization of Inhibitory Coupled Hindmarsh-Rose Neurons via Adaptive Sliding Mode Control". *2011 2nd International Conference on Intelligent Control and Information Processing*. Vol. 2. July 2011, pp. 1134–1139.

[114] J. Nagumo, S. Arimoto, and S. Yoshizawa. "An Active Pulse Transmission Line Simulating Nerve Axon". *Proceedings of the IRE* 50.10 (Oct. 1962), pp. 2061–2070.

[115] R. FitzHugh. "Impulses and Physiological States in Theoretical Models of Nerve Membrane". *Biophysical Journal* 1.6 (July 1, 1961), pp. 445–466.

[116] M. Desroches et al. "Mixed-Mode Oscillations with Multiple Time Scales". *SIAM Review* 54.2 (Jan. 1, 2012), pp. 211–288.

[117] K. Tsaneva-Atanasova et al. "Full System Bifurcation Analysis of Endocrine Bursting Models". *Journal of Theoretical Biology* 264.4 (June 21, 2010), pp. 1133–1146.

[118] M. T. M. Koper. "Bifurcations of Mixed-Mode Oscillations in a Three-Variable Autonomous Van Der Pol-Duffing Model with a Cross-Shaped Phase Diagram". *Physica D: Nonlinear Phenomena* 80.1 (Jan. 1, 1995), pp. 72–94.

[119] J. Guckenheimer and Y. A. Kuznetsov. "Hopf-Hopf Bifurcation". *Scholarpedia* 3.8 (Aug. 21, 2008), p. 1856.

[120] R. E. Westenbroek, D. K. Merrick, and W. A. Catterall. "Differential Subcellular Localization of the RI and RII Na+ Channel Subtypes in Central Neurons". *Neuron* 3.6 (Dec. 1, 1989), pp. 695–704.

[121] B. Gong et al. "Type I and Type II Na+ Channel α-Subunit Polypeptides Exhibit Distinct Spatial and Temporal Patterning, and Association with Auxiliary Subunits in Rat Brain". *Journal of Comparative Neurology* 412.2 (1999), pp. 342–352.

[122] W. R. J. Whitaker et al. "Comparative Distribution of Voltage-Gated Sodium Channel Proteins in Human Brain". *Molecular Brain Research* 88.1 (Mar. 31, 2001), pp. 37–53.

[123] A. Duflocq et al. "$Na_V1.1$ Is Predominantly Expressed in Nodes of Ranvier and Axon Initial Segments". *Molecular and Cellular Neuroscience* 39.2 (Oct. 1, 2008), pp. 180–192.

[124] S. Ovsepian. *Are Synaptic Vesicles Released during Depolarization Block?* ResearchGate. URL: `https://www.researchgate.net/post/Are-synaptic-vesicles-released-during-depolarization-block` (visited on 10/22/2021).

[125] A. Călin, A. S. Ilie, and C. J. Akerman. "Disrupting Epileptiform Activity by Preventing Parvalbumin Interneuron Depolarization Block". *Journal of Neuroscience* (Oct. 5, 2021).

[126] M. Bélanger and P. J. Magistretti. "The Role of Astroglia in Neuroprotection". *Dialogues in Clinical Neuroscience* 11.3 (Sept. 2009), pp. 281–295.

[127] C. Ayata and M. Lauritzen. "Spreading Depression, Spreading Depolarizations, and the Cerebral Vasculature". *Physiological Reviews* 95.3 (July 1, 2015), pp. 953–993.

[128] H. Kager, W. J. Wadman, and G. G. Somjen. "Seizure-like Afterdischarges Simulated in a Model Neuron". *Journal of Computational Neuroscience* 22.2 (Apr. 1, 2007), pp. 105–128.

[129] A. V. Chizhov et al. "A Simple Markov Model of Sodium Channels with a Dynamic Threshold". *Journal of Computational Neuroscience* 37.1 (Aug. 1, 2014), pp. 181–191.

[130] G. B. Ermentrout and N. Kopell. "Parabolic Bursting in an Excitable System Coupled with a Slow Oscillation". *SIAM Journal on Applied Mathematics* 46.2 (Apr. 1, 1986), pp. 233–253.